CONTRACTOR REPORT

Development of a Circulating Zinc-Bromine Battery Phase I – Final Report

R. Bellows, H. Einstein, P. Grimes,
E. Kantner, P. Malachesky, K. Newby, H. Tsien
Exxon Research and Engineering Company
Advanced Energy Systems Laboratory
Linden, NJ 07036

Prepared by Sandia National Laboratories Albuquerque, New Mexico 87185
and Livermore, California 94550 for the United States Department of Energy
under Contract DE-AC04-76DP00789

Printed January 1983

Issued by Sandia National Laboratories, operated for the United States Department of Energy by Sandia Corporation.

Printed in the United States of America
Available from
National Technical Information Service
U.S. Department of Commerce
5285 Port Royal Road
Springfield, VA 22161

NTIS price codes
Printed copy: A09
Microfiche copy: A01

GENERAL DISCLAIMER

This document may be affected by one or more of the following statements

- **This document has been reproduced from the best copy furnished by the sponsoring agency. It is being released in the interest of making available as much information as possible.**
- **This document may contain data which exceeds the sheet parameters. It was furnished in this condition by the sponsoring agency and is the best copy available.**
- **This document may contain tone-on-tone or color graphs, charts and/or pictures which have been reproduced in black and white.**
- **This document is paginated as submitted by the original source.**
- **Portions of this document are not fully legible due to the historical nature of some of the material. However, it is the best reproduction available from the original submission.**

EXXON RESEARCH AND ENGINEERING COMPANY

CORPORATE RESEARCH LABORATORIES

DEVELOPMENT OF A CIRCULATING ZINC-BROMINE BATTERY

PHASE I - FINAL REPORT

Exxon Research and Engineering Company

R. Bellows - Project Head
H. Einstein
P. Grimes
E. Kantner
P. Malachesky
K. Newby
H. Tsien

January 1982

Advanced Energy Systems Laboratory

P. O. BOX 45 ■ LINDEN, NEW JERSEY 07036

TABLE OF CONTENTS

LIST OF FIGURES

LIST OF TABLES

000. Abstract

This report summarizes Phase I of a three phase program aimed at developing Exxon's circulating zinc-bromine battery for photovoltaic energy storage. This effort was cost shared by Exxon and DOE/Sandia. Previous work at Exxon had developed a basic zinc-bromine system approach. This approach incorporates carbon plastic electrodes in a bipolar stack design, a circulating electrolyte with separable bromine complexes, and shunt current protection.

Phase I was highlighted by the successful scale-up and demonstration of 3 and 10 kWh submodules. Two smaller demonstration batteries were delivered to Sandia for testing. Important technology improvements were demonstrated concerning shunt current protection, improved performance of low cost microporous separators, and insert injection molding of electrodes and separators. Base technology was expanded via an increased parametric testing program, materials testing and electrolyte studies.

Production cost estimates were revised based on improved design concepts to project direct factory costs of $28/kWh (1980$) for large scale production of 20 kWh modules. A potential developmental plan was drafted, delineating critical development milestones. The project effort is continuing to show steady progress toward developing a deliverable 20 kWh photovoltaic battery for the completion of Phase III in 1983.

00. Summary

Exxon Research and Engineering has been developing an advanced battery system based on zinc and bromine. Projected performance for the system makes it suitable for various applications such as photovoltaic and bulk energy storage, and vehicle traction. This report summarizes Phase I of a three phase effort to develop Exxon's circulating zinc-bromine battery for photovoltaic energy storage. The effort was cost shared by Exxon and DOE/Sandia on contract 49-2862. This report covers development work between April 1, 1980 and April 29, 1981, as well as previously developed background material.

The goals of Phase I were to scale the system into multi-kilowatt hour, multi-stack demonstrations as well as to broaden the base technology. Phase II will continue development of the base technology, and will be highlighted by the cycling of a 20 kWh module. This represents a suitable scale for residential photovoltaic storage. Finally, the goal of Phase III will be to deliver a self-contained optimized 20 kWh system to Sandia National Laboratories for testing and evaluation.

The structure of the report roughly corresponds section-by-section to the structure of major tasks outlined in the Phase I program proposal. This should aid reviewers familiar with the original program proposal.

Phase I was marked by steady progress in all program areas. System scale-ups to 3 and 10 kWh submodules remained close to schedule with system demonstration of 100 plus and 50 plus cycles, respectively. These submodules were based on 80 V stacks comprised of 52 bipolar electrodes. The stacks have provided the most rigorous testing of our new concepts for shunt current protection. These concepts allow the use of carbon plastic bipolar electrodes, a cornerstone of our low cost approach. Furthermore, all key technical elements, the bipolar carbon plastic electrodes, the separable bromine complexers, circulating electrolytes, microporous separators, shunt current protection and multi-stack parallel operations, have now been combined and show stable operation in significantly large scale demonstrations.

Two smaller batteries, a 500 Wh without shunt current protection and a 1.3 kWh with protection, have been delivered to contract monitors at Sandia National Laboratories for in-house testing, evaluation and familiarization. The initial battery, delivered in October, has been cycled over 100 times, showing performances equal to those achieved in Exxon laboratories. In spite of minor damage incurred during shipping, operation of the 500 Wh unit has been trouble-free. The second battery has been delivered and is now undergoing testing.

Several specific technology improvements were further demonstrated during Phase I. The continued development of an electrolyte additive treatment to impart selectivity to the microporous separators resulted in the achievement of stable coulombic efficiency for 150 plus cycles. An improved concept of shunt current protection, called "Tunnel Protection", based on electrolyte interconnects between branched channels has undergone further development and testing. This decouples hydraulics and shunt currents and reduces the system's auxiliary power consumption. Demonstration of injection molding of 6 dm^2 inserts (i.e., active area equal 600 cm^2), using either electrodes or separators, greatly increased the availablity of system components. This also increases the potential for mass producing batteries. The parametric testing program has continued to expand the system data base in terms of duty cycles, system variations, component life and system reliability.

Manufacturing cost projections were updated, including recent injection rates, new electrode extrusion concepts and cost reductions on the electrolyte. Direct factory production costs for 20 kWh units in large scale production (100,000 batteries per year) are projected at $28/kWh (1980$). This estimate includes most direct costs, but excludes most indirect costs. This cost estimate also incorporates recent design improvements as well as increased experience in plastic fabrication and assembly. A projected commercialization schedule, aimed at marketing 20 kWh units for photovoltaic storage, bulk energy storage and traction vehicles, was prepared. This schedule delineates major technical milestones as well as pilot plant production targets. The program could reasonably be producing 25,000-100,000 units/year by the early 1990's.

Future project efforts are turning to the Phase II program. Emphasis will be on demonstrating a 20 kWh battery, continuing development of production techniques, and extending cycle life data. An automatic life cycle station with a microprocessor based battery controller will be constructed to obtain extended cycle life data.

0. Introduction

The structure of this final report follows the general outline of major tasks that were delineated in the original Phase I program Work Statement. The report includes overall Phase I progress and concludes at the end of Phase I activities. Some previously unpublished background work, concluded prior to the start of Phase I, has also been included. This section (Introduction) has been added to furnish general information on the Phase I program and on the operation of Exxon's circulating zinc bromine battery to readers unfamiliar with our recent progress.

0.1 Highlights of Phase I

This work represents the first phase of a three phase program whose goal is the development of Exxon's circulating zinc-bromine battery for photovoltaic and bulk energy storage applications. Phase I built on a foundation of technology that had previously been developed by Exxon Research and Engineering Company. The present effort is cost shared by Exxon and DOE/Sandia (Contract 49-2862). Phase I had several goals among which are:

Continued development of the base zinc-bromine technology, development of a design for a 20 kWh photovoltaic battery, demonstrations of intermediate scale-ups on the path to a 20 kWh design and delivery of two small demonstration batteries to contract monitors at Sandia.

Steady and timely progress was made toward those goals so that at the conclusion of Phase I, a number of individual accomplishments deserved mention, namely:

- Successful cycling of 3 kWh (X-3) sub-module for 100+ cycles
- Successful cycling of 10 kWh (X-10) sub-module for 50+ cycles
- 500 Wh battery and 1.3 kWh battery with shunt current protection delivered to Sandia
- Shunt current protection demonstrated for 100+ cycles
- Mass manufacturing techniques, injection molded electrodes, demonstrated
- Cost estimates refined for advanced 20 kWh design
- Developemental plan produced

These major accomplishments as well as a general broadening of system knowledge are discussed below in detail.

Projected system performance is shown in Table 0-1. These performance estimates are based on the performance of present electrodes and electrolytes, in either the 3 kWh or smaller 500 Wh batteries projected into the advanced 20 kWh design (Section I.1). Therefore, the only assumptions are: there will be no loss of performance during the scale-up to larger electrodes, there will be a 10% power requirement for auxiliaries, and the weight and volume reductions associated with reservoir and electrode support structures will be achieved. If these are valid

TABLE 0-1

EXXON'S ZINC-BROMINE BATTERY PERFORMANCE

		PRESENT*	PROJECTED+
Electrochemical Efficiency	(%)	68-73	72-78
Voltaic Efficiency	(%)	85	85-90
Coulombic Efficiency	(%)	80-85	85-90
Energy Efficiency	(%)	65-70	70-75
Specific Energy	(Wh/kg)	55	65-70
Energy Density	(Wh/l)	70	80-85
Specific Power	(W/kg)	80	90-100
Power Density (20-Sec.)	(W/l)	90	105-110
Discharge Voltage	(V)	80	120
Factory Cost- 100,000 Units/Yr	(1980 $)	-	$28.05

* Present Electrode Performance of X-3 Modules in 20 kWh Design

+ Present Electrode Performance of 500-Wh Systems in Advanced 20 kWh Design

assumptions, then our successful demonstrations of 3 and 10 kWh sub-modules and recent production cost estimates, make Exxon's circulating zinc-bromine battery a leading advanced battery candidate for photovoltaic and bulk energy storage as well as for vehicle traction.

0.2 General Circulating Zinc Bromine Battery Background

This section briefly discusses the principles of system operation and describes major components.

0.2.1 Introduction and System Description

The Exxon zinc-bromine battery is based on a battery module with a flowing electrolyte and utilizes two recent developments: a reversible liquid bromine complexing agent and conductive carbon-plastic technology. Previous attempts to develop the zinc-bromine battery have failed because of problems with self-discharge due to bromine diffusion between electrodes, irregular and dendritic zinc growth, and corrosion problems due to the high reactivity of bromine. In the present approach, self-discharge is controlled by use of a bromine complexing agent to store bromine outside of the cell. Electrolyte circulation gives uniform zinc deposition, and corrosion is avoided by the use of the conductive carbon-plastic and other plastic components which are bromine-resistant. In addition, carbon-plastic components provide a low cost, easily mass-produced battery module.

The basic understanding of bromine complexation chemistry was acquired in an extensive synthesis and screening effort over a two-year period. Hundreds of compounds representing six major classes of complexing agents were tested. Eventually, preferred complexing agents were chosen, based on rapid reversibility, bromine resistance, and general compatibility with the flowing zinc bromine system (1).

In developing this technology, Exxon views the zinc-bromine (Zn/Br_2) battery as an advanced candidate for various energy storage and motive power applications. System components are basically in-hand, and system development does not depend on inventing some as-yet-to-be-developed component. Rather, the progress from this point must be measured in terms of continued performance improvement (duty cycles, life, and cost consideration) and adaptability to specific applications.

Operation of the Circulating Zinc-Bromine Battery

Advanced battery designs, based on the circulating electrolyte concept, have been proposed for various couples, such as lead acid, zinc-nickel, iron-nickel, zinc-chlorine and zinc-bromine. Electrolyte circulation is generally useful for feeding reactants, removing products, assisting thermal management, and homogenizing the electrolyte. Although electrolyte circulation increases design complexity, it frequently allows better performance and higher specific energies. A particular advantage in the Zn/Br_2 battery is improved uniformity of the Zn plating during charging.

A schematic of a circulating Zn/Br_2 battery is shown in Figure 0-1. The system has three main components. The principal component is the electrochemical module, where the actual electrochemistry takes place. The second component is the circulating electrolyte, an aqueous solution of zinc bromide and bromine complexing agent, which is circulated in two streams through the electrochemical module. The third component is the system of pumps and reservoirs which store and circulate the electrolyte. The operation of the Zn/Br_2 battery is easily understood by following a typical charge/discharge cycle. During charge, zinc is plated at the negative electrode and bromine is evolved at the positive electrode. Bromine reacts with the complexing agent to form a second phase, indicated by dots in Figure 0-1. This bromine-rich phase is circulated out of the electrochemical module and is separated by gravity in the catholyte reservoir. Long-term charge retention is excellent because the Br_2 is stored remotely from the zinc. During discharge, the catholyte valve is opened and the Br_2 complex is fed back to the module. Now, Zn and Br_2 electrochemically react to form the original zinc bromide solution, liberating the energy absorbed during charging. The separator prevents direct mixing of the anode and cathode loops, thereby reducing self-discharge during cycling.

Component Descriptions

Battery Module - The battery module is nearly all plastic construction, so that the final product can be easily and economically mass-produced. Figure 0-2 shows an expanded view of the battery components, an alternating series of electrodes, plastic screens and separators.

a.) Electrodes - Previous zinc-bromine batteries have been plagued by bromine corrosion of metallic electrodes. Even titanium-based electrodes show corrosion pitting, resulting from bipolar shunt currents and/or from cell reversal. The Exxon Zn/Br_2 battery has avoided this problem by the use of a conductive carbon plastic composite. The carbon plastic is used for both the zinc and bromine electrodes. An extra layer of porous carbon is added at the Br_2 electrode to increase the reactive surface area. The conductive carbon plastic is framed with a filled, non-conductive plastic which matches the thermal properties of the carbon plastic. Flow channels, molded into the non-conductive plastic, uniformly distribute the two flowing electrolytes to each cell. The conductivity of the carbon plastic (about 1 $(ohm \cdot cm)^{-1}$) is sufficiently high that there is virtually no ohmic loss in the case of bipolar electrodes. The carbon plastic conductivity is not sufficiently high, however, for efficient monopolar electrodes, but metallic current collectors can be molded into the carbon plastic to increase lateral conductivity. There is no observable contact resistance between the metal screens and carbon plastic because of the high contact area and high compressive stresses generated during molding operations. Such composite electrodes have been used in monopolar configurations, and are presently used as endplates on bipolar stacks. The area of the present electrodes is 600 cm^2 but the materials and techniques can be easily scaled to larger dimensions.

ZINC-BROMINE CIRCULATING BATTERY

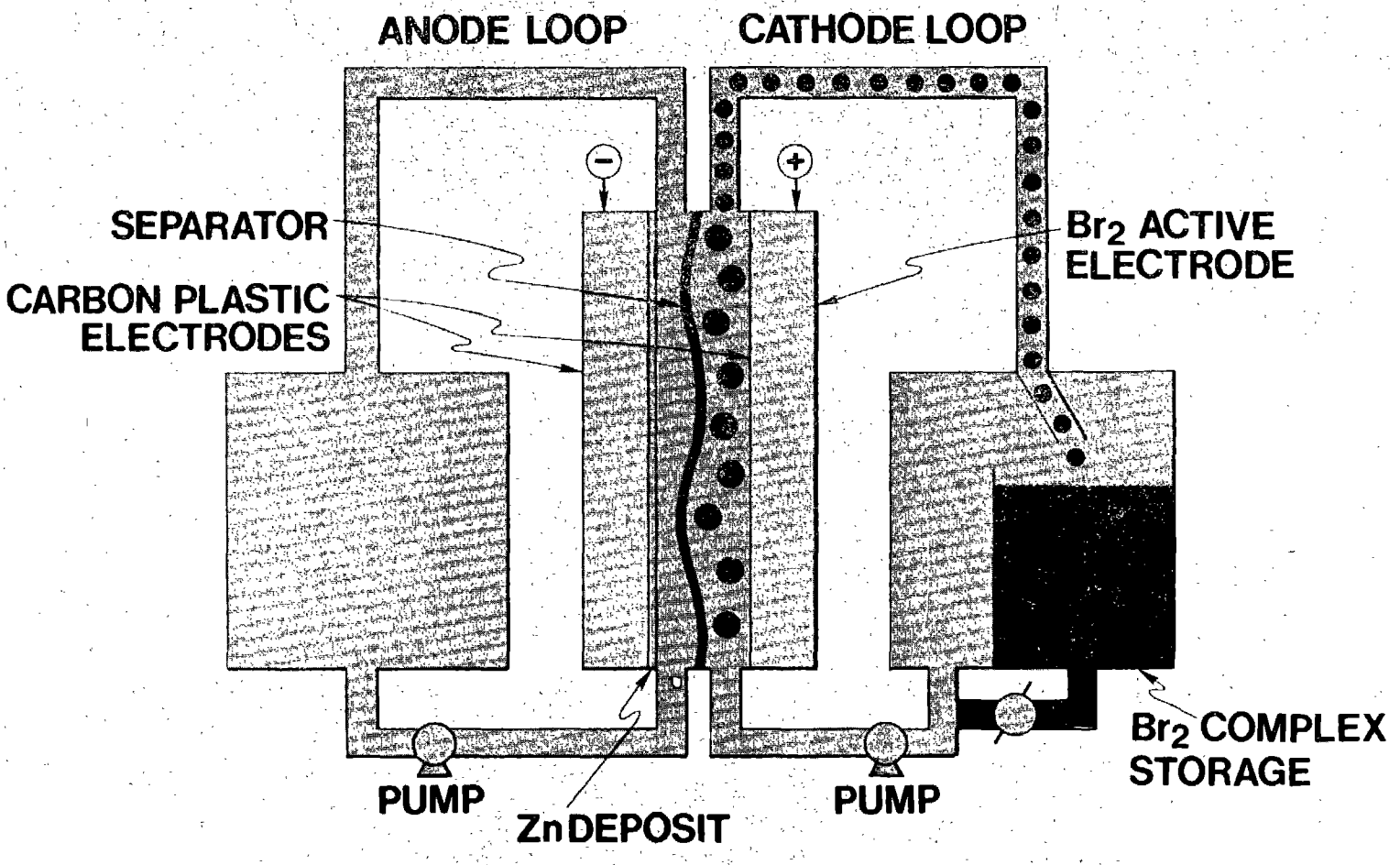

Electrochemical Reactions:

$$Zn^{\circ} \rightleftharpoons Zn^{++} + 2e^{-}$$

$$Br_2 + 2e^{-} \rightleftharpoons 2Br^{-}$$

Self discharge:

$$Zn^{\circ} + Br_2 \rightarrow ZnBr_2$$

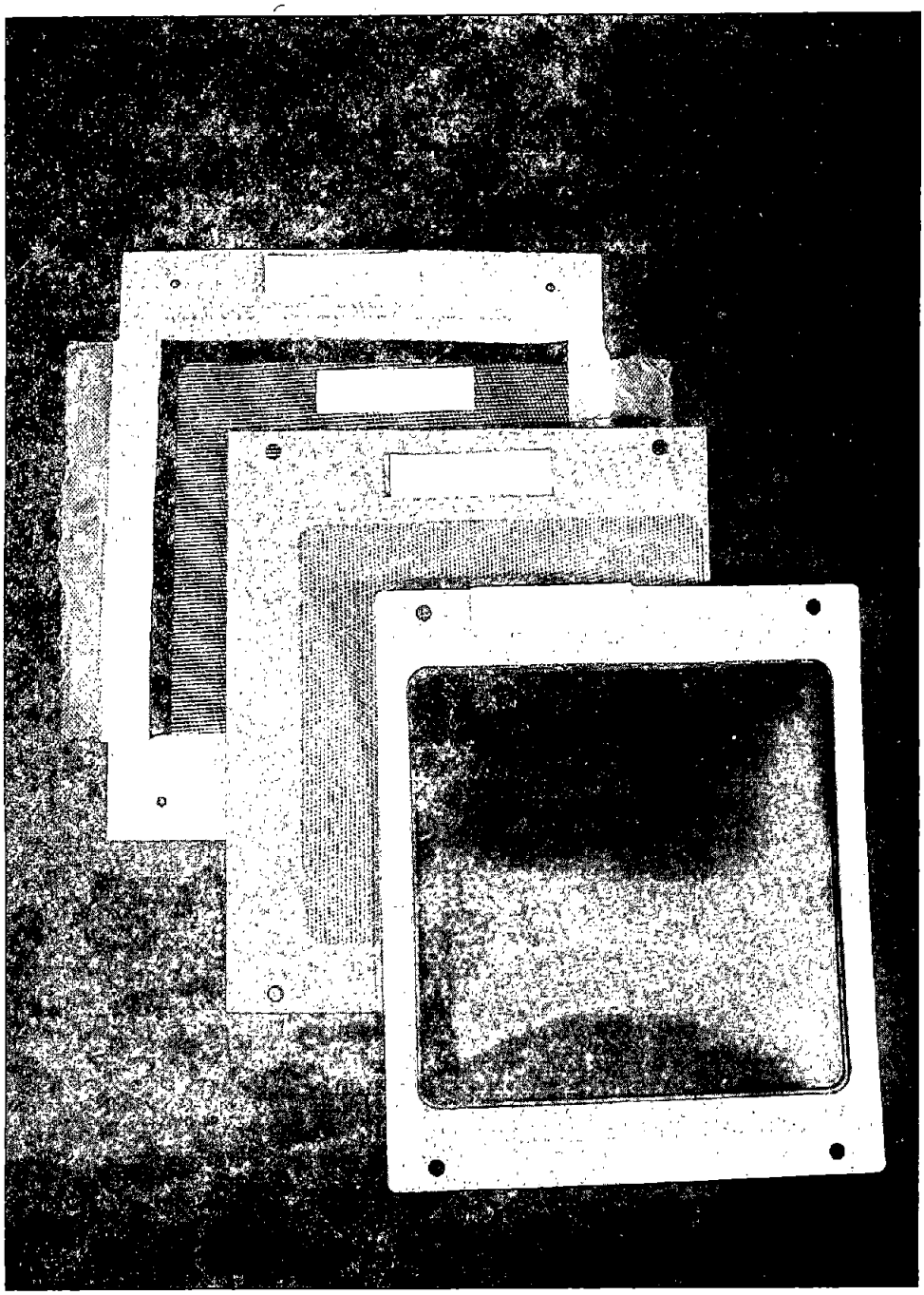

Figure 0-2 Battery Stack Components

b.) Screens - Screens of polypropylene or polyethylene separate the electrodes from the membrane. Vexar screens, made by DuPont, are being used presently. The screens keep the electrodes uniformly spaced and provide extra volume for zinc deposition. They promote uniform flow distribution over the electrode face.

c.) Separator - Previous work emphasized ion-selective membranes. These separators were made of a Teflon film which had been grafted with sulfonated styrene to induce ion selectivity. This membrane passes zinc ions and limits the migration of Br_2 from the cathode to the anode, because Br_2 exists in solution as the negative Br_3^- species. Bromine at the anode would react directly with the zinc deposit and reduce the battery capacity. Ion-selective membranes have a clear-cut coulombic efficiency advantage over porous separator materials. However, porous separator materials are less costly. Depending on the specific battery application, a coulombic efficiency vs. cost trade-off may be undertaken with regard to the choice of separator materials. Our recent work has emphasized the use of microporous membranes along with a low cost electrolyte additive which enhances the membrane's ability to retard bromine diffusion.

d.) End Block - Electrodes, spacers, and membranes can be conveniently assembled into stacks. The ends of each stack are bolted between plastic feed blocks which provide the external manifold connections and hold the electrodes in a uniform compression. Figure 0-3 shows a stack of 52 electrodes manifolded together between end blocks.

Electrolyte - The zinc-bromine battery system uses an aqueous electrolyte having two components, zinc bromide salt and a bromine complexing agent. These components are low cost, i.e., they are readily prepared from commercial items. The typical concentration of the electrolyte in the discharged state is: 3 M $ZnBr_2$, and 1 M bromine complexing agent. In typical operation, 70% of the $ZnBr_2$ is converted to Zn^0 and Br_2 at full charge.

a.) Zinc Bromide is the active ingredient of the electrolyte. It is the participant in the electrode reactions, and it is the major ionic current carrier. Zinc bromide provides a cell voltage of about 1.75 volts, and except for internal electrolyte resistance, there is virtually no cell polarization.

b.) The Bromine Complexing Agent is based on quaternary ammonium chemistry. This complexing agent was selected after a screening program which considered several classes of Br_2 complexing agents. The present agent was chosen because of its highly reversible complexing of bromine, superior chemical stability, lack of toxicity, miscibility with zinc bromide solutions, and its potential low cost. The use of a complexing agent reduces the aqueous Br_2 concentration in the aqueous electrolyte by 10 to 60-fold. This retards Br_2 diffusion across the microporous membrane and also Br_2 attack of the plastic components. The complexing agent also reduces H_2 evolution and improves plating at the anode.

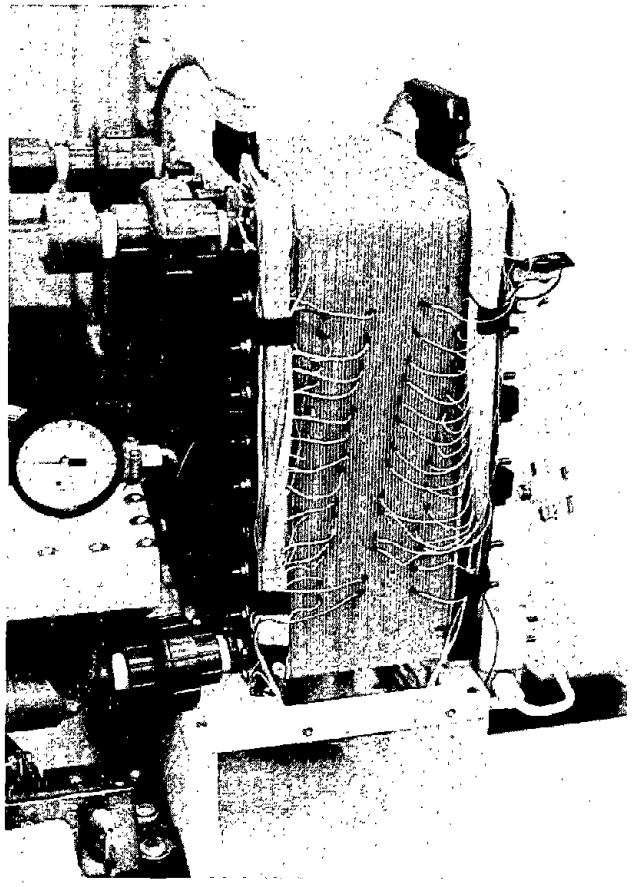

Figure 0-3 52 Cell Bipolar with End Blocks

The Circulation Equipment - The pumps and reservoirs for circulating the zinc bromine battery system's electrolyte are a distinct departure from standard lead-acid battery technology. The ability to flow and to store the electrolyte external to the cell has many advantages. Flow mixes the electrolyte and prevents the growth of zinc dendrites on the electrodes. All batteries "gas", and a flowing electrolyte removes the gaseous by-products and simplifies cell maintenance. Heat removal is also simpler with a circulating system. Since most of the electrolyte is located external to the cell, the electrode spacing can be reduced, and the cell, therefore, has a lower internal resistance. Power consumption by the circulating system can be designed to be a small fraction of the battery output. Finally, the external storage of Br_2 avoids the basic problem of self-discharge to a large degree.

a.) Pumps - Early small-scale laboratory testing utilized both peristaltic and centrifugal pumps. Practical larger designs favor centrifugal pumps which are magnetically coupled to either AC or DC motors, depending on use. Present small commercial centrifugal pumps can deliver close to 20% overall pumping efficiencies and larger pumps can be even more efficient.

b.) Reservoirs - The present reservoirs are simple polypropylene or polyethylene tanks. The cathode reservoir has separate withdrawals for the aqueous phase and for the dense bromine oil. However, a portion of the bromine oil is recirculated during charge to promote mixing of the two phases and to prevent stratification which decreases the effectiveness of the complexing agent.

0.2.2 20 kWh Photovoltaic Battery Design Approach:

Initial consideration of photovoltaic battery applications has focused on domestic grid connected storage systems with total capacity between 15 and 30 kWh. A desirable system must combine long life, low initial cost, high turn-around efficiencies, high terminal voltage, low maintenance and various other features. Similar features are desired in other advanced battery applications such as bulk energy storage and vehicle traction. Therefore, it is prudent to develop a basic zinc-bromine battery design that can be adapted to various advanced applications with a minimal amount of customization. This approach is attractive because it encourages the development of a common core battery technology which minimizes early development costs, while offering nearly identical final products for various applications. Thus, a larger possible market is created, and there should be a more rapid entry into volume production.

The initial design approach was based on existing bipolar electrodes having an active area of 600 cm^2. These were arranged as shown in Figure 0-4. The system building block was a stack of 52 bipolar cells giving a nominal discharge of 80 V. Operating at present efficiencies and loadings (90-100 mAh/cm^2), each stack has a discharge capacity of 3-3.5 kWh. Running six stacks in parallel produces a net 20 kWh battery. Reservoirs and pumps are located below the stack for a compact design. The initial attractiveness of the bipolar design was made possible by cost reductions arising from the use of carbon plastic electrodes. However, complete realization of this design required the development of a novel means of controlling shunt currents (Section I.3). The design of the 20 kWh (X-20) battery for Phase II is shown in Section IV, Figure V-2. The six stacks in this X-20 design are less compact than the design in Figure 0-4 to allow for access during laboratory assembly and operation.

This original design approach will eventually be superseded in Phase III by an advanced 20 kWh design (Sections I.1 and I.2) which uses larger electrodes (1200 cm^2), larger stacks (78 cells) and therefore, fewer modules (2). Cost reductions provide the principal driving force for these recent modifications in the ultimate system design.

0.2.3 Historical Perspective

Exxon's present concept of the circulating zinc-bromine battery is based on a number of contributions. Original patent literature on the zinc-bromine battery is nearly 100 years old. Recent development in the late 1960's was spurred by circulating electrolyte design work at Magneti-Marelli (3) and work on separable bromine complexes at Eco-Control (4). In the early 1970's, several attempts (5, 6, 7, 8) to develop circulating zinc-bromine batteries were made. Differences between these approaches are discussed elsewhere (9).

Significant events in the development of the Exxon system are chronicled below, in order to provide a brief historical perspective on recent developments. The basic technical innovations required to create a battery appear to be "in-hand", so that the major effort is now in scale-up and demonstration rather than innovation that might involve major redesigning of the system.

Nominal Capacity	**20kwh**
Specific Energy	**65-70wh/kg**
Energy Density	**80-85wh/l**
Specific Power	**80-100w/kg**
Energy Efficiency	**65-70%**

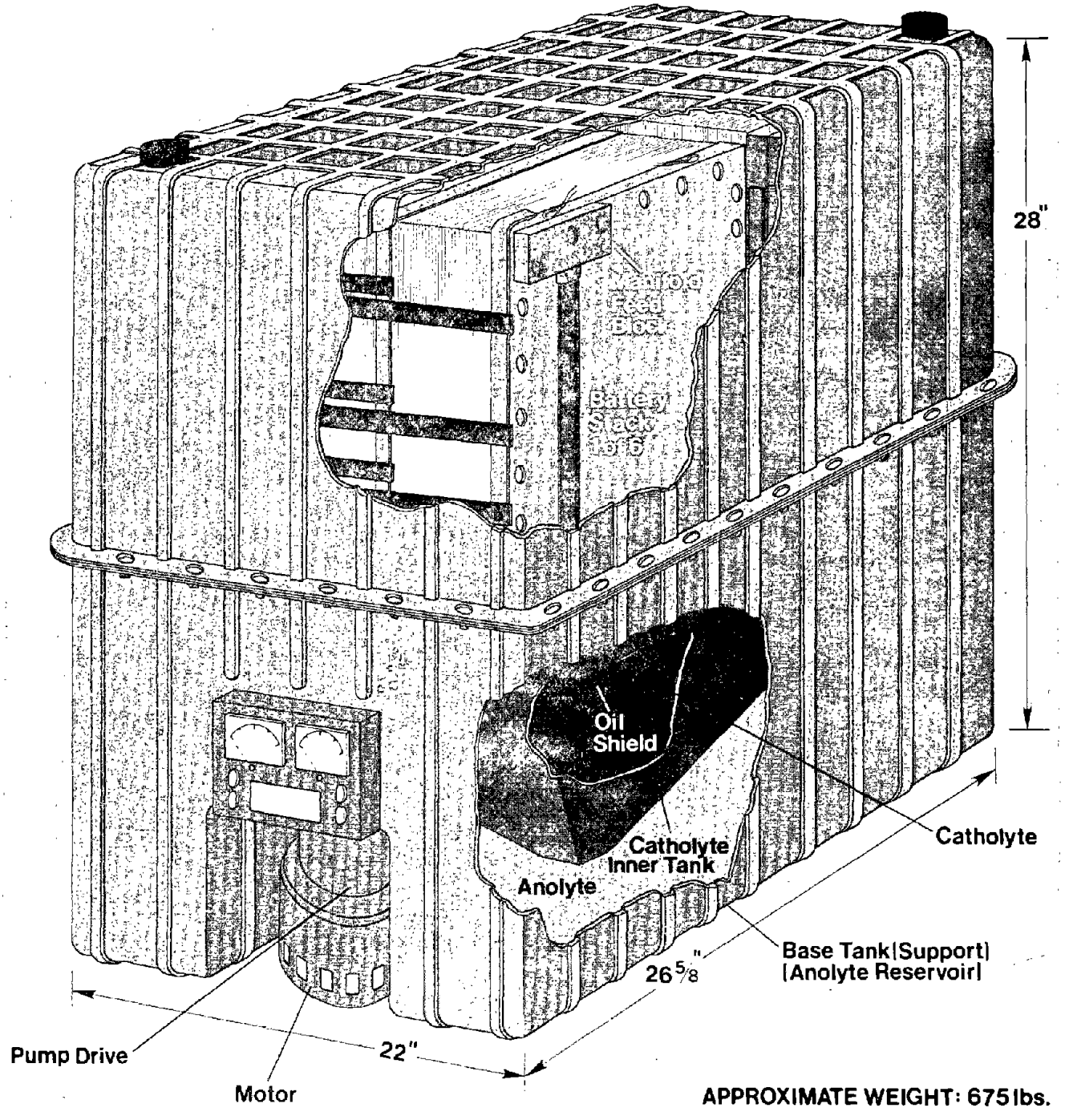

Figure 0-4 Conceptual 20 kWh Zinc-Bromine Prototype Design

Time	Events in Exxon's Circulating Zinc-Bromine Development
1959-1964	Circulating electrolyte fuel cell program at Exxon
1970-1977	Fuel cell partnership with French company - Alsthom, C.G.E. Provides initial circulating electrolyte module (fuel cells). Shunt currents observed in fuel cell and electrolyzers.
1972	Conductive carbon plastic invented by Exxon fuel cells group. Carbon plastic incorporated in fuel cell modules.
1975	Fuel cell flow components used for Zn/Br_2 battery. Cathode catalytic layer developed.
1976	Br_2 complexing agents screened and selected. Shunt currents observed in bipolar stacks. Shunt current protection concepts developed. Ion-selective membranes utilized.
1977	50 cycle - 50 Wh data - bipolar and monopolar designs - 100 cm^2 electrode. First electrode production in United States - compression molding. Shunt current protection tested in glassware simulation. Insert injection molded electrodes - 100 cm^2.
1978	Microporous separator with electrolyte additives developed. First 500 Wh and 1 kWh batteries - 100 cm^2 electrodes. Shunt current protection demonstrated in zinc bromine battery. Public demonstration of 500 Wh battery at EV Expo II. Scale-up decision to 600 cm^2 bipolar electrodes. 600 cm^2 compression molded electrodes manufactured.
1979	Shunt current protection demonstration in 500 Wh and 3 kWh 600 cm^2 electrodes. Daramic microporous separator used with electrolyte additives. Protective electrodes developed. Tunnel shunt current protection concepts improved. Automatic cycle testing - 50 Wh monopolar - 100 cm^2 electrodes.
1980	DOE/Sandia Phase I contract begins. Injection molded bipolar electrodes - 600 cm^2. Ion selective replaced by microporous separators plus additives. 100 cycle plus testing of X-3A. Two piece unit cell design. Production cost estimates revised. Commercialization plan developed.
1981	50 cycle testing of X-10.

0.3 Photovoltaic Battery Applications

Photovoltaic (PV) generation of electricity offers the promise of a renewable energy source that could someday reduce our dependence on non-renewable energy sources, such as imported petroleum. However, the widespread use of photovoltaic energy is limited by two key problems, the initial cost of the collectors and cyclic availability of solar energy.

Battery storage of photovoltaic electricity is already being used in many small remote applications to store energy generated during the daytime for later use during periods of overcast skies or darkness. Technically, this solves the problem of cyclic availability. Most of these facilities use lead-acid batteries. In these remote applications, the value of the remote, unattended power is sufficient to justify the cost of both the collectors and the batteries. However, the total energy conservation achieved on these sites is trivial compared to present national energy consumption because of both the small number and scale of these remote sites.

Many groups are working to reduce the cost of the photovoltaic collectors and much progress is being made in this area. If the price continues to drop, then domestic sized photovoltaic units could be an attractive market. However, at this point, the cost of the batteries, at current lead-acid prices, will be a major fraction of the system cost. Photovoltaic systems without batteries can augment electrical grids in various residential situations. However, a recent study (10) has shown that low cost photovoltaic systems with battery storage could make significant reduction in utility power demand, therefore reducing present fossil fuel consumption. This study does make the point that the desirability of these PV/battery systems will depend on various factors such as local insolation and utility rates and at least a factor of two reduction in present battery costs ($100-150/kWh).

The model developed in the above study, called Solstor, is shown in Figure 0-5. It shows a typical home connected to a utility grid. In addition, solar panels can be used to power the residence or feed into the grid via a DC/AC inverter, or to directly charge the battery storage system. Later, during dark periods, energy stored in the battery can be fed to the house or the grid via the inverter. Through careful sizing, the grid becomes an extended load leveling system, supplying peak power demands and absorbing excess storage capacity. The final report for this study includes a full description of the range of variables studied including collector and battery costs, system maintenance and life, siting considerations and various possible utility rate structures (10).

A typical crystalline silicon photovoltaic output in full sunlight is shown in Figure 0-6. Maximum solar power generation for this cell occurs at about 0.5 V. The effect of reduced insolation at 25% and 50% full sun is approximately shown by the dashed line. This reduced insolation could be either from haze or from the angular incidence of the sun on the collectors.

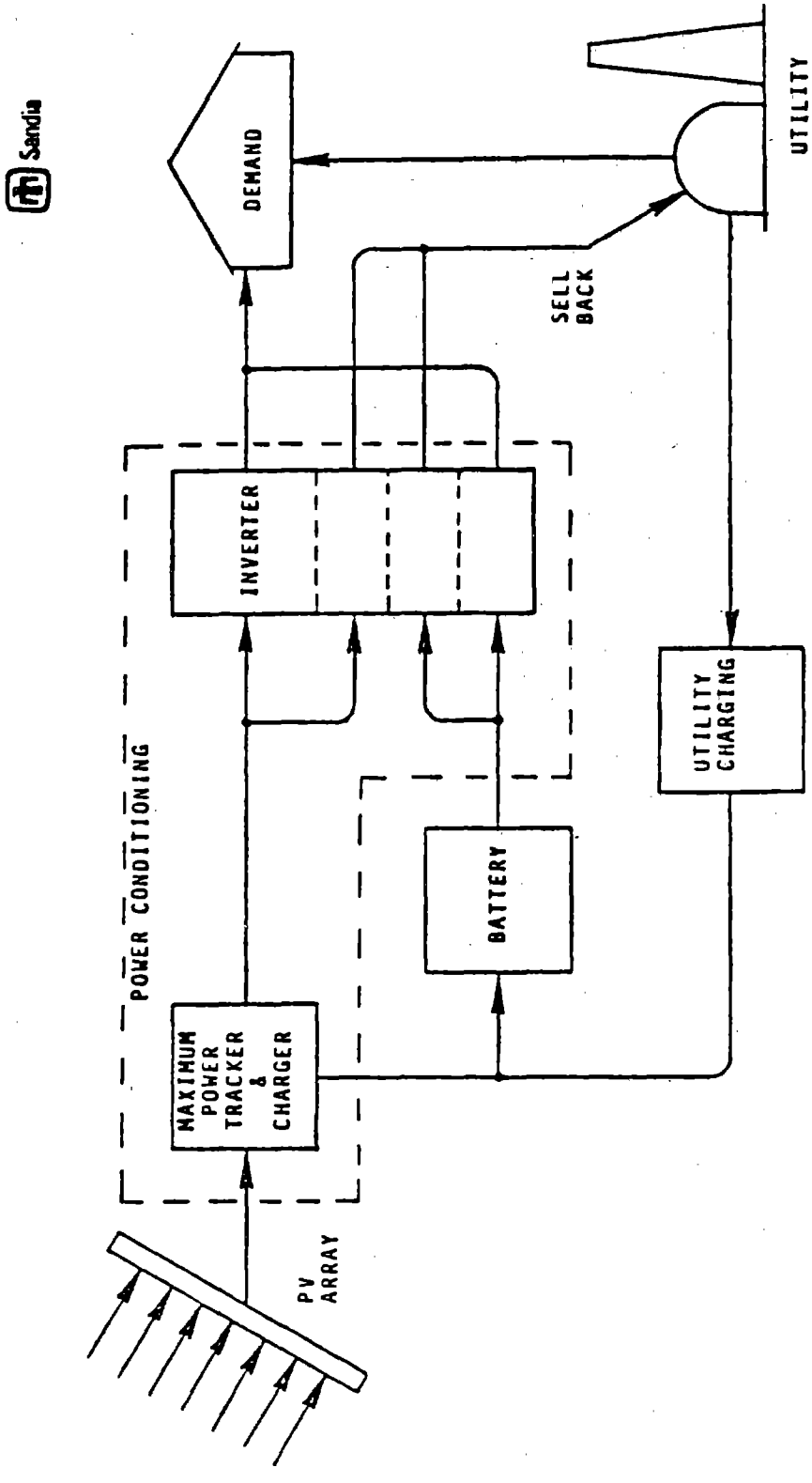

Figure 0-5 Solstor Model (10)

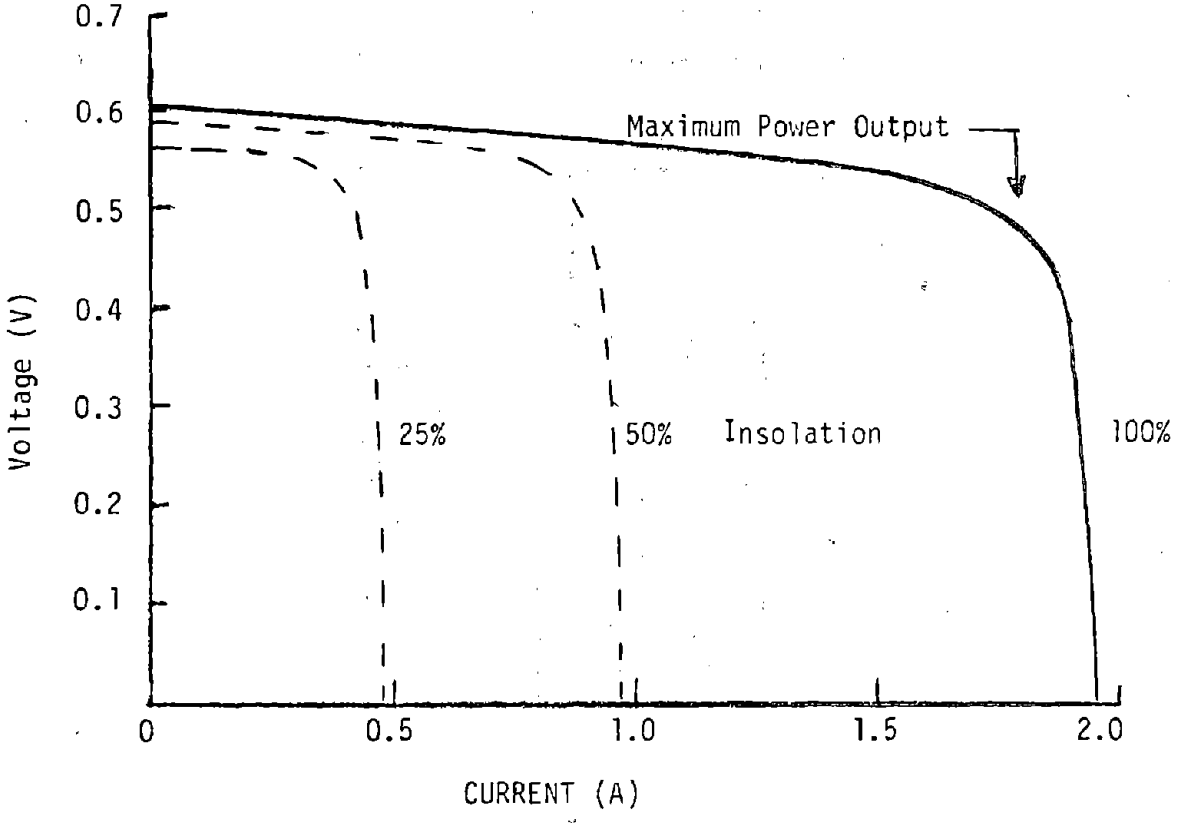

Figure O-6 Solar Power Generation -
Crystalline Silicon Cell

A possible direct interfacing of a 20 kWh zinc-bromine battery to an array of solar cells is shown in Figure 0-7. The photovoltaic array is based on 30 parallel strings, each with 180 solar cells in series or a total of 5400 individual solar cells. The charging curve for Exxon's zinc-bromine battery is plotted on the same coordinates. The actual battery rate would be given by the intersection of the charging curve with the solar generation curve at the appropriate level of insolation. This interfacing was designed so that all photovoltaic energy would be used to charge the battery. In this design, the relative slopes of battery charge and solar array have been designed so that the battery charging rate is always near the maximum solar power generation point, regardless of insolation rates, so that full use is being made of the solar cells' capacity. In the Solstor model, a significant fraction of the power would also go directly into the residence via the inverters. In this case, more solar cells in parallel (for example, 60 parallel strings) would be required with the power of these extra strings supplying the average house demand. These curves illustrate some of the considerations in the coupling and sizing of zinc-bromine batteries to various solar arrays.

Solar Array = 180 Cells in Series X 30 Cells in Parallel

Zn/Br_2 Battery = 20 kWh Capacity

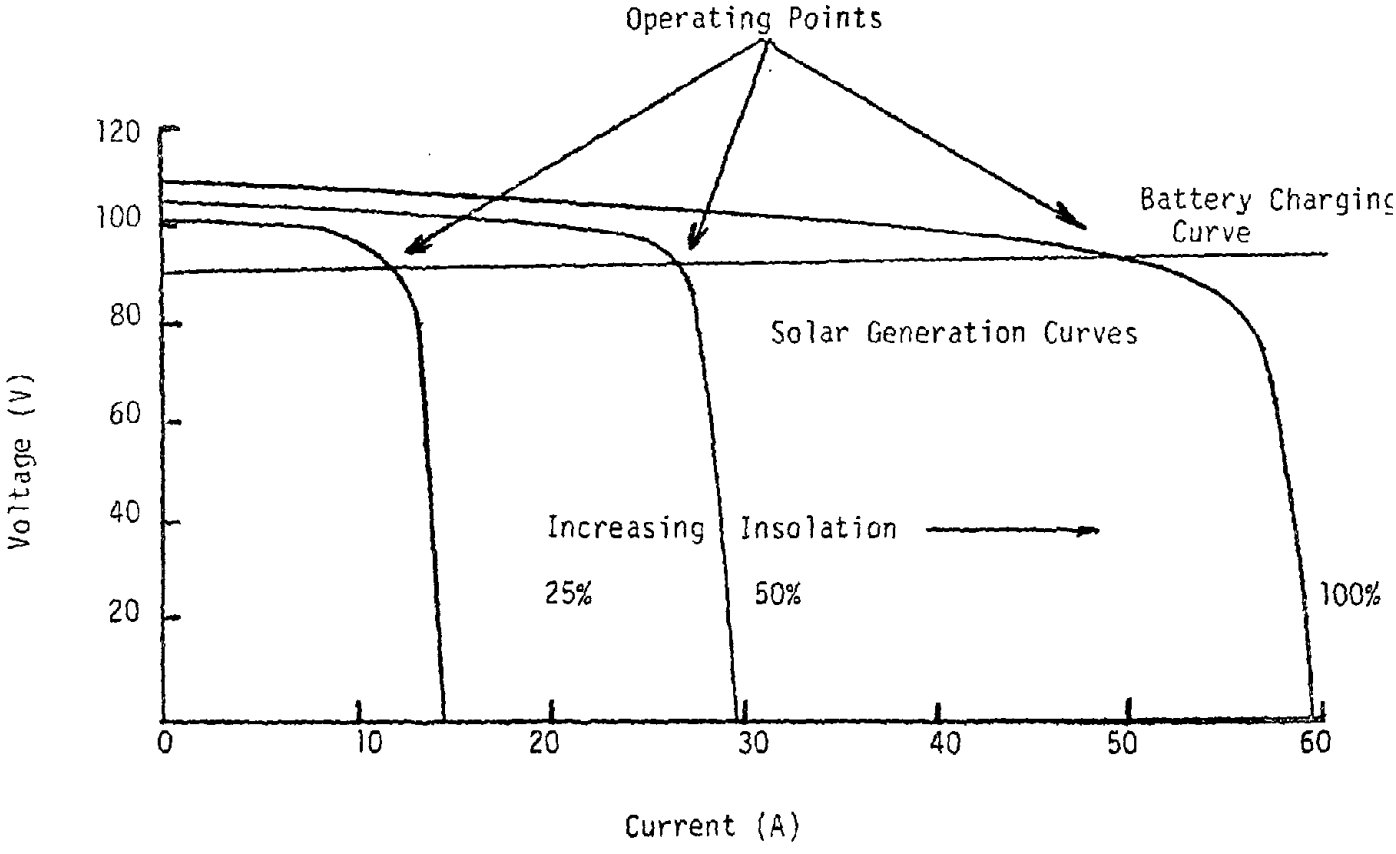

Figure D-7 Direct Interfacing of Solar Array and Zn/Br_2 Battery

I. Design, Costing and Planning Studies

Initial work on Exxon's circulating zinc-bromine battery (1) indicated that it was an attractive advanced battery technology with potentially high performance, long cycle life and low initial cost. This section describes recent studies concerned with specific design concepts that have evolved during Phase I, and the impact of these design concepts on the projected manufacturing cost. Finally, a possible timetable for commercialization of the Zn/Br_2 battery is presented, which delineates specific development targets and milestones.

I.1 Engineering of Advanced 20 kWh Design

During Phase I, a number of design concepts have coalesced. These included the initial development of an extremely low-cost two-piece unit cell (Section II.7), tunnel shunt current protection (Sections I.3 and IV.2), manifold flow distribution (Section IV.5.1) and a revised production cost estimate (Section I.2). With the new two-piece unit cell, the cost of interior electrodes dropped to the point that the cost of the "ends-of-the-stack," i.e., the current collectors, protective electrodes, electrical and plumbing connections and multiple stack assembly, became significant cost reduction targets. Calculations and data on tunnel shunt current protection and manifold flow distribution allowed larger numbers of cells to be placed in series. Easy scale-up of the electrodes from 100 to 600 cm^2 and their successful demonstration in 3 kWh and 10 kWh units increased confidence in further electrode scale-ups.

These inputs gave rise to a new two-stack 20 kWh design based on the present electrode and electrolyte performance, but with electrode area doubled to 12 dm^2 and with each stack increased to 78 cells giving a nominal 120 V discharge. This design is shown in Figure I-1 and otherwise resembles the earlier 20 kWh described in section 0.2.2. By reducing "ends-of-the-stack" from the previous design, the advanced 20 kWh design should be cheaper and faster to produce.

Initial scale-up studies on electrode flow distribution will be part of Phase II. Final design of the optimized Phase III 20 kWh deliverable will await the result of these scale-up studies. Meanwhile, other program activities such as reservoir sizing, materials selection, pump development, controller development and most other system parameter modifications can procede unchanged because of the obvious similarities between these two 20 kWh designs.

I.2 Costing of Advanced 20 kWh Design

Battery Costing Analysis

A study of direct factory costs to produce this advanced 20 kWh design was conducted at various production rates. The costing methodology assumed an assembly type operation where most of the components would be purchased from outside vendors. Estimates of purchased components

CELL CONSTRUCTION

Each Cell consists of one injection molded plastic frame around a Daramic insert and a carbon-plastic bipolar electrode co-extruded with an insulating plastic top and bottom.

BATTERY CONSTRUCTION

Battery consists of two cell stacks of 78 cells each. Active electrode area 11 inches high × 16⅜ inches wide (180 sq. in).

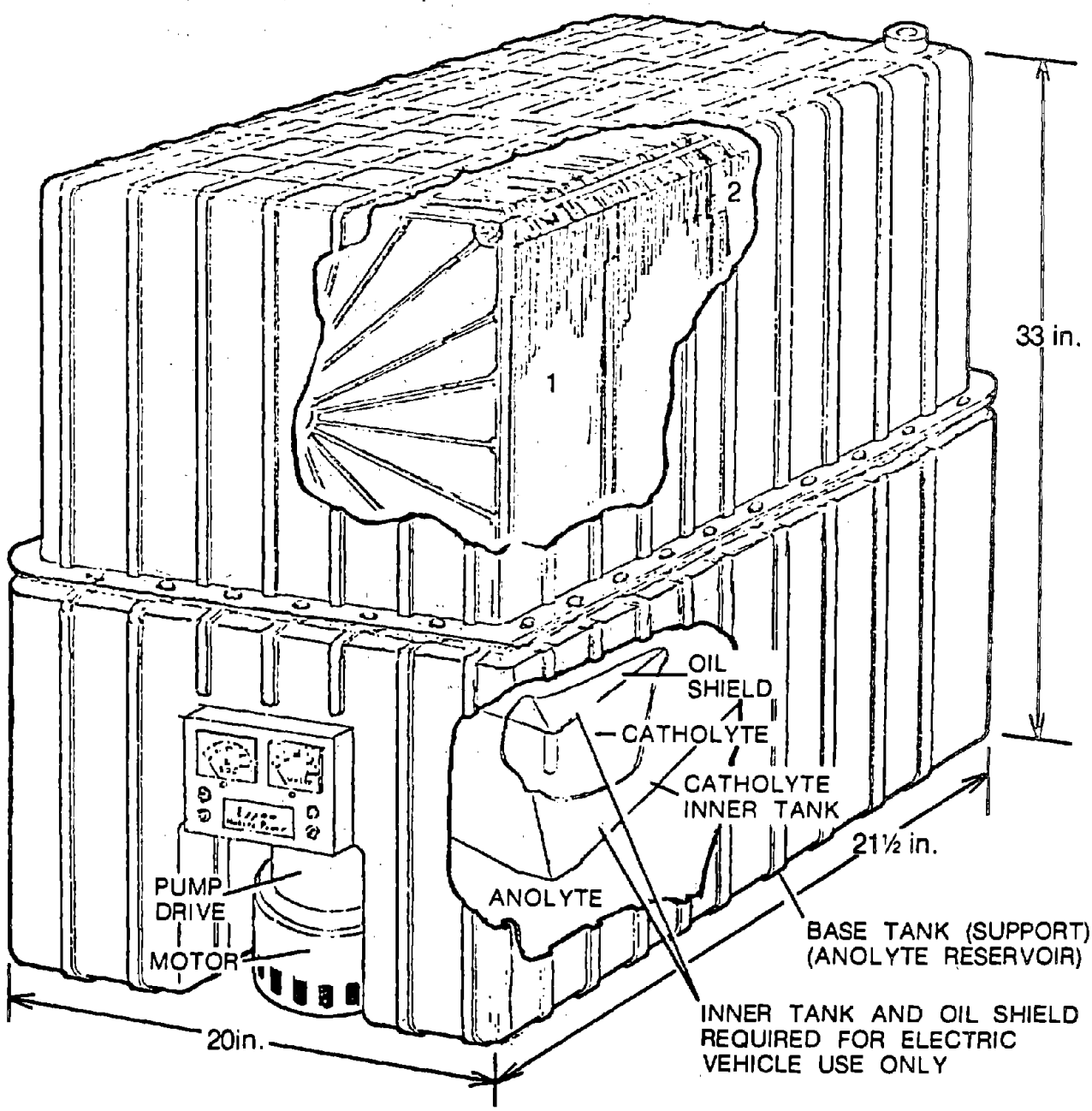

Figure I-1 Advanced 20 kWh Design

are based on present quoted costs of machine and operator. Accessory items, not yet fully defined, (pumps, controllers etc.) are best estimates. In-house factory labor estimates are based on station by station time estimates as anticipated after the second or third year of operation, when the problems of initial start-up have been solved. In-house labor consists primarily of the assembly of battery stacks, the attachment of the stacks to the reservoir, installation of accessories and final testing of the assembled module.

The assembly plant approach has both advantages and disadvantages. Quotes from experienced vendors are likely to be more reliable than in-house estimates of component fabrication, thus uncertainties in the cost estimates are reduced. In limited production, extensive use of outside vendors is likely because this approach reduces capital and labor requirements where full time production personnel are not required. Thus capital, labor and space are required only for the final assembly.

However, the "assembly plant" approach tends to be conservatively high for large scale production estimates. Dependence on several outside vendors would require higher inventories and more lead time for coordinating production. In large scale production, plastic fabrication machinery (the largest capital expenditure) could be occupied full time. Therefore a shift to total in-house production would undoubtedly reduce costs by eliminating intermediate overhead and profits as well as inventory requirements. Future studies will investigate a more integrated in- house plastic fabrication approach.

The term 'factory cost' includes most direct charges for assembly of 20 kWh units. It includes required raw materials, purchased components, accessories, direct labor costs, worker benefits, quality control and supervision. It does not include indirect charges such as inventory costs, depreciation of plant and equipment, working capital, tooling, sales and general administration costs, development costs and return on investment (ROI). Various estimates of these indirects were made, including the A. D. Little method. These costs are not included in this report because of the differences arising out of the various methods of predicting indirect costs.

An overview of the factory cost study for this 20 kWh battery indicates the factory cost to be $28/kWh at a production rate of 100,000 units per year (1980 dollars). Various indirect costs as described above need to be added to arrive at the selling price (OEM). Figure I-2 is a 'pie chart' cost breakdown showing the major costs such as purchased stack and reservoir parts, accessories, electrolyte and in-house labor. The low in-house labor percentage reflects the assembly plant viewpoint since labor is required only for final assembly. Additional labor and overhead are included in the cost of purchased components. A more complete breakdown is shown in Table I-1. Major cost items are the battery stack components (bipolar electrodes, separator assemblies and current collectors) and the electrolyte. Detailed cost analysis of these and other items can be found in Appendix 2.

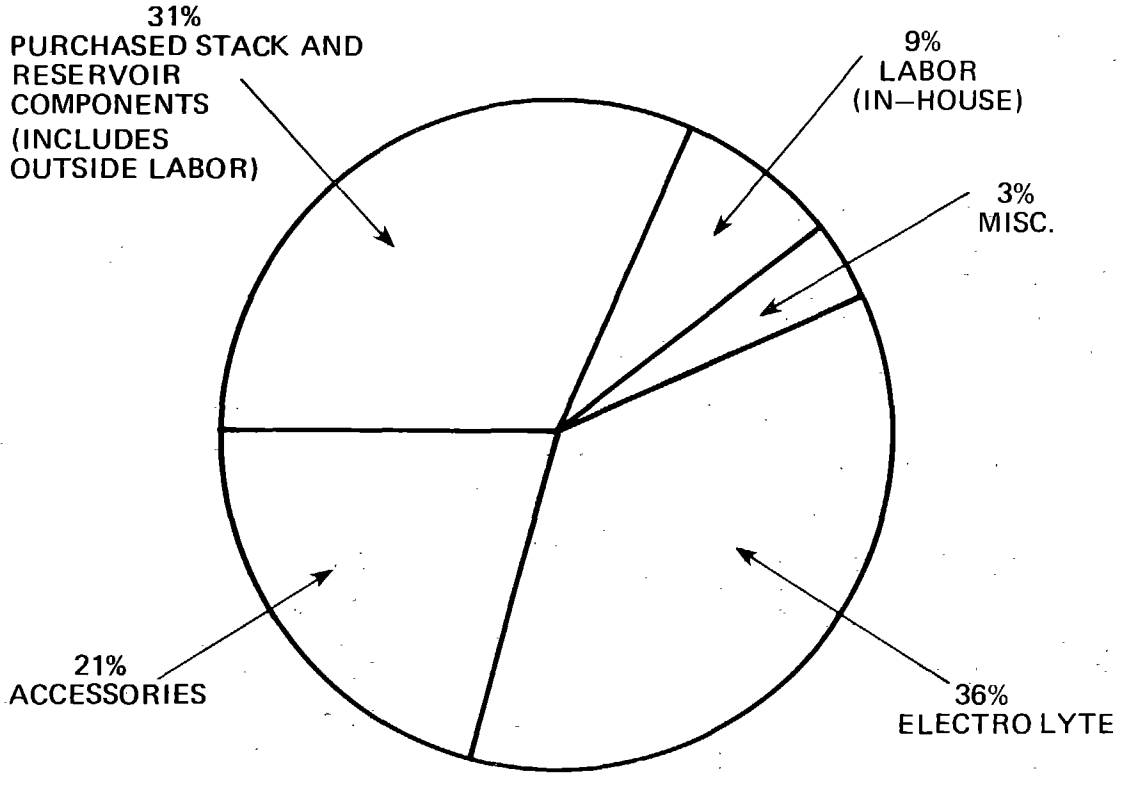

FACTORY COST: $28.05/kWh

20 kWh ZINC-BROMINE – FACTORY COST BREAKDOWN

(100,000 BATTERIES/YEAR)

Figure 1-2 Factory Cost Analysis

TABLE I-1

TOTAL FACTORY COST*

20 KWH ZINC-BROMINE BATTERY

ITEM OR ASSEMBLY	100K Batteries/Year ($)
Bipolar Electrodes	38.30
Current Collectors	28.20
Separator Assembly (Incl. Outside Labor)	77.44
End-Support Block Assembly	10.52
Center-Support Blocks (Incl. Outside Labor)	10.36
Reservoir	8.59
Reservoir Tray	2.95
Battery Stacks - Total	176.36
Electrolyte Pump	24.00
Electrolyte Pump Motor	16.00
Isolating Drive System	10.00
Bromine Pump Head	4.00
Bromine Pump Motor	6.00
Pump Press Sensor	4.00
Electrolyte Level Sensor	2.00
State-of-Charge Sensor	4.00
Voltage Cut-out	1.50
Temperature Probes (3)	3.00
Electronic Circuit Board	12.00
Hydrogen Recombination	2.00
Plumbing & Fittings	10.00
Bus Bars - Tie Rods & Hardware	20.00
Batt. Access., Controls, Etc. - Total	118.50
Electrolyte	200.00
Packaging & External Case	18.49
Materials - Total	513.35
In-House Labor	47.75
Factory Cost Total, $/Unit	561.10
Factory Cost Total, $/kWh	28.05

*Excludes various indirect costs such as G & A, ROI, and cost of sales

I.3 Design Concepts in Shunt Current Protection

The development of a novel technique for controlling the effects of shunt currents in bipolar stacks was a major milestone in Exxon circulating zinc-bromine battery. This new technique is called shunt current protection. It uses auxiliary currents in the common manifold or "tunnels" to voltaically nullify shunt currents.

Cell Stack Design Considerations

Bipolar vs. Monopolar

In addressing the development of a large zinc-bromine battery at low cost, the desire to use conductive plastic components leads to an important decision in terms of stack design. In earlier Zn/Br_2 development, both monopolar and bipolar designs were tested. These designs are shown schematically in Figure I-3. At the cell level, performance and life of both designs were virtually identical. However, the need for implanting screens in monopolar electrodes was an added expense. In contrast, bipolar electrodes offer a distinctively simpler and cheaper stack design. In addition, the higher voltage of bipolar designs can be interfaced economically with high voltage chargers and DC motors. By comparison, monopolar stack designs require the additional expense of external bus bars to obtain equally high terminal voltages.

Shunt Current Considerations

Unfortunately, continuous cycling of bipolar stacks with a common circulating electrolyte is plagued by parasitic (shunt) currents. Shunt currents 'flow' from the high potential regions to the low potential regions of the series of cells via the common electrolyte during charge, open circuit and discharge conditions. There are reduction processes at the high potential regions and oxidative processes at the low potential regions. In the Zn/Br_2 battery, these shunt currents cause zinc to plate more rapidly near the manifold connections at the negative end of the bipolar stack. As this zinc accumulates, it grows into the electrolyte manifold, thereby disrupting normal electrolyte distribution. Without stable circulation, the plating becomes non-uniform, and the cell eventually fails.

Physics of Shunt Currents

Figure I-4a and 4b show a simplified explanation of shunt currents in a string of battery cells which are connected electrically in series and fed by a single common electrolyte manifold. Ideally, any currents passing into an end electrode pass equally through each electrode in the series. However, the conductive electrolyte in the common manifold forms an alternate pathway in parallel with the series-connected cells. These parallel pathways allow a certain portion of the terminal currents to bypass or shunt around the central electrodes in the series. (Figure I-5).

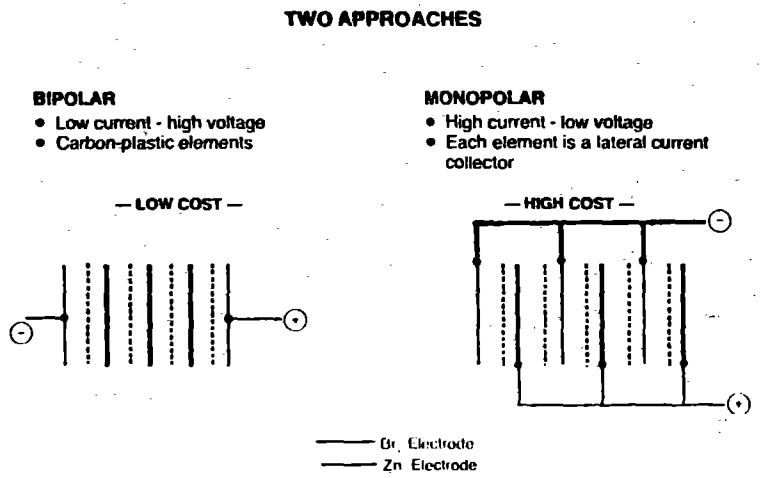

Figure I-3 Bipolar vs Monopolar Stack Design

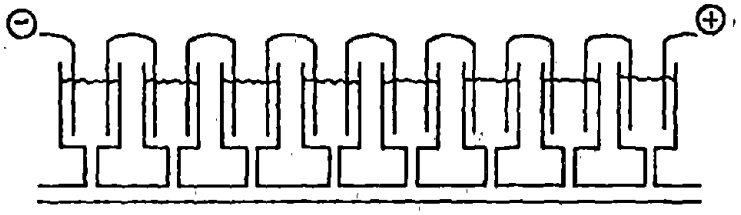

Figure I-4 Series Connected Cells with Common Electrolyte Manifold

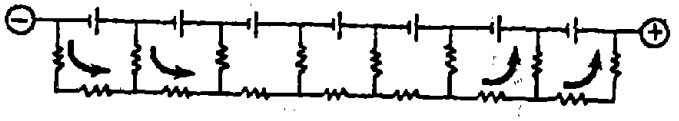

Figure I-5 Electrical Analog of Shunt Currents

Early work on bipolar designs with short stacks showed that the detrimental effects of non-uniform zinc growth due to shunt currents could be avoided by cycling the battery with excess Br_2 and completely shorting the stack at the end of discharge. During shorting, the excess Br_2 erased all stray zinc growth. Eight-cell bipolar stacks showed stable operation over 100 cycles by using this shorting technique. However, this technique works best for small bipolar stacks and would probably be ineffective in larger stacks (30 or more cells in series), where the magnitude of shunt currents becomes larger. Furthermore, the complete shorting of a battery after a partial discharge is an inefficient and impractical mode of operation. Since bipolar designs offer a number of incentives, a large effort was directed to understanding and controlling shunt currents. This effort led to developing a novel technique called shunt current protection.

I.3.1 Manifold Shunt Current Protection

The following analysis of series connected cells with common electrolyte shows methods of elimination of shunt currents and their effects. The effects can be eliminated in one method of applying a potential through the common electrolyte manifold. If the potential gradient in the common electrolyte manifold equals the potential gradient across the series of cells, there is no potential gradient between the cells and the manifold and no shunt currents flow. In order to attain this condition of potential gradient matching, a current must flow through the manifold. The shunt current elimination by the passage of current through the manifold is called manifold protection. The magnitude of the manifold current, k_o, as seen below, is defined as:

$$k_o = \frac{\text{cell voltage}}{\text{resistance of a manifold segment}}$$

Another method of protection involves passage of a current through interconnects between the channels which connect the manifold to the cells. These interconnections are called tunnels and, thus, the method is called tunnel protection.

I.3.2 Shunt Current Model Analysis

The lumped resistive equivalent circuit of series connected cells with common electrolyte and the governing difference equations are shown in Figure I-6. Kirchoff's Law expressions can describe loop equations. Difference equation analysis, described in Appendix 3 leads to the expressions for the currents in various portions of the system shown in Figures I-7 and I-8.

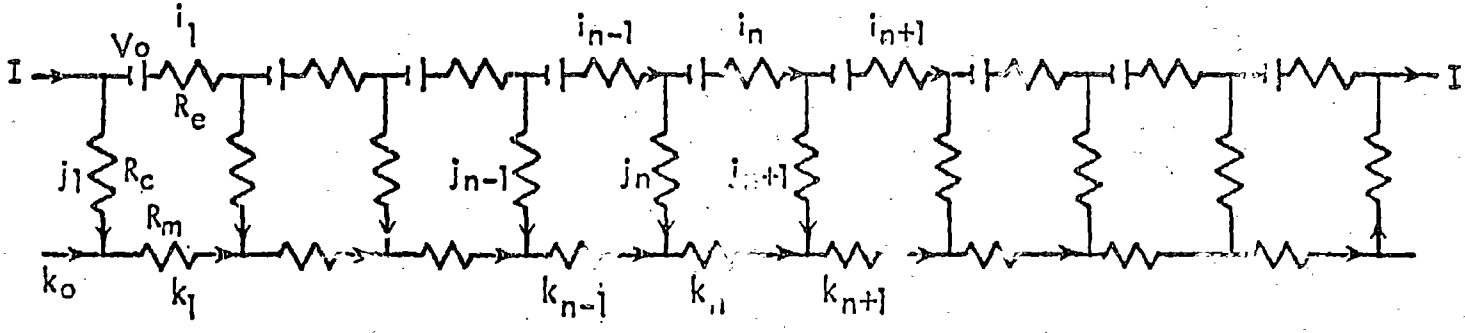

$$I_{n-1} = i_n + j_n;\ k_n = k_{n-1} + j_n;\ k_{n-1}R_m - (j_n - j_{n-1})R_c - i_{n-1}R_e - V_o = 0$$

Fig. I-6 Lumped Resistive Equivalent Circuit with Governing Difference Equations

The values for the resistances:

R_e = internal cell resistance per manifold, ohms
R_c = channel resistance, ohms
R_m = manifold segment resistance, ohms

can be determined from the geometry of the system and electrolyte conductivity.

These values are used to determine β and then λ. The cell open circuit potential, V_o (volts), and the terminal system current/per manifold $\pm I$ (amps) are specific operating parameters.

N is the number of cells in series. The value of the first channel shunt current $J = j_1$ can then be determined from λ, N and $(V_o + IR_e)$.

The values of:

j_n = nth channel shunt current
k_n = nth manifold segement current
i_n = nth cell current per manifold

can be determined from J and the formulas in Figure I-8.

Shunt Current Elimination Manifold Protection

The mathematical model leads to a k_o current, inserted into the manifold. The expression for the J current, Figure I-8, involves a minus k_oR_m term. When the value for k_oR_m is equal to $(V_o + IR_e)$ then the numerator of the J equation is zero, and there are no channel shunt currents. Under these conditions, the following expressions hold, namely:

$j_n = 0$
$k_n = k_o$
$i_n = I$

The shunt currents are thus eliminated when a current of value:

$$k_o = (V_o + IR_e)/R_m$$

is passed through the manifold.

Ideally, the voltage drop, V_t, through the manifold from the first to last cell is:

$$V_t = (N-1)(V_o + IR_e)$$

In practical systems, currents approaching this value will effectively eliminate problematic shunt current effects in a zinc-bromine battery system. Shunt currents in practical size and voltage zinc-bromine bipolar batteries are mainly determined by the number of cells in series, and the geometry of the electrolyte supply system. The effects are larger with higher voltage systems (large N).

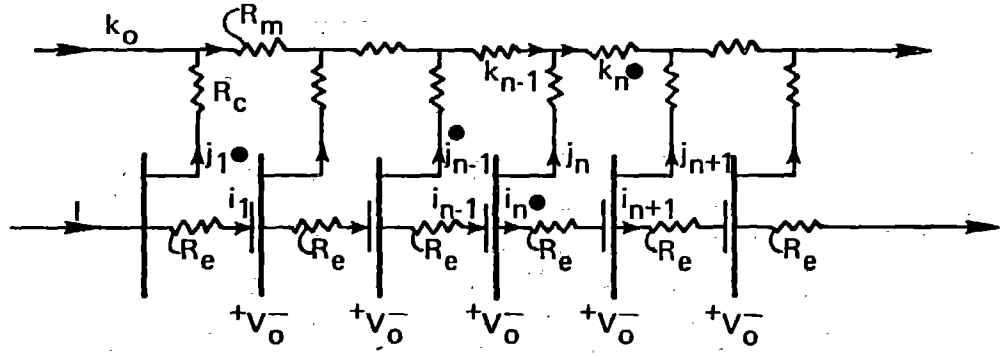

$$i_{n-1} = j_n + i_n \qquad k_{n-1} = k_n - j_n$$

$$\circ\ j_n R_c + k_n R_m - j_{n+1} R_c - i_n R_e - V_o = 0$$

$$\circ\ j_{n-1} R_c + k_{n-1} R_m - j_n R_c - i_{n-1} R_e - V_o = 0$$

$$j_{n-1} - \beta j_n + j_{n+1} = 0$$

$$\beta = 2 + \frac{R_m + R_e}{R_c}$$

Figure I-7 Electrical Analog of a Common Electrolyte System

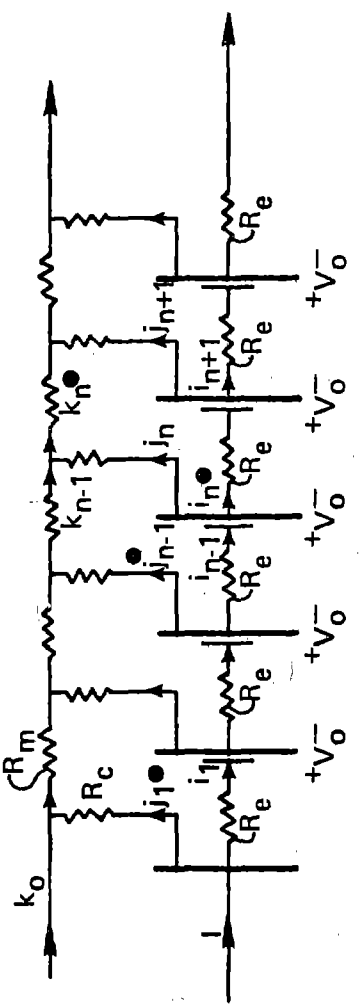

- $j_n = J\left[\dfrac{\lambda^{N-2n+1} - \lambda^n}{\lambda^N - \lambda^n}\right]$ $\qquad \sum_1^n j_n = J\dfrac{\lambda}{(\lambda-1)}\left[\dfrac{\lambda^n + \lambda^{N-n-1} - \lambda^N}{(\lambda^N - \lambda)}\right]$
- $k_n = \sum_1^n i_n + k_o$ $\qquad \lambda = \dfrac{\beta}{2} \pm \sqrt{\left(\dfrac{\beta}{2}\right)^2 - 1}$
- $i_n = 1 - \sum_1^n i_n$ $\qquad \beta = 2 + \dfrac{R_m + R_e}{R_c}$
- $J = j_1 = \dfrac{V_o + IR_e - k_o R_m}{R_m + R_e + R_c \dfrac{(\lambda-1)(\lambda^{N-1} + \lambda)}{(\lambda^N - \lambda)}}$

Figure I-8 Electrical Analog of a Common Electrolyte System

I.3.3 Experimental Verification of Shunt Current Protection

This theory was first verified with a network of nickel-cadmium batteries and selected ceramic resistors (Figure I-6). Measured currents through the resistors in the unprotected system matched those computed from the analytical shunt current formulas under charge, discharge, and open circuit conditions. When the appropriate k_o current was inserted from a second power supply at the first R_c/R_m node, the currents in the channels stopped.

Next, a simple H_2/O_2 electrolyzer of ten cells in series with a common 1 M KOH electrolyte was constructed of glass beakers and plastic tubing, with 10 cm^2 Ni electrodes 4 cm apart (Figure I-9). A clip-on ammeter was used to measure the currents in the channels. When power was applied to the terminals, H_2/O_2 production was markedly less at the center cells. Portions of the input terminal current, S_n, were being shunted through the manifold and past the cells (Table I-2). The center cells received about 80% of the 124 mA input current. A second power supply was then connected to Ni electrodes in the manifold and various protective currents were passed through the manifold. Gas production from each cell became more uniform, and the shunt currents were markedly reduced (Table I-2).

A 12 V, 1 kWh Zn/Br_2 battery was constructed from eight monopolar substacks connected electrically in series, and supplied in parallel by common anolyte and catholyte streams (Figure I-10). Each substack was comprised of 14 plates. Each side of a plate had 100 cm^2 active area.* Zinc plates were typically charged to 60 mAh/cm^2. The total stack discharged at about 12 V, with a nominal capacity of about 1 kWh.

The four electrolyte manifolds created pathways for shunt currents between the monopolar stacks. Branched channels on the manifolds were sized so that ionic shunt currents could be measured directly with a Hewlett-Packard-428B clip-on ammeter. Electrodes for passing the protective current can be seen at the end nodes of each manifold. Shunt currents in the branched channels were measured during charge, discharge, and on open circuit, both with and without shunt current protection.

Figure I-11 shows typical data for the four manifolds during a charge cycle. Without protection, shunt currents in the branched channels were positive at the positive end of the stack, passed down the common manifold, and re-entered the stack at the more negative end of the manifold. When shunt current protection was applied, the current in each branched channel was simultaneously nulled. Imperfections in the data are due to either slight deviations in manifold geometry or to measurement error limitations of the clip-on ammeter. The nulling applies equally to all four manifolds. Equivalent behavior, with and without shunt current protection, was observed during discharge and OCV. This series-connected monopolar battery was cycled with shunt current protection over the equivalent of 50 deep-discharge cycles, including a sequence with 24 mathematically random discharge cycles. Battery performance remained stable throughout the cycling period, showing an average coulombic efficiency of about 85%.

*100 cm^2 equals one square decimeter, 1 dm^2.

TABLE I-2

ELECTROLYZER EXPERIMENTS

Example	Manifold Status	Electrolyzer Input Current (mA)	Electrolyzer Input Voltage (V)	Protective Input Current (mA)	Protective Input Voltage (V)	Channel Shunt Currents (mA) S_1	S_2	S_3	S_4	S_5	S_6	S_7	S_8	S_9	S_{10}
1	Unprotected	124	20.8	0	0	+11	+5	+2	*	+0.3	-0.24	*	-3.4	-6.3	-11.5
2	Protected	124	21.2	12.8	23.3	+1.3	+0.5	-0.1	-0.1	-0.2	-0.1	+0.6	+0.6	-0.4	-0.8
3	Protected	124	21.3	14.8	24.1	+0.1	-0.3	-0.25	-0.19	-0.24	-0.15	-0.62	+0.72	+0.55	-0.55
4	Protected	420	25.4	17.5	28.5	+0.09	+0.18	+0.24	+0.23	+0.1	+0.24	-0.72	+0.98	+0.8	-0.82

*Not measured

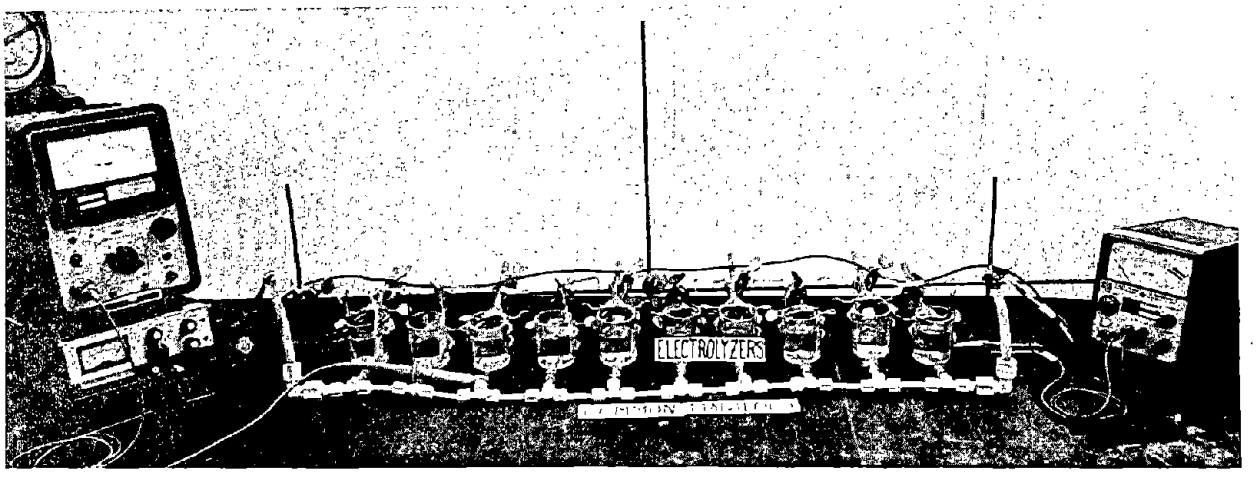

Figure I-9 Shunt Current Protection on an Electrolysis Apparatus

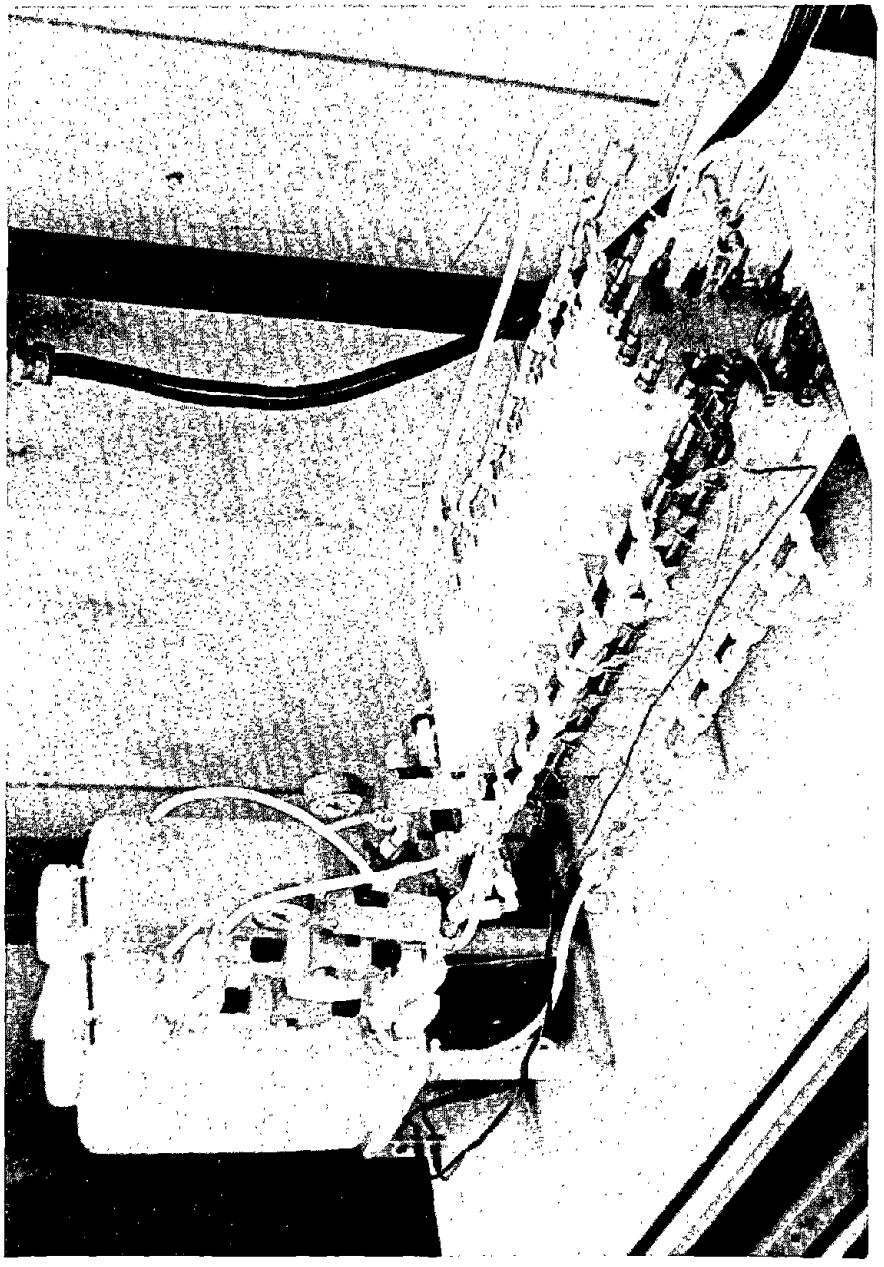

Figure I-10 Shunt Current Protection on a Series-Connected Monopolar Zinc-Bromine Battery

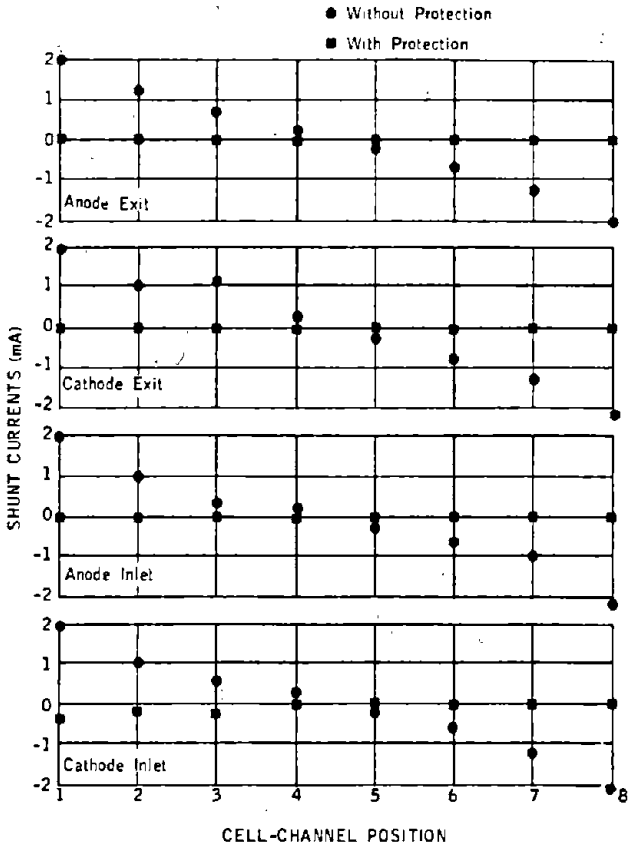

Figure I-11 Shunt Currents on 12V Stack With and Without Protection

Design Tradeoffs with Manifold Protection

Three important design aspects are critical for successful implementation of shunt current protection:

1. The end manifold node voltages must approximately equal stack voltage, NV_c. where $V_c = V_o + IR_e$
2. The common manifold cross-section must be kept small to increase R_m.
3. The manifold cross-section must be large enough for low pressure circulation.

By generalizing Figure I-4 to any number (N) of cells in series, the stack voltage will be NV_c and the voltage between the end nodes of each manifold will be $(N-1)k_oR_m$, or $(N-1)V_c$. This is an important relationship for batteries with a large internal resistance, where stack voltage can vary significantly between charge and discharge. The Shunt Current Protection concept was defined in terms of the magnitude of k_o; i.e., $k_o = \frac{V_c}{R_m}$, so that the currents needed for protection must be varied whenever cell voltages change, or whenever R_m changes because of electrolyte resistivity changes (temperature and/or concentration). This would be a messy control problem. However, if the protective electrodes can be run potentiostatically referenced to the stack voltage, variations in k_o are automatically controlled. For the generalized case of Figure I-4(c), described above, this means that $V_t = \frac{(N-1)}{N}V_c$. The simplest means for controlling the protective electrode voltages is to simply connect the protective electrodes to the battery terminals via appropriate dropping resistors. As long as $\frac{N-1}{N} \approx 1$, the voltage of the protective electrodes will be roughly potentiostated versus the stack. Whenever cell voltage changes, the protective electrode voltage will track. If the electrolyte resistivity changes, the "potentiostated" protective electrodes will simply pass more or less k_o, as required. By this technique, the control of k_o is simplified.

Uncontrolled shunt currents cause a continuous parasitic drain on series-connected batteries having common electrolyte. However, shunt current protection represents a larger dissipation of power $(N-1)k_o^2R_m$, or $(N-1)V_c^2/R_m$, than uncontrolled shunt currents. Therefore, the power consumed by shunt current protection must be kept acceptably small relative to the battery discharge power and relative to unprotected shunt currents. This means that R_m must be as large as possible. For circular common manifolds, $R_m = 4\rho\ell/\pi D^2$, so that the power consumed for protecting a manifold (protective power) equals $\frac{(N-1)V_c^2\pi D2}{4\rho\ell}$. Figure I-12 shows, conceptually, how the protective power increases as D^2. Clearly, minimizing the protective power requires as small a common manifold diameter as possible.

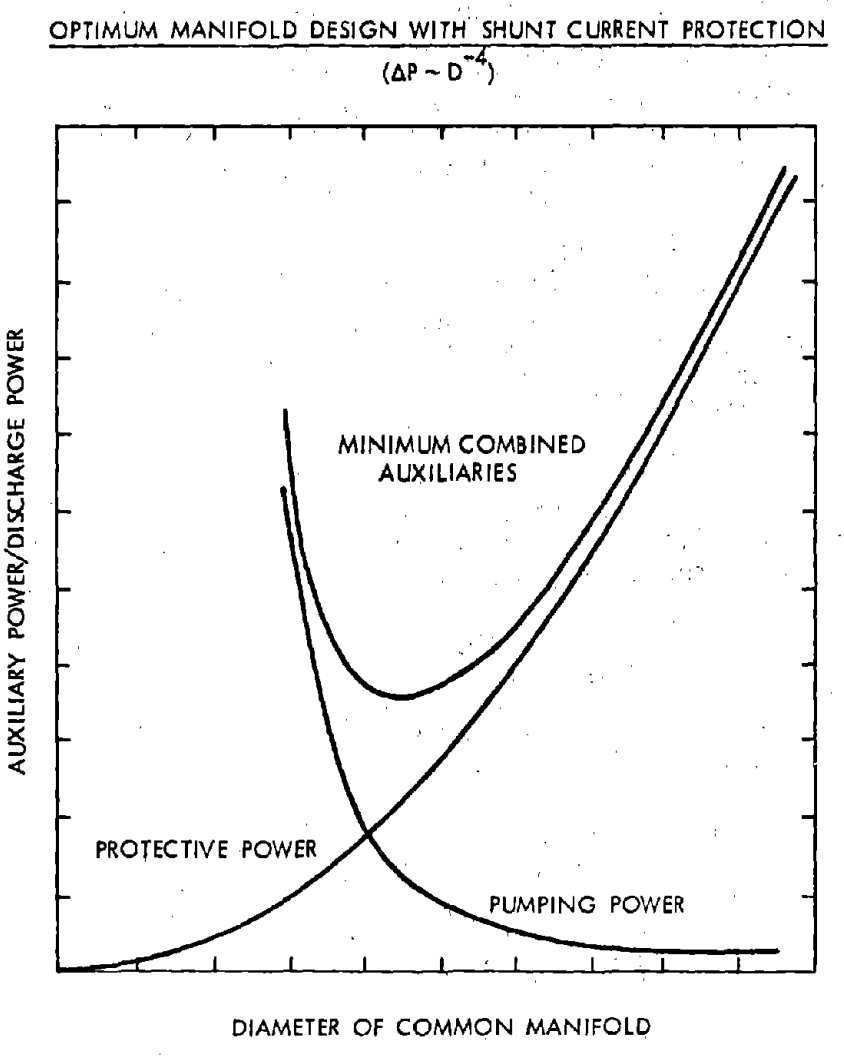

Figure I-12 Auxiliary Power Requirements

Unfortunately, as the common manifold diameter decreases, the pressure drop required to circulate the same amount of electrolyte grows rapidly. Flow studies indicate that the pumping power for manifolds in turbulent flow is approximately proportional to the inverse fourth power of the diameter. This relationship is also plotted conceptually in Figure I-12. In a circulating electrolyte battery, both protective power and pumping power represent auxiliary inefficiencies. Addition of these inefficiencies, in Figure I-12, shows that an optimum manifold diameter will exist for any battery system that minimizes these auxiliaries. Studies predict that this optimum will depend strongly on N, ρ, and the electrolyte circulation rate. Successful implementation of shunt-current protection requires that the combined auxiliary losses represent an acceptable percentage of battery capacity relative to the required mission.

The power requirements for manifold shunt current protection are determined by the number of manifolds, M, resistance of a manifold segement, R_m, and the number of cells in series, N.

$$\text{Protective Power} = MN\, V_c k_o$$
$$= MN\,(V_o + IR_e)^2/R_m$$

The power output/input of a self protected battery system is:

$$\text{Power} = M\,N(V_o + IR_e)(I + k_o)$$
$$= M\,N[(V_o + IR_e)I + (Vo + IR_e)^2/R_m]$$

The power ratio is:

$$\frac{(V_o + IR_e)/R_m}{I + (V_o + IR_e)/R_m}$$

The percentage of power for manifold protection is thus greatly influenced by both the resistance and geometry of the manifold and the total stack current.

Protection Electrodes

Manifold shunt current protection requires the passage of currents through the manifolds to provide a potential gradient. The current insertion and recovery from the manifold requires oxidation and reduction reactions at electrodes to convert from electronic to ionic currents.

Electrode reactions with the zinc bromide electrolyte in the battery manifolds could lead to zinc metal deposits at the reduction electrode. However, if these electrodes are supplied with a bromine rich electrolyte, the reduction reaction becomes bromine to bromide ion.

This reaction provides a long term invariancy in the system. The bromine rich electrolyte is supplied at the negative protective electrode surface, which is separated from the main electrolyte flow by a microporous barrier or ion selective membrane.

The protection electrodes in the terminal end manifolds which supply and remove electrolytes can most effectively be annular, with the main electrolyte flow through this annulus. The electrodes in the terminal end manifold which is dead ended in this region can be planar and perpendicular to the manifold cross section.

Ideally, the manifold protective electrodes should be located at the first and last manifold channel junctions. Location of the protective electrodes at regions removed from these ideal points requires that the input voltage be boosted over that of the stack voltage for ideal protection. The analysis of boost voltage is given in Appendix 5.

I.3.4 Tunnel Protection
Tunnel Interconnect Analysis

The power requirements for shunt current protection can be reduced by the use of tunnel interconnects between the channels and inserting and removing the protective current at the first and last channel/tunnel node (Figures I-13 and I-14). Current, t_o, entering the system at the first tunnel channel node can divide with part, j, going to the channel through resistance R_c, part t_1, going through the tunnel with resistance R_{T_1}, and part l_1, going to the cell through the channel leg with resistance R_L. If the resistance of R_{T_1}, (and subsequent tunnel resistances) are chosen and designed such that the voltage drop through R_{t_1}, is equal to the voltage difference of the cells whose channels are connected by the tunnel, there is no potential difference across R_{L_1} and R_{L_2} and thus no shunt currents. Thus:

$$V_o + IR_e = t_1 R_{T_1} = t_m R_{T_m} = t_{n/2}\, R_{T_{N/2}}$$

Under these conditions, the tunnel insert current divides only into two parts, current in the tunnels and current in the channels, and thus the manifold.

The formulas for computation of the resistance values are derived in detail in Appendix 5. The nomenclature is the same as defined above. Tunnel current for N cells in series (with $k_o = 0$) is:

$$t_o = t_{N/2} + k_{N/2} = J' \frac{\lambda'}{\lambda'-1} \left[\frac{(\lambda'^{N/2}-1)^2}{\lambda'^{N}-\lambda'} \right] + t_{N/2}$$

$$= (V_o + IR_e) \left[\frac{(\lambda^{N/2}-1)^2}{R_m(\lambda^N+1)} + \frac{1}{R_{T_{N/2}}} \right]$$

SERIES-CONNECTED CELLS WITH COMMON ELECTROLYTE MANIFOLD AND CHANNEL INTERCONNECTS

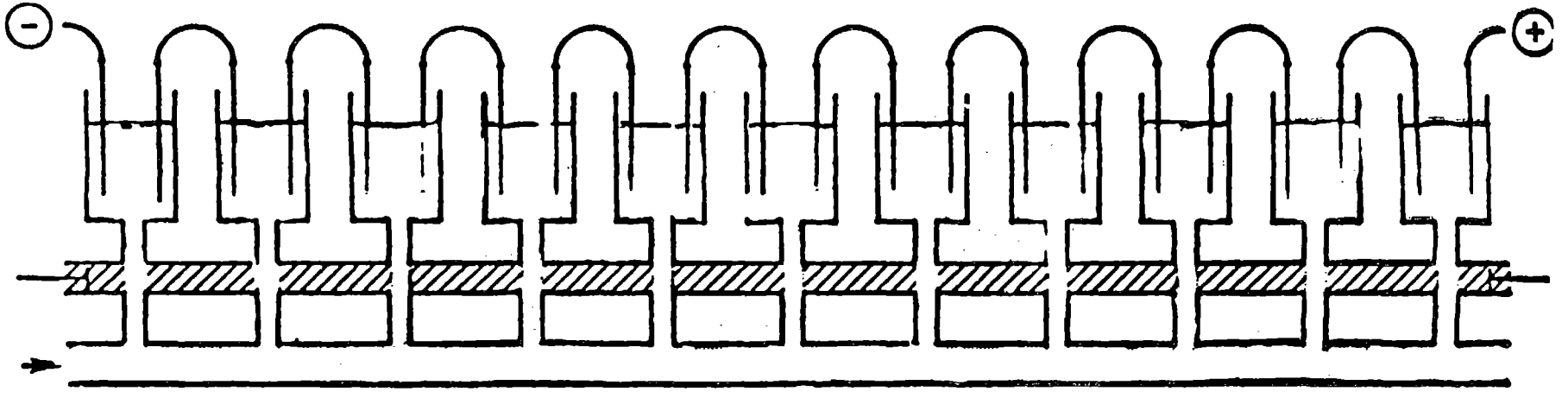

LUMPED RESISTIVE EQUIVALENT CIRCUITS

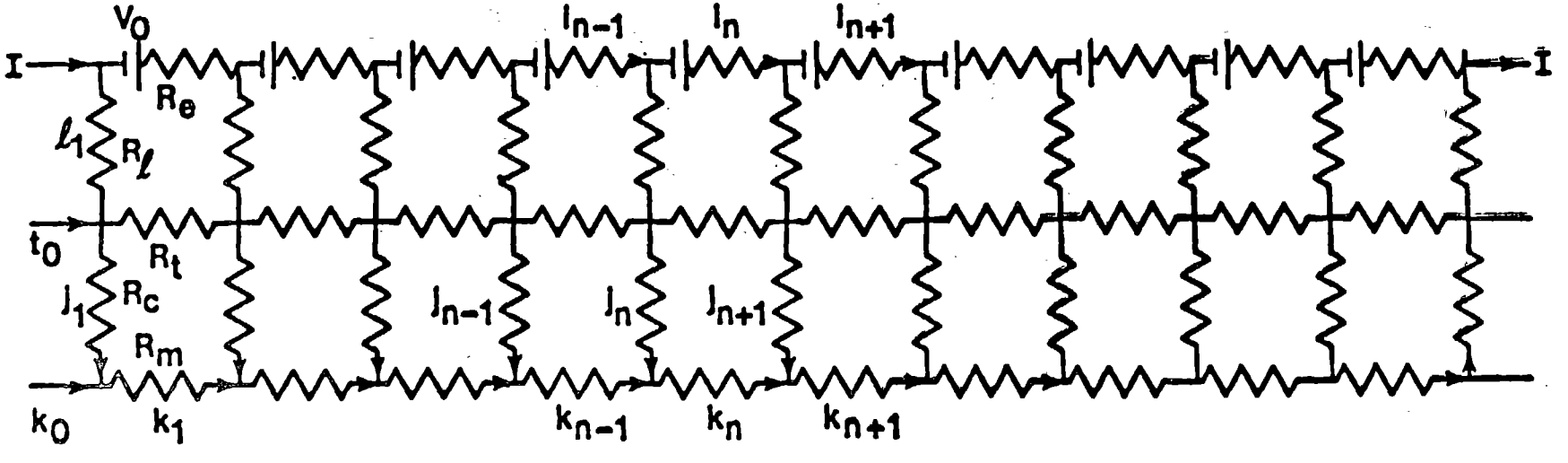

Figure I-13 Tunnel Protection Model

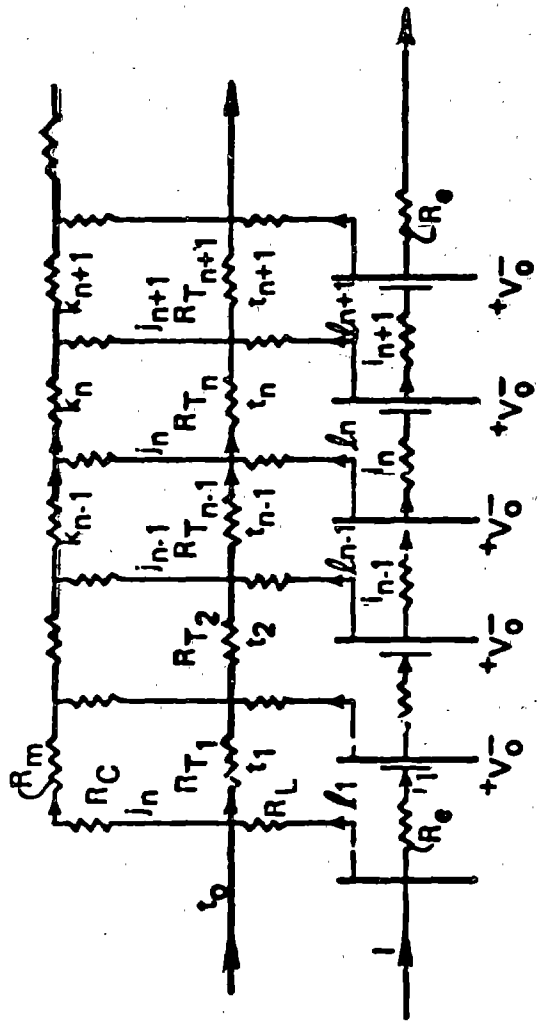

- $V_o + IR_e = t_n R_{T_n} = t_{n+1} R_{T_{n+1}}$
- $t_o = k_N \frac{N}{2} + t_N \frac{N}{2} = J' \frac{\lambda' \ (\lambda^2-1)^2}{\lambda^{N-1} \ \lambda^N . \lambda}$
- $J' = \frac{V_o + IR_e}{R_m + R_c \frac{\lambda'-1}{\lambda'} \frac{(\lambda'^{N-1} + \lambda')}{\lambda'^N . \lambda'}}$
- $l_n = 0 ; t_n R_{T_n} = V_o + IR_e$

$$\lambda' = \frac{\beta'}{2} \pm \sqrt{\left(\frac{\beta'}{2}\right)^2 - 1}$$

$$\beta' = 2 + \frac{R_m}{R_c}$$

Figure I-14 Tapered Tunnel Shunt Network

where $\lambda' = c/2 \pm \sqrt{(c/2)^2-1}$

with $c = 2 + R_m/R_e$

and $$J' = \frac{Vo + IR_e - k_oR_m}{R_m + R_c \dfrac{(\lambda' - 1)(\lambda'^{N-1} + \lambda')}{(\lambda'^N - \lambda')}}$$

The limiting condition of input tunnel current occurs when the center tunnel resistance $R_{T_{N/2}}$ is infinite. When $R_{T_{N/2}}$ is infinite the fraction $1/R_{T_{N/2}}$ is zero.

The value of the expression:

$$(\lambda^{N/2-1})^2/(\lambda^N+1)$$

is less than 1, particularly when λ and N are small.

The value for t_o is less than k_o whenever the following condition is met, namely:

$$R_m < R_{T_{N/2}}\left[1-(\lambda^{N/2-1})^2/(\lambda^N + 1)\right]$$

The value of the individual resistance of tunnels can be computed from the formula:

$$R_{T_N} = \frac{1}{\dfrac{\lambda'^{N-n} + \lambda'^n - \lambda'^{N/2}}{R_m(\lambda'^N + 1)} + \dfrac{1}{R_{T_{N/2}}}}$$

When $R_{T_{N/2}}$ is infinite, there is a decided "taper" to the values of the resistance of the tunnel. When the value of $R_{T_{N/2}}$ is finite, the "taper" is reduced. When the value of $R_{T_{N/2}}$ is sufficiently small, the tunnel resistances approach a constant value, i.e., $R_{T_{N/2}}$.

Protective Power For Tunnels

The protective power requirement for the tunnel case is the stack voltage minus one cell's voltage times the tunnel current:

$$\text{Tunnel Protective Power} = (N-1)(V_o + IR_e)^2\left[\frac{(\lambda^{N/2-1})^2}{(\lambda^N + 1)R_m} + \frac{1}{R_{T_{N/2}}}\right]$$

The manifold protection power is:

$$(N-1)(V_o+IR_e)^2/R_m$$

Thus, the tunnel protective power is less than the power for manifold protection in so much as:

$$\frac{1}{R_m} > \frac{(\lambda^{N/2}-1)^2}{R_m(\lambda^N + 1)} + \frac{1}{R_{T_{N/2}}}$$

In the limiting case, the tunnel protective power approaches that which would have been dissipated in the unprotected case.

Hydraulic/Electrolytic Decoupling

The use of tunnel protection allows a decoupling of design constraints on hydraulic and electrolytic systems. In the manifold protection case the protective current is determined by the resistance of the manifold. This, in turn, is governed by the desire to have the pressure drop controlled by channel resistance and not by manifold hydraulics.

Tunnel protection allows manifold resistance, and thus manifold diameter, to vary greatly without unduly influencing the tunnel protective current. This is shown in the following example. Consider two cell systems with the following parameters, namely:

V_o = 1.75 volts
I = 0
R_e = 0.03 ohms
R_c = 6000 ohms
R_m = 5 and 10 ohms
N = 52

The calculated protective currents for manifold and tunnel protection for these systems are:

R_m ohms	k_o amps	t_o amps	($t_{N/2}$ = 0)
5	0.35	0.0798	
10	0.175	0.0668	

Thus lowering the manifold resistance by a factor of 2, (increasing the diameter by 40%) the manifold protective power would increase by 100%. The tunnel protective power, however, would increase by only 19%.

The tunnel protective power is 23 to 38% of the power for either manifold case. Tunnel shunt current protection allows the battery system designer considerable freedom. The hydraulics and the electrical factors are effectively decoupled. Pumping and protection auxiliary power can be optimized at lower summation power requirements.

I.4 Design Concepts for Safety

Safety is always a concern in the design of a battery system. By definition, a secondary battery is a receiver of energy, a storer of energy and finally, a deliverer of energy. The energy is stored in the form of chemical reactants. They must be kept separated to prevent unwanted release of energy.

Bromine Complex Storage

The charged zinc-bromine battery stores the zinc within the cells and the bromine as a complex in the exterior catholyte reservoir. During stand-by conditions the battery reactants are thus physically separated. During discharge only a small fraction of the bromine capacity is circulated through the system and even a smaller fraction is within the actual battery cells. This approach prevents the spontaneous release of stored energy because of internal short circuits, electrode spacing changes, etc., which can occur in conventional batteries.

The battery design is shown in Figures 0-1 and 0-4. The bromine complex is stored within the aqueous catholyte reservoir. Separate internal compartments can also be used within this reservoir. The catholyte reservoir, in turn, can be nested within the anolyte reservoir. A puncture would have to penetrate three walls in this case to gain access to the stored bromine complex.

Bromine Complex

The bromine complex is an association of quaternary ammonium cation with bromine polyhalide:

$$Q^+ + Br(Br_2)_n^- \rightarrow QBr(Br_2)_n$$

Such complexes are described in detail in a recent paper by D. Eustace (10). They have low aqueous solubility and separate from the aqueous electrolyte as a second phase. The aqueous solubility of bromine is reduced an order of magnitude or more by this process (above equation). Correspondingly the vapor pressure of bromine is markedly reduced.

The vapor pressures of bromine over some quaternary ammonium bromine complexes at a stoichiometry of two bromines per quaternary amine (nominally 50% state-of-charge (SOC)) are shown in Figure I-15. N-methyl-n-ethyl morpholinium bromide (MEMBr) is the quaternary used in the majority of our past work. The bromine vapor pressure at ambient temperature over the MEMBr complex is 10 mm Hg. This compares to 200 mm Hg for bromine, a 95% reduction. These data were taken from a study of hazards in zinc-halogen batteries by Factory Mutual Incorporated, Norwood Massachusetts. The Factory Mutual research was supported by DOE Contracts EM-78-C-02-5088 and DE-AC02-79ET25110, and a series of EPRI contracts.

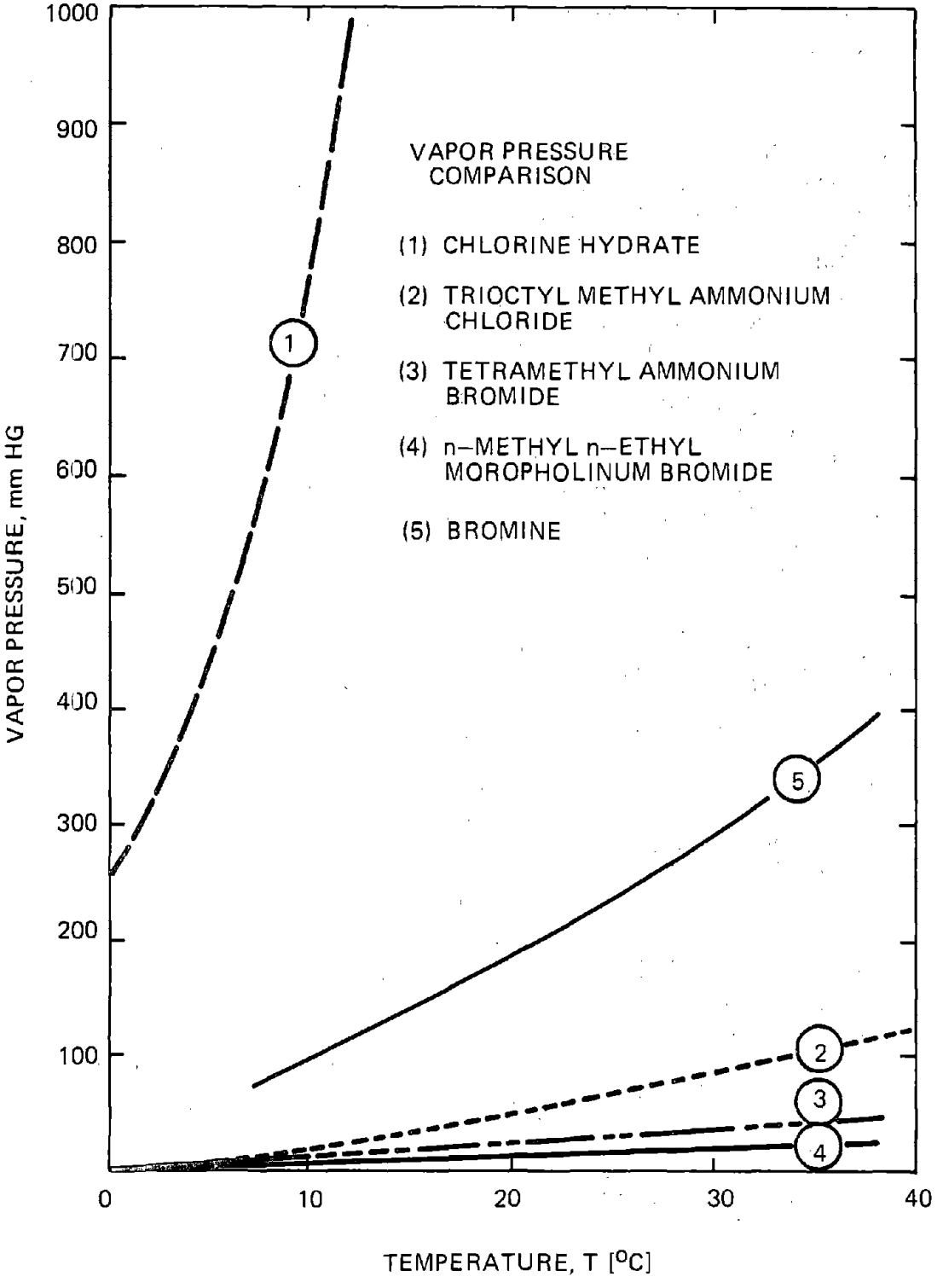

Figure I-15 Vapor Pressure of Bromine and Bromine Complexes

The low vapor pressure of the complex is not the whole story. As bromine vapor leaves the surface of the liquid bromine complex, the bromine to quaternary ratio is reduced. The lower this ratio, the lower the vapor pressure. The vaporization of bromine thus causes a quenching or extinquishing effect. A skin or "crust" of low bromine content material forms on the surface sealing the remainder. The bulk bromine complex is more dense, so the surface layer is only slowly renewed by diffusion. If the bromine depleted surface is punctured or mechanically broken, there is a release of bromine from the now higher bromine content area until a new "crust" is formed. The bromine complex is thus self sealing.

The vaporization of bromine requires the input of thermal energy. Normally, in the battery, the complex is at or slightly above ambient temperature. There is thus only a small thermal driving force from the surroundings for vaporization.

As part of the ongoing evaluation of bromine complexes, samples of representative mixtures of bromine and complexing agents were submitted to Hazards Research Corporation (HRC), Rockaway, New Jersey for hazards analysis. A report of their investigation (HRC4771) entitled, "Reactivity of Bromine Bromide Complex", and having to do with impact sensitivity, auto-ignition, deflagration, and flash point (TAG) studies was returned in December, 1980.

Hazards Research Corporation found that the material was basically unresponsive in all of these tests. Impact sensitivity results were analogous to that of water. Auto-ignition did not take place in 6 trials at heating to 500°C. No flash was observed to 125°C at which point the vapors from the complex extinguished the pilot flame. No propagation was observed in the deflagration tests, although the squib triggering did cause some thermal decomposition.

Hydrogen

Small amounts of hydrogen are produced in the battery system. The effect on battery capacity is correspondingly very small. It can be removed by recombination with bromine, (See Section IV.4). In the gas spaces within the battery system, there is little or no oxygen. Any oxygen in the gas space from the presence of air during assembly and filling will equilibrate with the electrolyte and be circulated into the cells. Here it will quickly react with freshly deposited zinc metal surfaces. The gas phase is thus rapidly reduced to nitrogen. The bromine vapor in the gas space is low because of bromine complexation (see above). The gas phase in the normal zinc-bromine battery system is thus nitrogen with small amounts of hydrogen and bromine. Homogenous gas phase reaction of dilute hydrogen and bromine is not favored, kinetically.

The normal zinc-bromine battery system is enclosed to prevent the escape of the small amount of bromine vapor present, since it would have to be replaced to provide for long term operation of the battery. Any puncture of the enclosure into a gas phase region could release some of the gas, which in a normal operating battery would consist of nitrogen with a little bromine vapor and the small amount of hydrogen which had not yet been recombined. Hydrogen is thus a comparatively minor safety problem.

I.5 Projected Development Plan

A technical development plan has been prepared for Exxon's Zn/Br_2 flowing electrolyte battery technology. Key technical goals and resources (people, equipment, and time) needed to accomplish these goals are specified. The plan serves as a guideline against which program progress is evaluated. This effort was internally funded by Exxon.

Figure I-16 shows the overall schedule projected for the Zn/Br_2 product development program which allows a 1990 commercialization. Commercialization is defined as the capability to produce 25,000-100,000 full scale 20 kWh batteries per year. The program consists of the following phases: (1) Advanced Engineering Development, (2) Prototype Development, and (3) Product Development. Phases 1 and 2 are to be carried out in parallel through 1981-1985, with pilot production capability (1,000 units/year) by 1987-88.

Figure I-16 Zinc-Bromine Battery Product Development Schedule

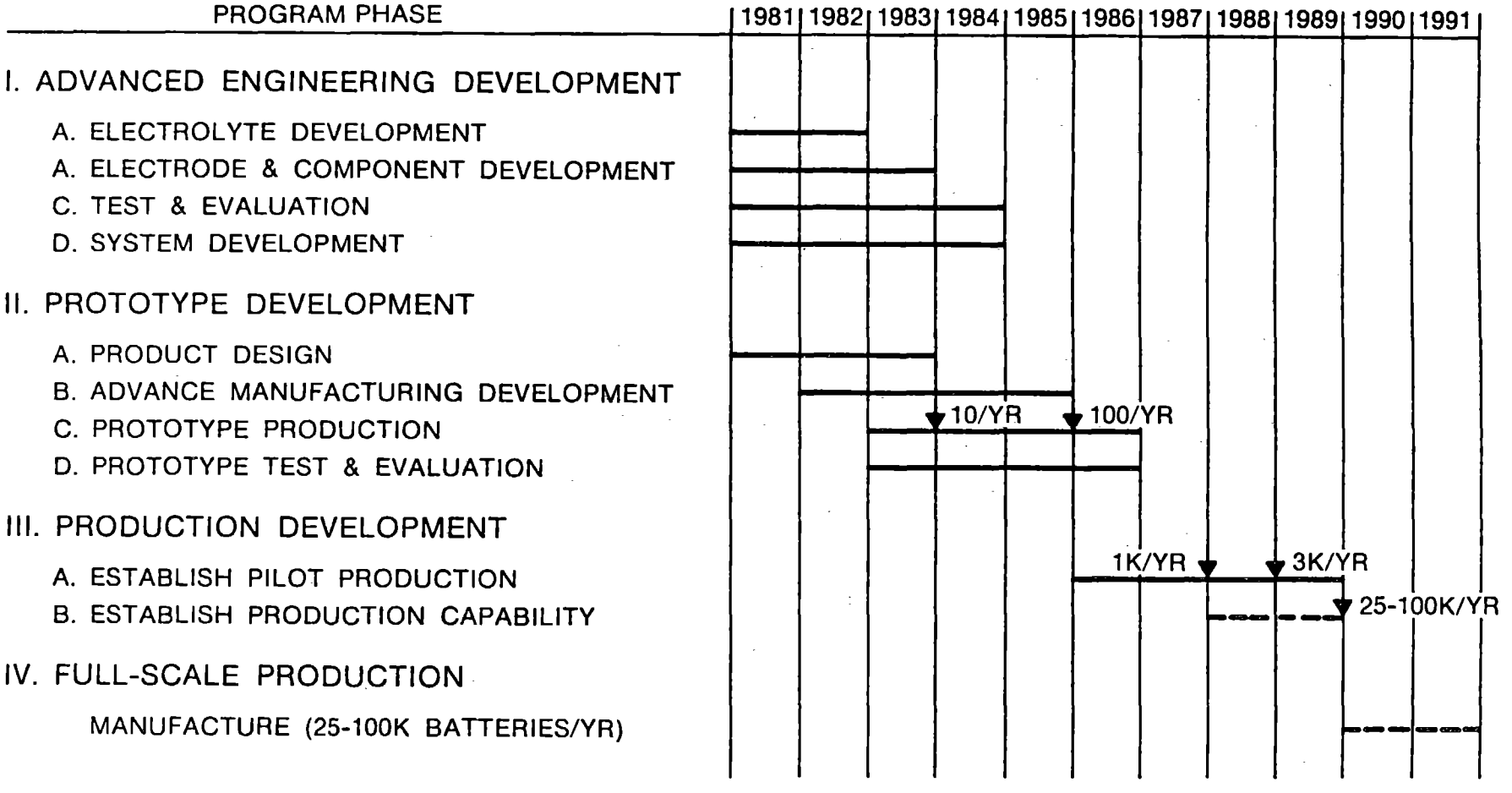

II. Manufacturing Development

Introduction

Unlike many battery systems where cells and small batteries can be developed and tested in glassware, the flowing Zn/Br_2 battery has required from its inception hardware and materials that were similar to the projected final product. Early in the project, Exxon made the philosophical decision to design components such that high volume production techniques could be directly applicable. This meant that when parts were not currently available commercially, a significant effort was made to develop extrusion, compression molding, and/or injection molding capabilities for making these parts. Especially with respect to the components associated with the battery stack, high and uniform tolerances around the periphery of the parts were needed to avoid leakage and to give uniform flow rates and distribution, from cell to cell, and within a given cell. Also, to maintain uniform flow, planar electrodes were required. While 100 cm^2 parts were being utilized, these criteria could all be sufficiently met with compression molded parts. However, with the scale-up to 600 cm^2 parts early in the Phase I contract, a new fabrication technique had to be developed - namely injection molding.

At the start of Phase I, the state-of-the-art unit cell incorporated in Battery X-3A, shown in Figure II-1, consisted of a bipolar electrode and two flow frames which were each compression molded with poor tolerances. An expensive ion-selective membrane and two polypropylene screens were used for separation and internal support. These parts, the cells, were all held together with internal stainless steel bolts, making assembly both tedious and time consuming.

The current "state-of-the-art" unit cell, found in the X-10 battery is shown in Figure II-2. The three individually compression molded electrode and two flow frames found in X-3A are now a one piece insert injection molded part of high tolerances. The ion-selective membrane has been replaced by an inexpensive, commercially available microporous (Daramic) separator. The two polypropylene spacers are present to match the half cell thickness to the polypropylene screen thickness. The assembly of battery stacks now utilizes external bolting which greatly speeds up the assembly process.

II.1 Carbon Plastic Processing

At the heart of the zinc-bromine battery being developed at Exxon is the carbon plastic electrode which is inexpensive, stable to the chemicals involved, and relatively easy to fabricate using commercially available processing techniques. The fabrication of carbon plastic begins with compounding in a Banbury mixer of highly conductive carbon and a polyolefin plastic. The quantities of each is determined such as to give a final product with a resistivity of less than 5 ohm-cm, when measured through the thickness of an extruded sheet. The choice of polyolefin is determined by the desire to have a rigid, non-brittle, extrudable product.

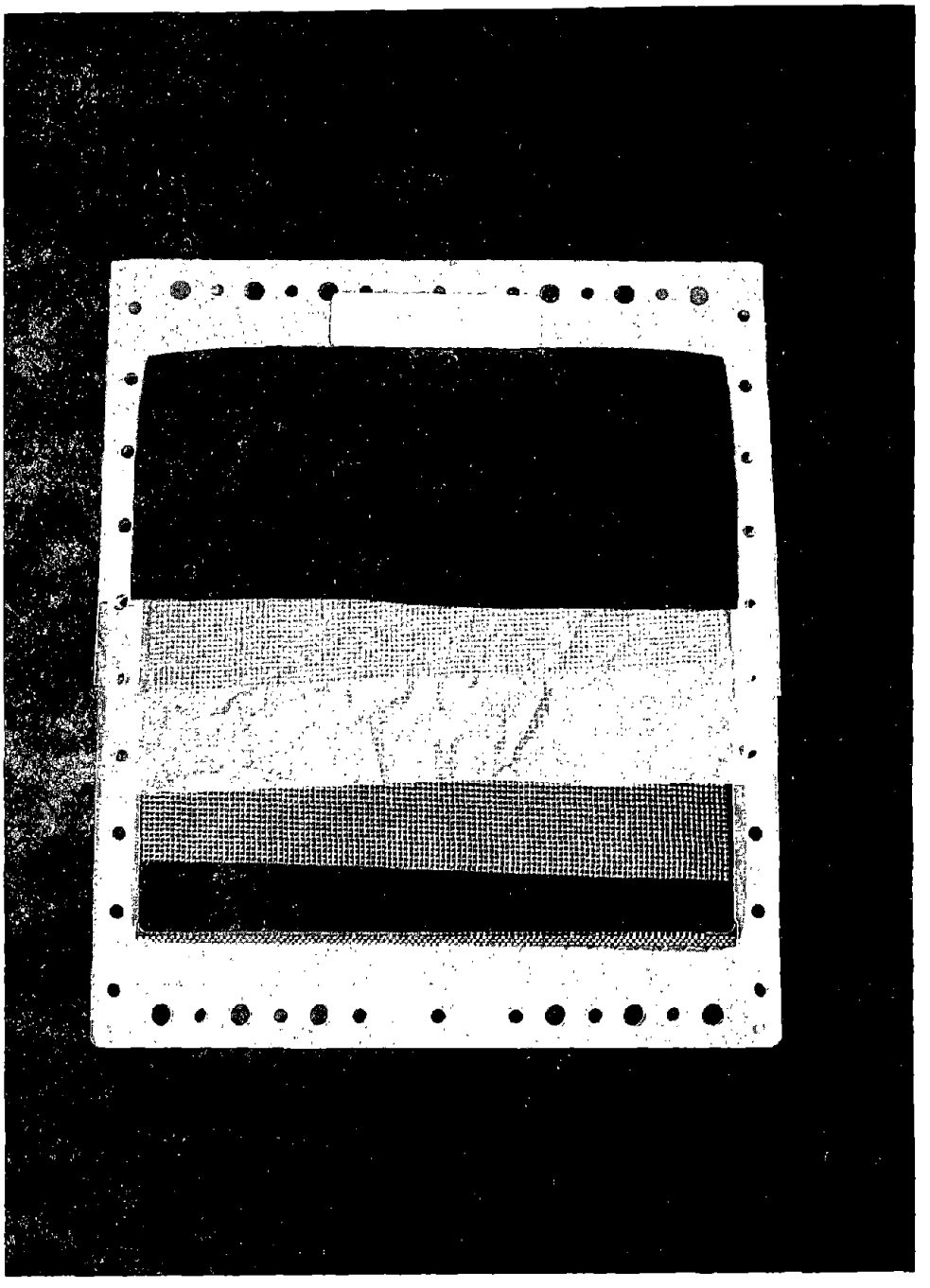

Figure II-1 X-3A Battery - Unit Cell

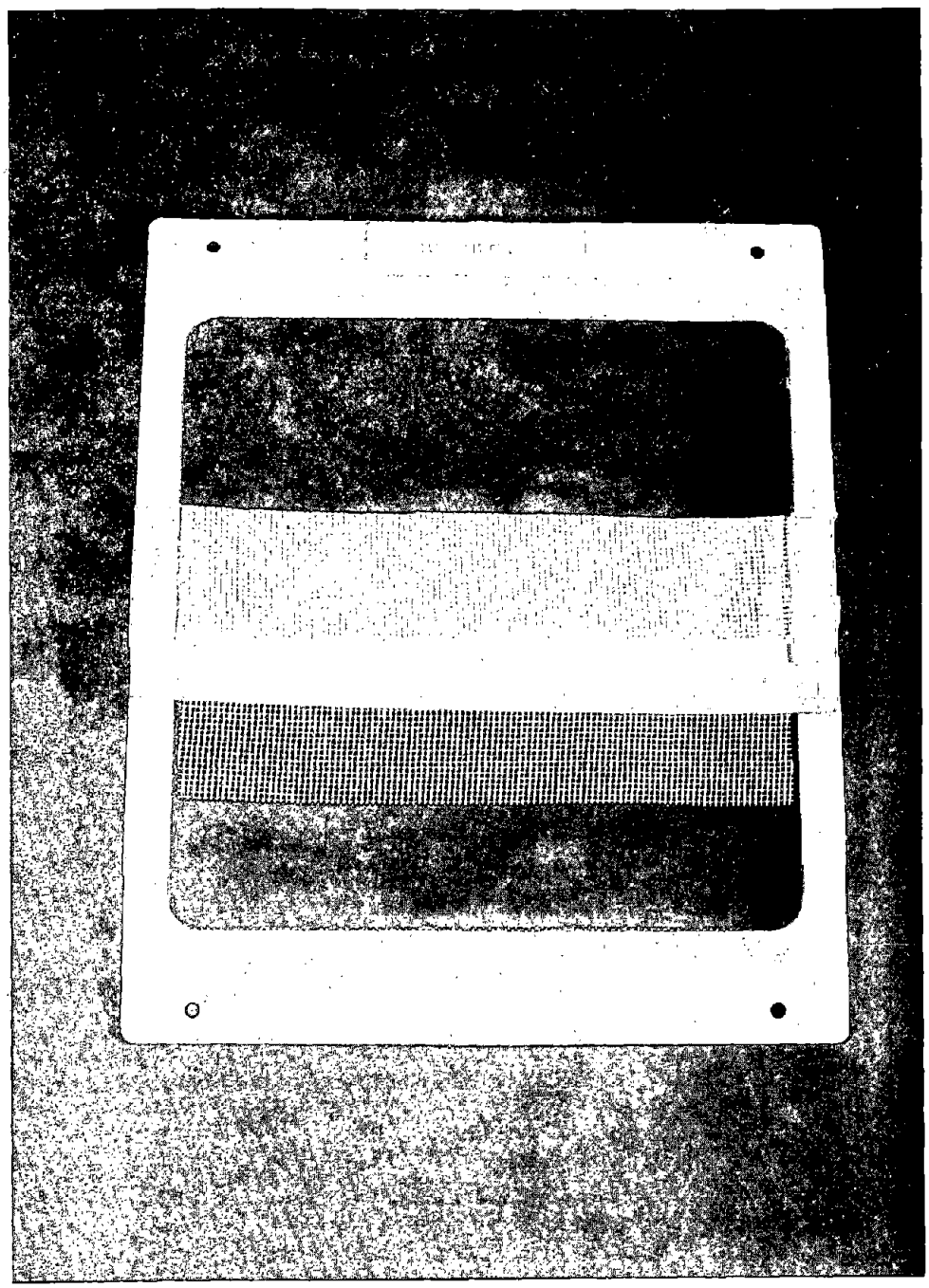

Figure II-2 X-10 Battery - Unit Cell

The compounding of the carbon and the plastic is relatively straightforward once the proper batch size has been determined. Care must be taken to avoid degrading the polyolefins by exposing them to excessive temperatures. When the compounding is complete the carbon plastic must be milled and diced suitably for extrusion, prior to its cooling, otherwise it becomes unworkable. Normal quality control at this point involves measuring resistivity on a press out, analyzing carbon loading and checking for uniform dispersal.

Extrusion of the diced pellets into a flat sheet, normally 10-30 mils in thickness, is the next operation. While this extrusion is fairly routine, the back-pressures involved in extruding the highly loaded carbon plastic can be very large. As a result, care must be practiced in selecting both machine and die. Normal procedure requires two passes through the extruder in order to obtain uniform carbon dispersion. The use of a spaghetti die with a chopper downstream, works well for the first pass. Quality control entails dimensional checks and conductivity measurements. Also life tests in bromine electrolyte as described in Section IV can be made, if desired.

II.2 Cathode "Catalytic" Layer

In order to avoid polarization problems at the cathode, it is necessary to provide a higher surface area than is attainable with extruded carbon plastic. Zinc plating and stripping shows very high exchange currents and almost no activation polarization is observed for the zinc on carbon plastic. Bromine electrochemistry on carbon shows more limited exchange currents. Br_2 can be oxidized and reduced directly on the carbon plastic. Large activation potentials are, however, required for both charge (~200-400 mV for Br_2 evolution) and discharge (~400-800 mV for Br_2 consumption). These polarizations could lead to very poor voltaic efficiency.

Surface area measurements of the carbon plastic bipolar using the BET method show limited surface roughness (50-100 cm^2/cm^2). Furthermore, much of this surface area may be electrochemically inactive because of tortuous conductive and diffusive pathways. Application of higher surface area carbons to the bipolar carbon plastic increases the apparent roughness of the surface, effectively catalyzing the surface for electrochemical reactions. After the proper application of high surface carbons, carbon plastic electrodes show virtually reversible bromine electrochemistry. Battery performance with the properly activated cathode catalytic layers show high voltaic efficiencies where the only significant voltaic polarization is from internal resistance.

II.3 Insert Injection Molding

The ability of the project to remain on schedule and the steady improvement in battery quality is due, in large part, to our successful injection molding efforts. Prior to the availability of parts by this process, it was necessary to compression mold two flow frames and a

bipolar electrode for each cell. These parts had variations in thickness, ± 4 mils each, such that leakage in batteries was a constant problem. The compression molding operation was also slow enough that the project was frequently parts limited.

With the insert-injection molded electrodes, the three compression molded parts have been combined into one piece. Thickness tolerances are within ± 1 mil around the periphery of the part, and electrolyte leakage in batteries has diminished to the extent that the number of required tie rod bolts has been reduced. Also the significant reduction in labor per unit cell has allowed us to fabricate additional batteries and work on other problems.

The molding operation is performed under contract by an outside "job" shop on a 350 ton Ingersoll Rand machine. During initial testing a variety of filled and unfilled plastics were examined. A filled polypropylene was selected finally, as its mold shrinkage characteristics gave minimal part warpage. Also, during these initial trials, the runners and gates were both enlarged and relocated to yield the part shown in Figure II-3. This was needed to provide adequate fill, especially in the flow distribution areas. The "dog-ears" visible along either side of the electrode were added to increase the strength of the parting line.

The actual molding operation entails having the operator carefully align the pre-cut carbon plastic insert with its hot pressed "catalytic" layer. This alignment is aided by a locating device which mounts on pins in the mold. The insert is then held in place with vacuum and the plastic framing material is injected around it. The entire process, including cutting off the runners, requires just under 2 minutes. The molder feels that this number can be improved on by automating the alignment and by using multiple cavity molds.

For quality control, parts from the injection molder are checked for tolerances and for the soundness of the insert to frame bond. Seven electrodes from any given molding run are also made into an eight cell parametric battery and tested for such things as polarizations and uniformity of zinc plating.

II.4 Separator

During this contract, the battery separator of choice has shifted from ion selective membranes, originally P-1010 made by RAI Inc., to microporous membranes, such as Daramic made by W. R. Grace Co. Daramic is a low cost, durable, commercially available, microporous membrane. It is a filled polyolefin which is processed into its final geometry by conventional extrusion techniques. Table II-1 compares P1010 and Daramic.

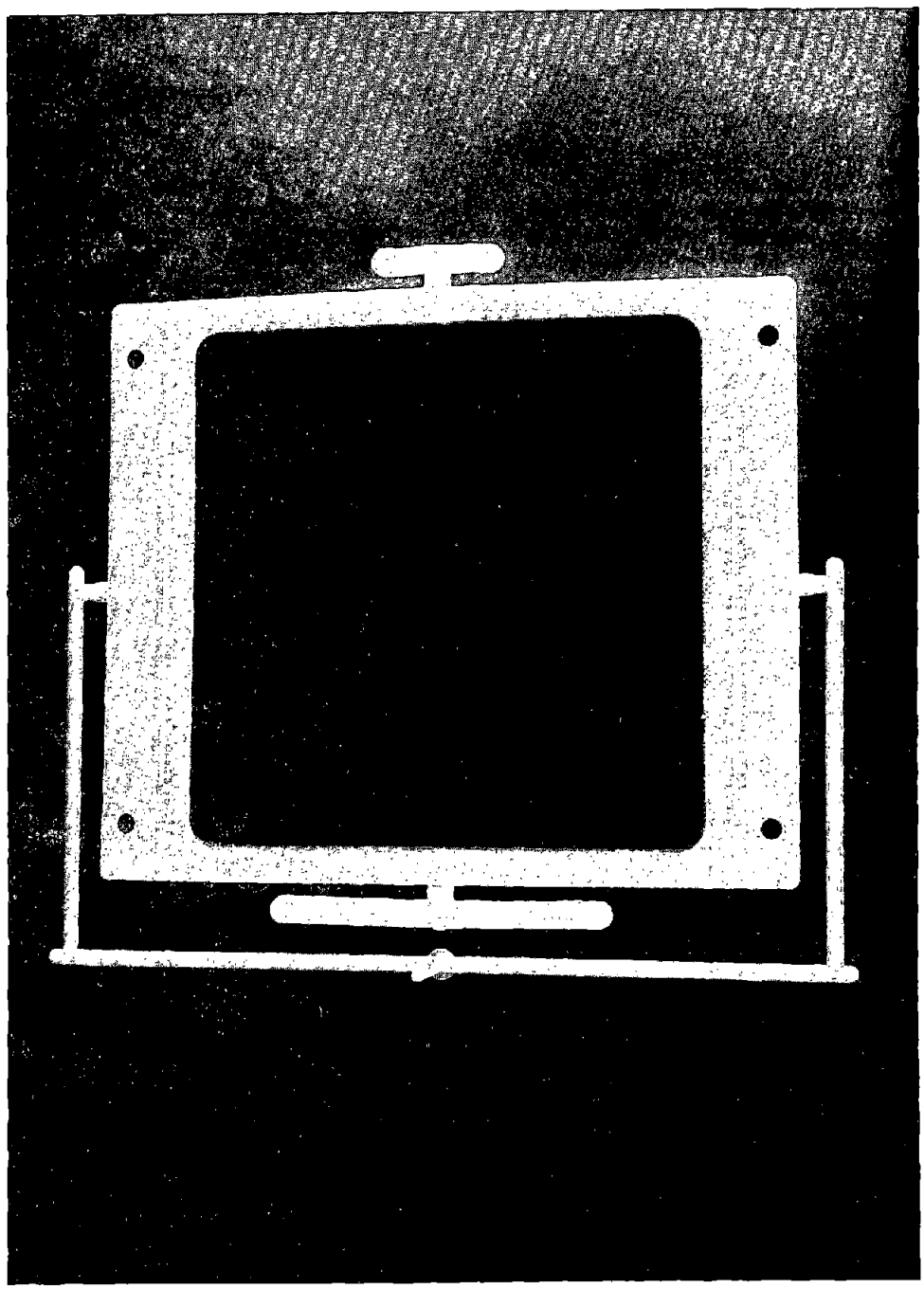

Figure II-3 Injection Molded Electrode

Table II-1

P1010 vs. Daramic

	P1010	Daramic
Type	Ion-Selective	Microporous
Typical battery coulombic efficiency	85-90%	80% with additives
Typical battery voltaic efficiency	85%	85%
$/sq. ft.	2-5	.0.10-0.12
Ease of handling	Difficult (Must be kept wet)	Easy (Dry)
Commercial availability	Limited Capacity	Yes

As can be seen the switch to Daramic has resulted in significantly lower cost. It is much easier to handle in processing as it is not prone to tearing or puncturing. The Daramic does have to be washed free of an oil residue resulting from its extrusion. This is done with multiple acetone washings.

There are some penalties experienced in the material switch. The battery stack thickness has been increased about 22 mils/cell. The coulombic efficiencies have decreased slightly due to the greater transport of Br_2 across the separator (Section IV gives details). The slight loss in voltaic efficiency is due to the increased cell resistance caused by the wider intercellular spacings.

An additional advantage to the extrudable Daramic material is that virtually any profile desired can be manufactured. This feature is used to advantage by having a series of posts profiled on each surface (See Figure II-4). These posts, which line up with each other from side to side, provide both structural strength and intercellular spacing. With the addition of the posts, it is no longer necessary to use polypropylene screens which mask a greater electrode surface area (15-20%), are difficult to assemble in the stack, and tend to entrap any gas bubbles which may be present.

II.5 Two Piece Unit Cell

In order to continue the simplification of the zinc-bromine battery unit cell several projects are underway. The goal of these projects is a unit cell that is simple to manufacture. To attain this goal we envision a unit cell consisting of a framed bipolar electrode, and an insert injection molded microporous separator which contains molded-on posts for half cell spacing and support. These two parts are illustrated in Figure II-5.

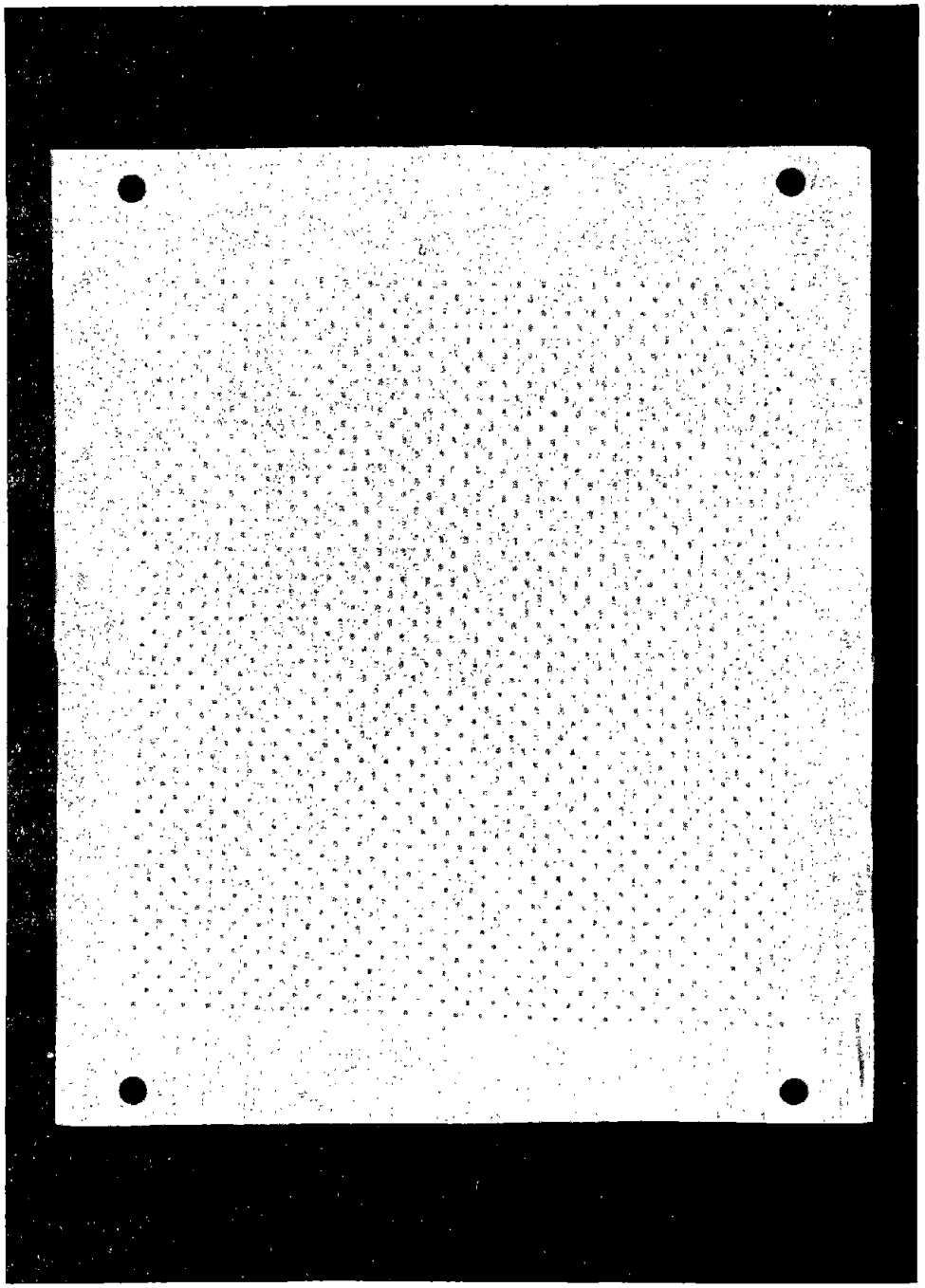

Figure II-4 DARAMIC Separator

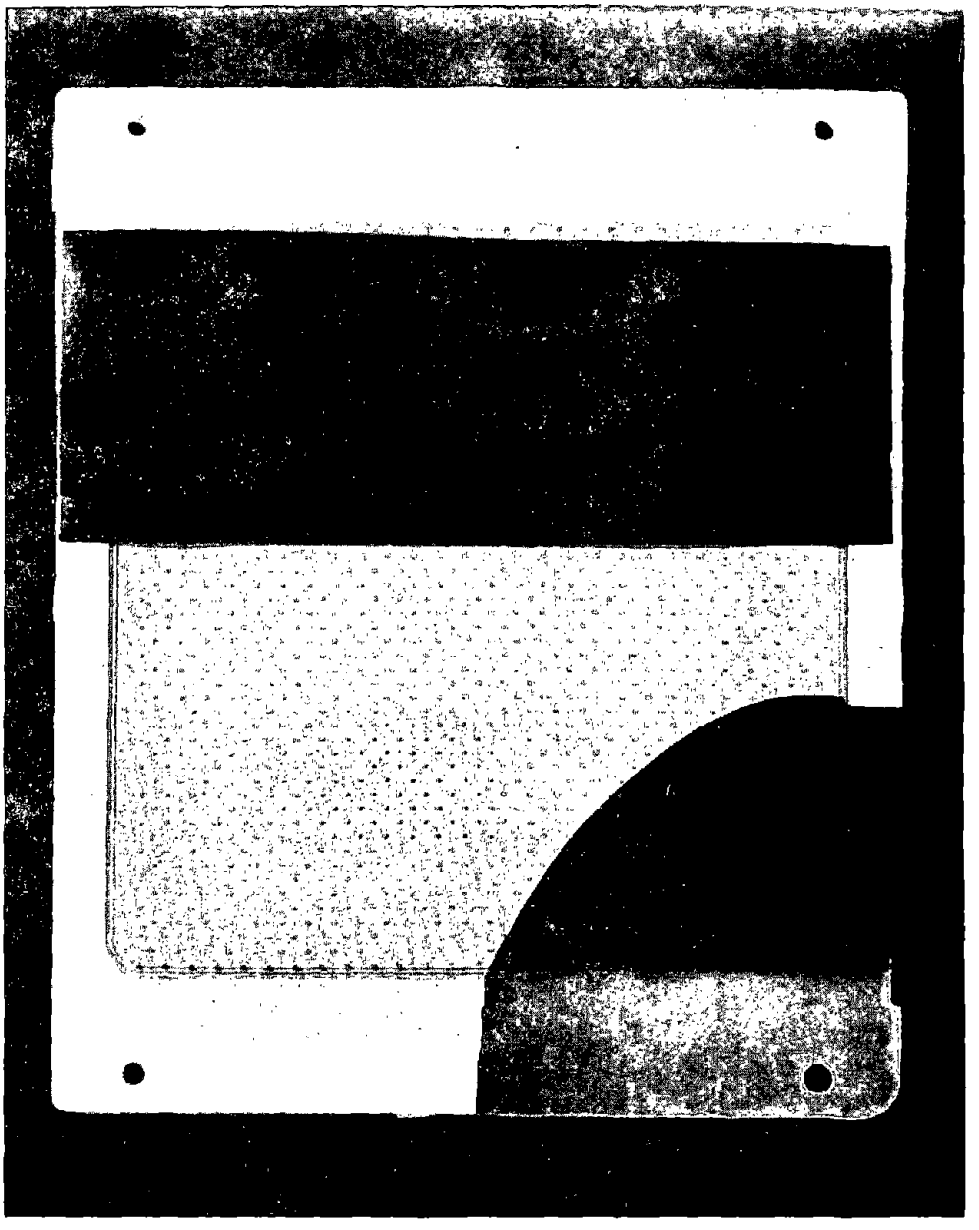

Figure II-5 Envisioned Electrode/Separator with Molded Posts

The framed bipolar electrode will be a co-extrusion of carbon plastic and non-conductive polyolefin on each side as illustrated in Figure II-5. A die for this extrusion has been constructed and preliminary tests are encouraging. The first full test is scheduled during Phase II of this project. The "catalytic" layer will be applied onto one side of the carbon plastic. The only other operation is that of punching out the final part.

The insert injection molded microporous separator will be fabricated in a manner strictly analogous to the currently injection molded electrodes. The support posts on the separator are formed when that material is extruded. Preliminary results show that framing of the separator rather than the carbon plastic electrode will have several advantages. The insert to frame seals will be stronger. The flow distribution part of the frame will be facing away from the microporous membrane helping to minimize crossflow. The microporous membrane will no longer extend to the edge of the battery module where leakage is possible.

With the development of these two components, a co-extruded bipolar electrode and an insert injection molded separator, manufacturing of the battery module is reduced to operations already well developed within the plastics industry. The actual assembly is conceptually two stack feeders which alternately feed each of these components into a properly aligned stack. This stack can be held together by a combination of heat sealed edges and straps and/or tie rod bolts to maintain compression.

III. Assembly and Testing of Large Batteries

III.1 3 kWh (X-3) Submodules

Several 3 kWh (X-3) submodules were assembled and tested prior to fabrication, assembly and testing of battery X-10. The X-3 battery modules were 52-cell, bipolar stacks. Capacity rating of 3.25 kWh was based on 90 mAh/cm^2 zinc loading, 80% coulombic efficiency, and an average discharge voltage of 1.50 V per cell.

III.1.1 Components

Each X-3 module was comprised of 51 bipolar electrodes and two (2) current collectors, one positive and one negative, located at opposite ends of the stack. The current collectors provided the means for external electrical control. Active electrode area was 600 cm^2. In addition, there were 52 separators, 104 flow frames (a later design with injection molded electrodes eliminated separate flow frames), and 104 spacers in each 52-cell module. Thus, the average unit cell consisted of one bipolar electrode, one separator, two flow frames and two spacers. Vexar, an extruded polyolefin mesh made by Dupont, was used as the spacer to provide the required gap between the electrode surface and separator material. These components are shown in Figure III-1A.

The electrode stack was constrained by two (2) 1 in. thick polypropylene feed blocks which served as an entry and exit for circulating electrolyte through the battery module. The assembly was clamped filter press style with aluminum end plates, making it leak tight. Such a battery assembly is shown in Figure III-1B.

The first of these battery modules, X-3A, was assembled with compression molded electrodes and P-1010, a 0.001 in. cation permeable separator material made by RAI Inc. Battery module X-3B was identical to X-3A, except that the Br_2 reducing shunt current protective electrodes were of an improved design, and the primary objective here was to test the effectiveness of the new electrode design (This will be discussed in the next section).

Module X-3C, also a 52-cell bipolar battery was assembled with compression molded electrodes and Daramic separators, a 0.024 in. thick microporous material made by W. R. Grace for the lead-acid industry. This separator material had been successfully pretested in a smaller, 12 V battery. The objective of X-3C was to verify performance with Daramic on a larger scale before freezing the X-10 design.

III.1.2 Special Design Considerations

Earlier development testing had been done at the 12 V (8-cell) bipolar battery level, and in scaling up from 8 cells to 52 cells, a number of factors had to be considered. The X-3 test station represented a 6 1/2 fold increase in size. Accordingly, electrolyte volume, pumping

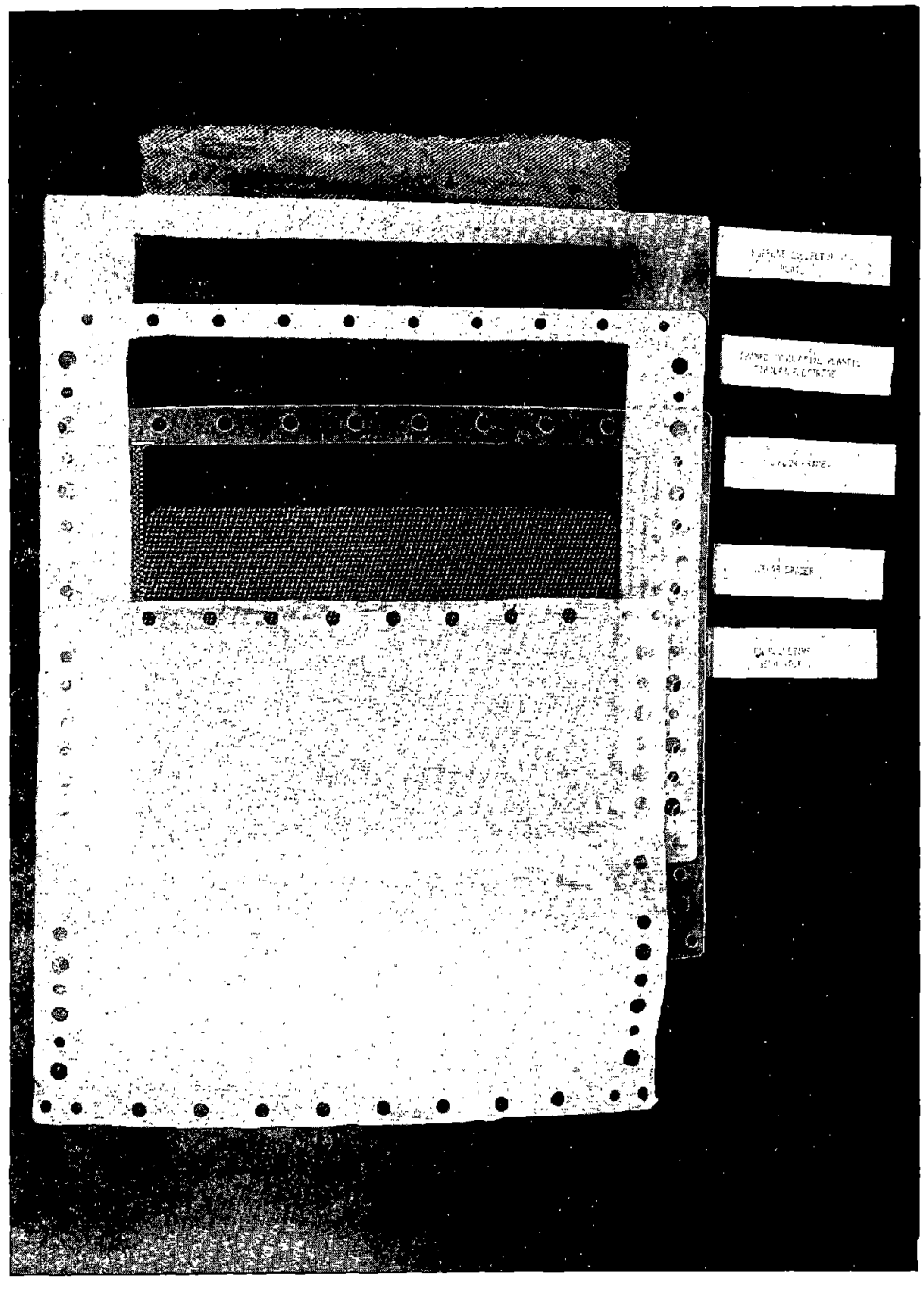

Figure III-1A Battery Module X-3A Components

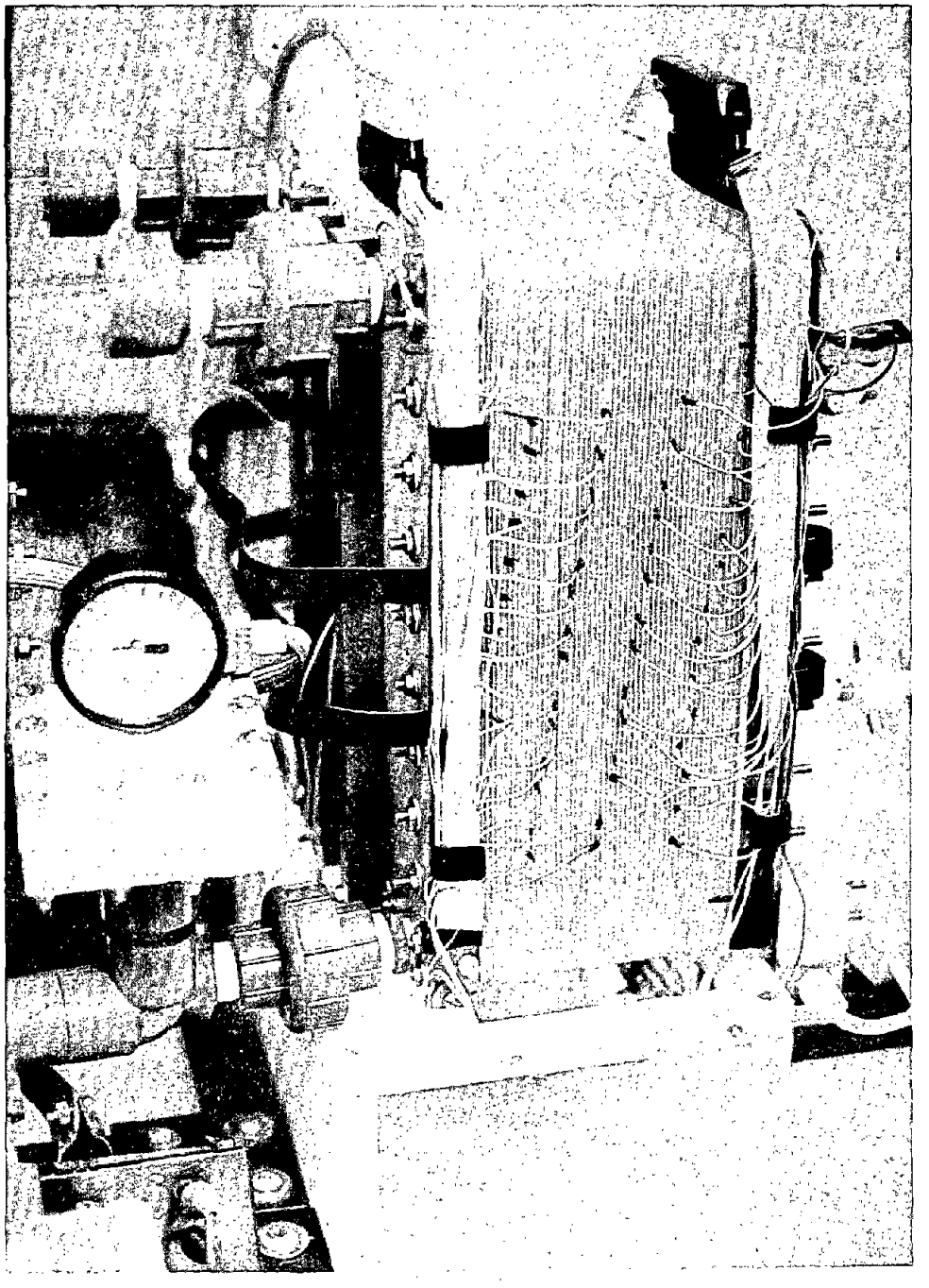

Figure III-1B Battery Module X-3A

rates, and electrolyte feed lines were increased proportionately over the values used for the 12 V systems. For example, electrolyte volume was increased from 4 l to 26 l, pumping rate was increased from 1.2 l/min to 7.8 l/min and the internal feed lines were increased to 3/4 in. I.D. The layout of the component parts was such as to make them readily accessible.

The most significant factor in scaling up from 12 V (8 cells) to 80 V (52 cells) was the added requirement of shunt current protection for the higher voltage battery. As discussed in Section I.3, multicell batteries with one or more common electrolyte manifolds, give rise to shunt currents with undesirable effects. In our 12 V system, the magnitude of these shunt currents was such as to permit operation during the course of an 8 hour day without deleterious effects. (A fully charged 12 V battery left on open circuit for 14 hours develops shunt current driven zinc growths in the manifold which affect battery voltage). However, with the higher voltage battery, operation could not be undertaken without shunt current protection. In our scheme, this was accomplished by imposing a nulling voltage signal in the manifold. This gave rise to oxidation on the bromine electrode side of the manifold and to reduction at the other end. The oxidation reaction was satisfied by allowing Br^- to form Br_2, with the Br^- being supplied by the electrolyte. To satisfy the reduction reaction, and avoid zinc deposition, Br_2 was supplied and Br^- was formed as part of the system. Supplying Br_2 to the protective electrodes on the zinc side of the battery was a demanding task. In module X-3A, this was accomplished by mounting the protective electrodes externally on the zinc electrode feed block. While this approach was effective (as evidenced by the 100+ cycles that were run), the protective power requirement was high due to the added 20-30 V drop in the external electrodes. This approach was modified in module X-3B where the protective electrodes were redesigned so as to be located inside the feed block. This design modification placed the protective electrodes in closer proximity to the battery anode, greatly reducing the protective power requirements. The success of this approach was demonstrated by testing X-3B for 29 deep charge-discharge cycles.

Module X-3C was identical to X-3B in construction except for the separator material used. Here the ion selective membrane was replaced with the microporous separator material. Several charge-discharge cycles indicated performance comparable to that observed on the 12 V units, where the microporous material had been extensively evaluated.

III.1.3 Cycling Regime

Battery performance evaluation consisted primarily of a repetitive charge-discharge cycling routine. Charging was done at rates of 5.8A to 11.6A (10-20 mA/cm^2) for a sufficient time to obtain a desired Ah input. Discharging was done at rates up to 17.4A (30 mA/cm^2),

usually to a 1.0V/cell cutoff. Higher discharge rates were also used. However, these were of shorter duration - a few minutes at most. The higher discharge rates were used to test the battery system's high rate capability, to generate polarization and power data, and to pulse the battery to simulate peak power demand. The following section presents the performance characteristics of the X-3 modules.

III.1.4 Performance Characteristics

Figure III-2 is a voltage plot of a charge-discharge cycle, in which the battery was charged at 11.6A for 4 hours (80 mAh/cm^2 Zn loading) and discharged at a constant load at approximately the same rate. Capacity input was 4.6 kWh with a material utilization of 71.5% based on the total amount of $ZnBr_2$ in the system. Coulombic efficiency was 77% with a 65% energy efficiency.

Figure III-3 shows a polarization curve for module X-3A at discharge rates that ranged between 17.4A (30 mA/cm^2) and 53A (91 mA/cm^2). The slope of the line is 0.42 ohms, and the linearity of the data suggests that the voltage loss was predominantly ohmic. Evidently, our pumping rate (25 ml/min-cm^2) will sustain these high currents for short periods (20-30 sec). Longer duration high current pulses may be expected to produce polarization losses, unless the pumping rate is increased. Figure III-3 also shows the corresponding power output. At the maximum current drawn, power output was 3.6 kW, somewhat higher than the 1 hour discharge rate.

The high rate pulse discharge capability of the battery over its useful capacity range was also tested. Here, high current pulses (46.6A avg.) of 15.20 seconds duration were superimposed at 3-4 minute intervals while the battery was discharging at 17.4A. These results are shown in Figure III-4, where the average battery voltage during the high current drain was plotted as a function of state-of-charge (zero % S.O.C. represents battery capacity exhaustion). These tests indicated that the battery delivered an average power pulse of 3.32 kW (11W/cm^2) at a current density of 80.3 mA/cm^2.

Figure III-5 summarizes the cycle life data of module X-3A. Here coulombic efficiency was plotted as a function of cycle number. Coulombic efficiency was used as a figure of merit because voltaic efficiency remained relatively constant. For the 100 cycles, the average energy efficiency was 70% (83% coulombic and 85% voltaic efficiency).

The plot shows a gradual loss in coulombic efficiency on cycling. This is believed to be due to loss in membrane selectivity with time. Similar data with a microporous separator showed that coulombic efficiency remained constant on cycling, as will be shown later (see Section IV.1.2).

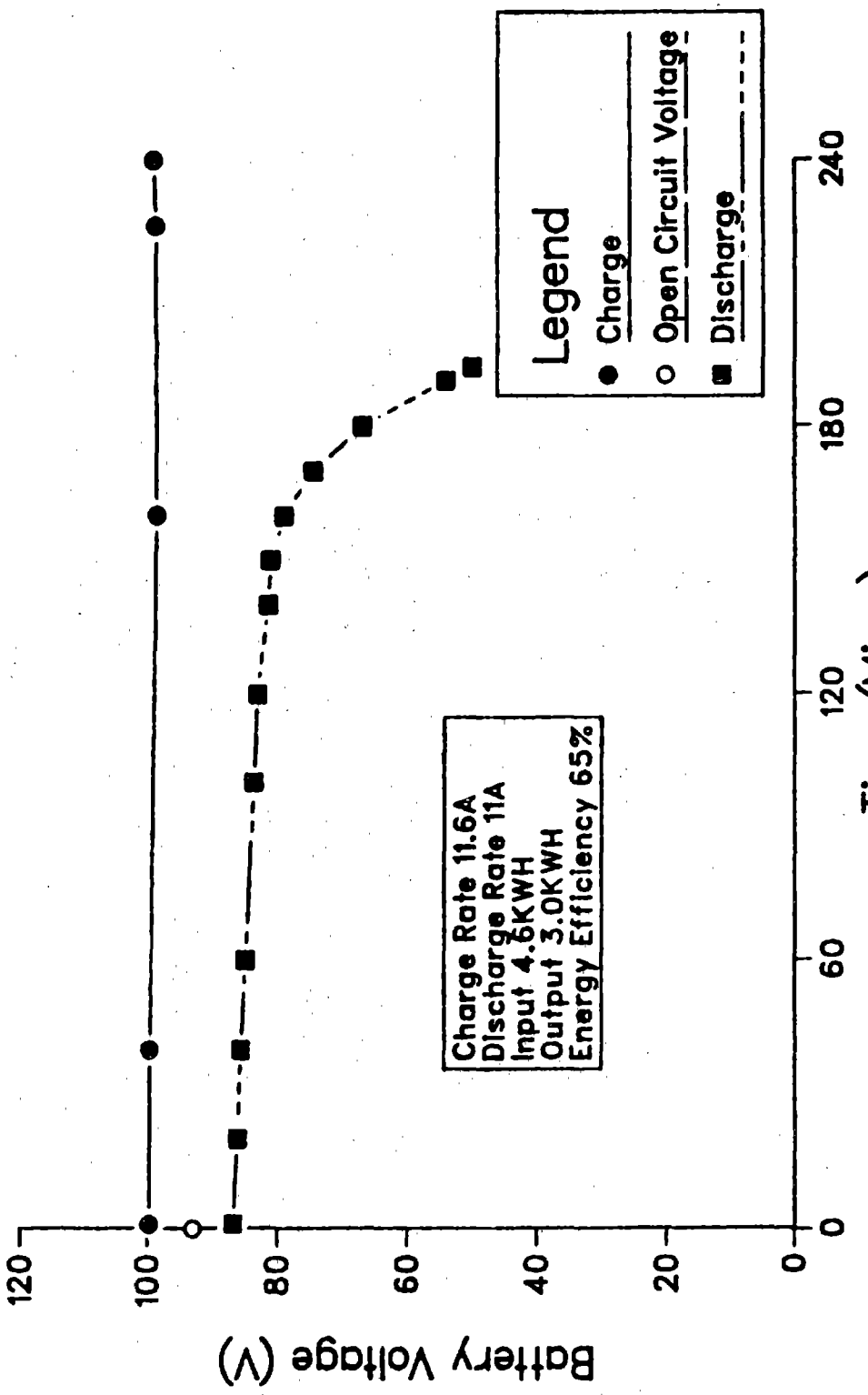

Figure III-2. Battery X-3D, Voltage vs Time Cycle #8

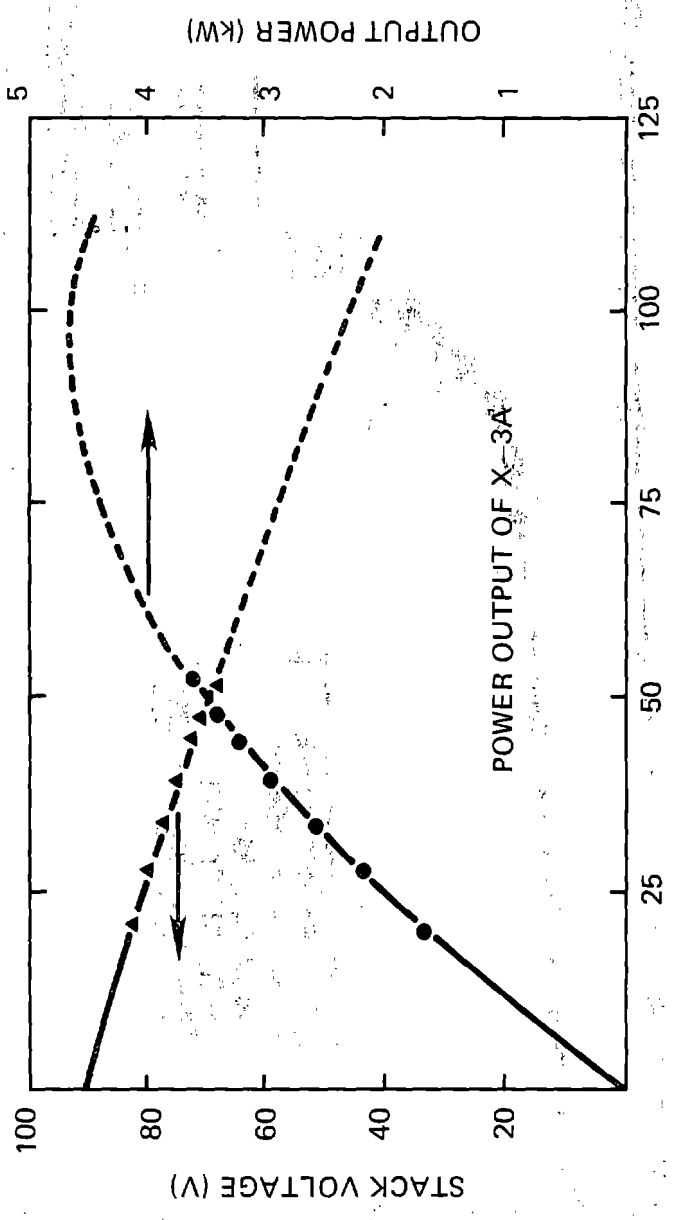

Figure III-3 Polarization and Power Curves, Battery Module X-3A

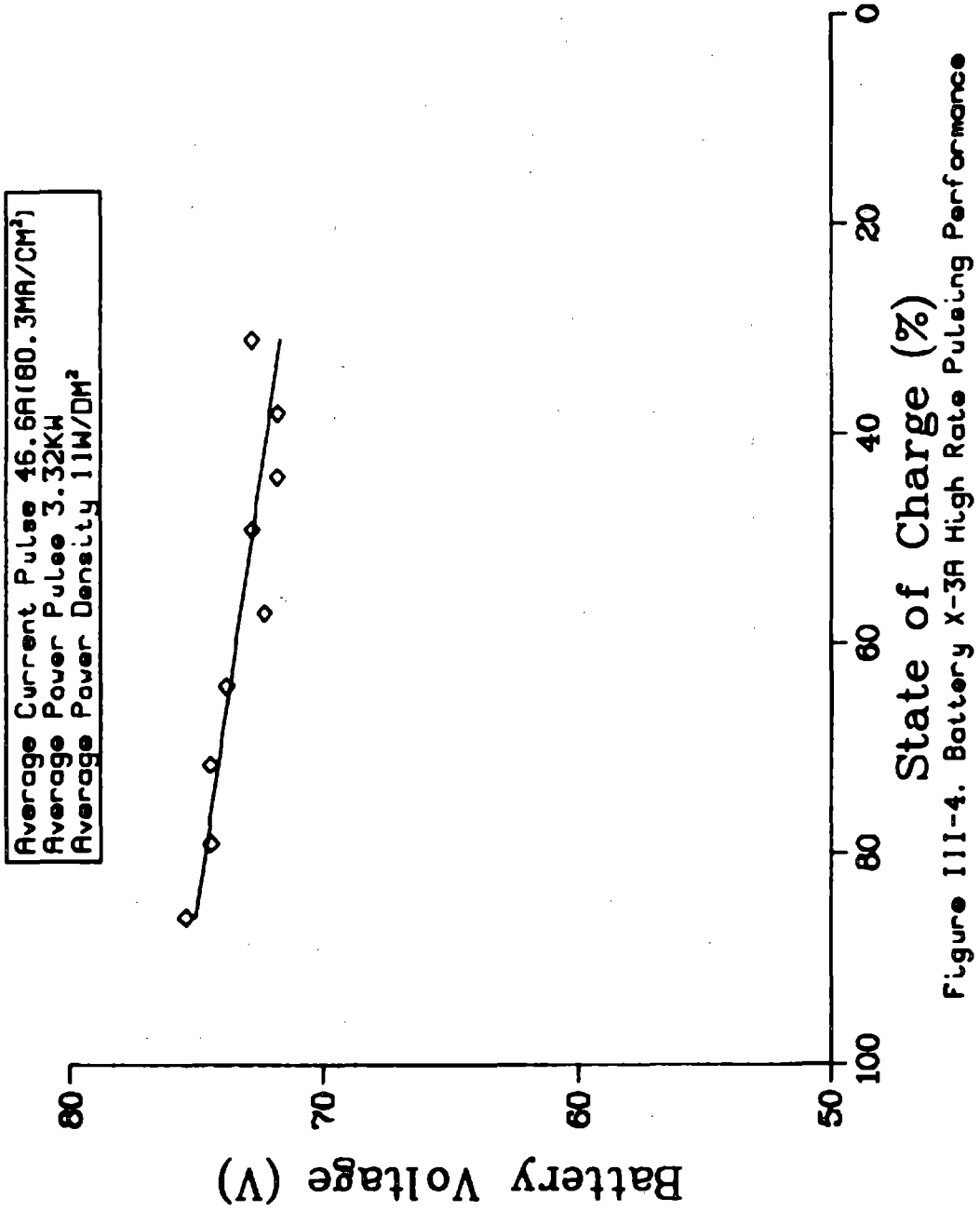

Figure III-4. Battery X-3A High Rate Pulsing Performance

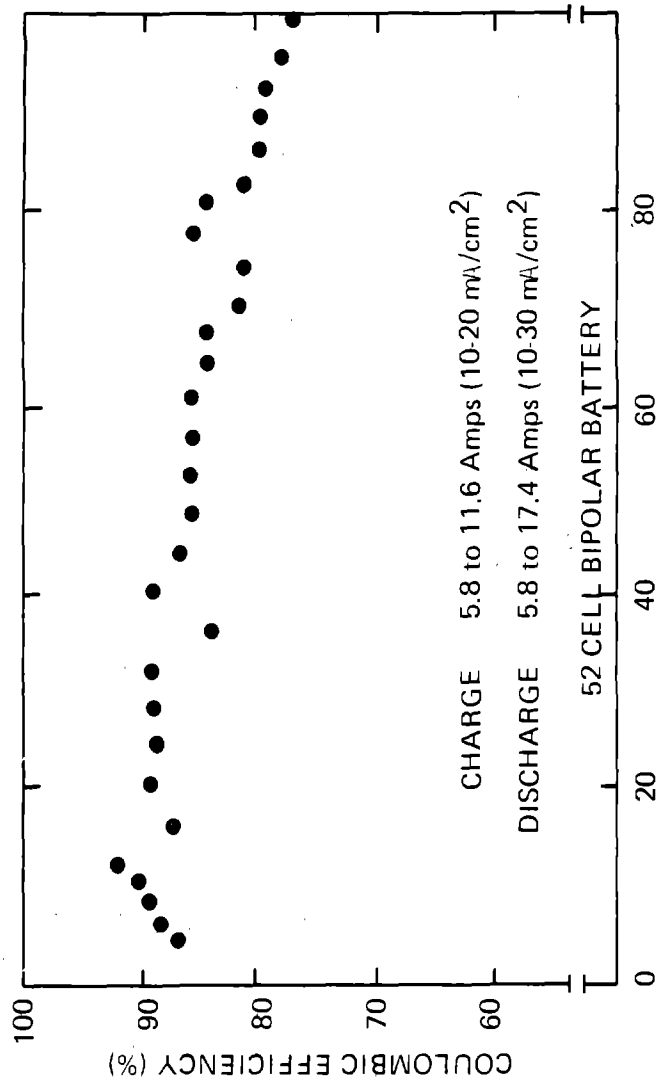

Figure III-5 Battery Performance vs Cycle Number, 52-Cell Bipolar Battery

As indicated earlier, module X-3B was assembled with more energy-efficient shunt current protective ("internal") electrodes, and a primary objective here was to test their effectiveness. The test regime included 29 charge-discharge cycles at rates that ranged between 5.8A-11.6A, and zinc loadings of 50-82 mAh/cm^2.

These tests led to the following observations, namely:

1. The "internal" protective electrodes showed good, stable and reproducible performance on battery cycling. Their effectiveness was also successfully demonstrated on a charged overnight stand. The overnight capacity loss indicated a 0.5 mA/cm^2 self-discharge rate in the fully charged state under the prevailing experimental conditions.

2. Coulombic efficiency (80-81%) was lower than that observed for module X-3A (86-88%) due to electrolyte cross-flow. On disassembly, 19 of the 52 P-1010 separators were found to leak to varying degrees under a 6 psi pressure differential. This problem developed, most probably, during assembly and is believed to be due to a mismatch between the Vexar spacer and flow frame dimensions. Since the compression molded electrodes with the separate flow frames were subsequently replaced by injection molded electrodes, with the flow channels being an integral part of the electrode frame, this problem has been eliminated.

III.2 X-10 Battery System

The X-10 test unit was an 80V (52-Cell), 10 kWh bipolar battery system. Its capacity rating was based on the same criteria used to rate the X-3 modules, as described above. In fact, X-10 consisted of three (3) X-3 modules connected in parallel electrically, as well as hydraulically. The test objectives were to demonstrate the zinc-bromine system on an increasingly larger scale, to look for scale-sensitive operating parameters, and to look for potential problems which might be associated with operating large, individual batteries in parallel.

III.2.1 Components

The components used in assembling X-10 were identical to those used in the assembly of X-3 modules, excepting the bipolar electrodes. X-3 modules were assembled with compression molded electrodes, while X-10 was assembled using injection molded ones. Active area dimensions were identical for the two electrode types. However, the compression molded parts required the use of two (2) separate flow frames (one on either side of the electrode) where those made by injection molding were of a unitized design. The flow channels were molded into the frame, making them an integral part of the electrode. This reduced the part count of the average cell to one electrode, one separator and two Vexar spacers. An added advantage of the newer type electrode was its improved dimensional uniformity, which eliminated tolerance buildup problems we had experienced with the X-3 module. The current collectors and feed blocks were identical to those used in X-3 modules.

III.2.2 Special Design Considerations

Figure III-6 is a sketch of the X-10 battery system. It shows three X-3 modules bolted to a master feed block, with the battery module assembly resting on top of the electrolyte reservoir. The reservoir was a rectangular polypropylene tank and contained a total of 78 l of electrolyte. It was partitioned inside to separate anolyte from catholyte. Electrolyte was circulated by means of two AC motor driven, magnetically coupled centrifugal pumps through 1 in. I.D. rigid PVC piping. Two throttling valves located near the pump outlets were used to adjust and to control the 22 l/min flow rate. Flow meters located inside the PVC piping provided visual indication of the flow rates. A 4-way valve in the catholyte line facilitated initial filling and, when needed, gas expulsion. The electrolyte was fed into the master feed block which had machined main distribution channels, designed to distribute the incoming electrolyte stream evenly among the three modules. Similarly, electrolyte from the exit manifolds was channeled into a single stream for return to the reservoir.

Shunt current protection electrodes were of the "internal" type, as described earlier. A small constant displacement pump was used to supply the required Br_2 complex. Bromine feed lines were initially in parallel configuration. However, the low flow rate used occassionally caused severe maldistribution. Connecting the lines in series proved to be a more satisfactory arrangement. (The amount of Br_2 needed to keep Zn from depositing in the manifold is less than 2 g/h, which requires a very low feed rate).

Waste heat generation was also considered, and projections based on our experience with the X-3 modules dictated some active form of heat removal. Accordingly, a small water-cooled heat exchanger was included in the anolyte tank. Because X-10 was the largest circulating zinc-bromine bipolar battery assembled for testing to date, the system was extensively instrumented for performance monitoring. In addition to battery voltage and current, individual cell voltage probes were included in each of the stacks. Individual manifold voltages (to regulate the shunt current protection power), current distribution among the individual battery modules, and electrolyte flow rates and temperature were also monitored. For the voltage probes, approximately 1/16 in. x 1 in. pieces of 0.001 in. platinum foil were used. Platinum voltage probes had been used extensively on smaller batteries with no apparent ill effects. In this case, however, they proved to be troublesome, as will be discussed later.

III.2.3 Cycling Regime

Four X-3 modules were assembled for the X-10 unit, with one module serving as a backup. Each module was pretested individually to ascertain that it functioned normally. The tests consisted of several (5-8) charge-discharge cycles at current densities of 10-20 mA/cm^2.

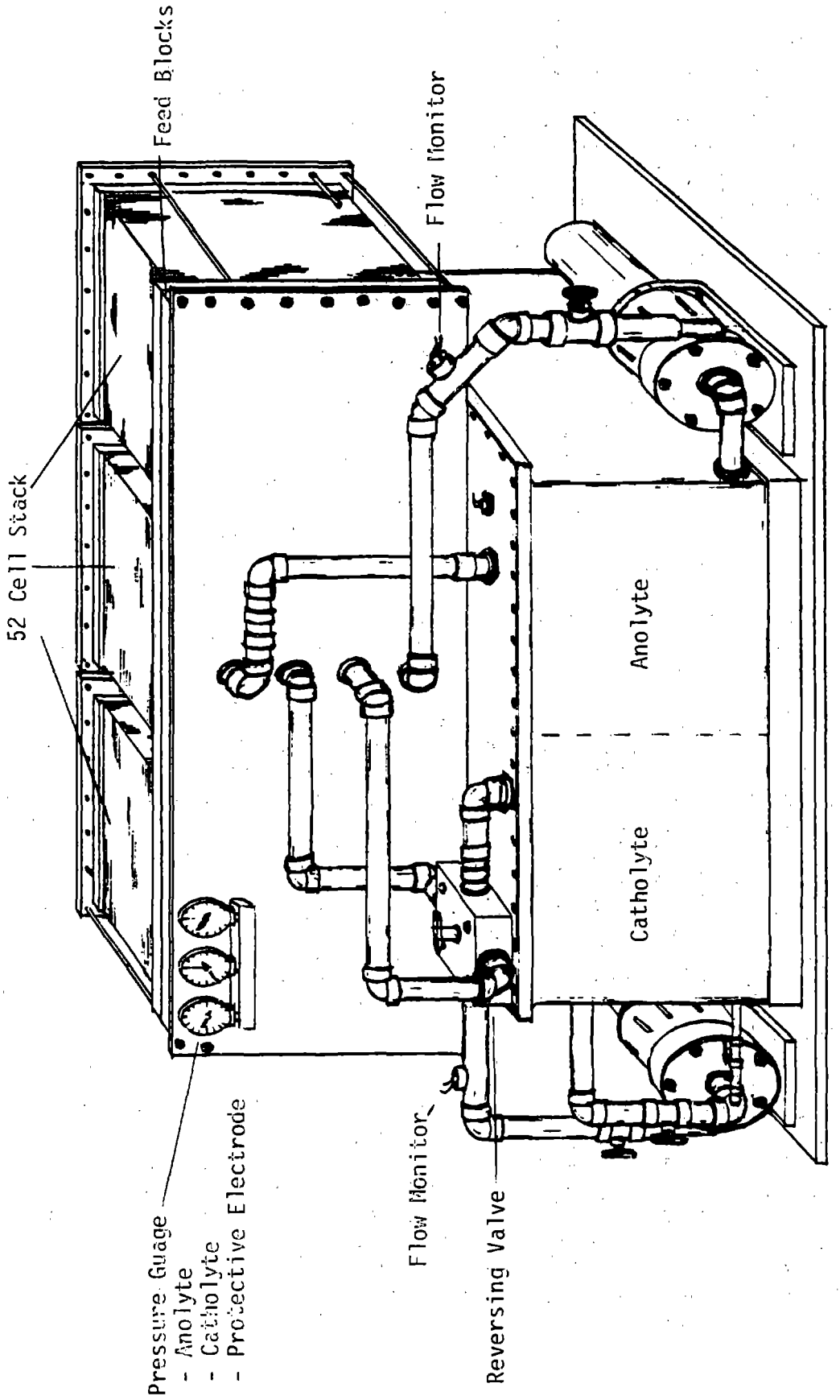

Figure III-6 X-10 BATTERY SYSTEM

Several discharges were carried out at varying rates to generate polarization and power curves for each of the modules. Two molar $ZnBr_2$ electrolyte was used to pretest the modules, and the same 27 l of solution was used for each of the modules. Following these preliminary tests, each module was rinsed with 1 M KBr solution, followed by two rinses with de-ionized water. The modules were stored in a wet condition while awaiting assembly of the X-10 unit. Testing of X-10 consisted of a repetitive charge-discharge cycling routine, using 78 l of standard electrolyte (3 M Zn/Br_2 - 1 M Br_2 complexer). Charging current ranged from 26.1A to 43.5A (34.8A predominantly) for a sufficient time to achieve the desired input. Discharge was at the same rate to 50V (1V/cell). At the 50V mark, the discharge current was reduced to 10-15A to bring the battery voltage to zero before overnight shorting.

III.2.4 X-10 Battery Performance Characteristics

Figures III-7, III-8, and III-9 are polarization and power curves for X-10 modules A, B and C. The slopes of the lines are 5.5, 4.8 and 6.3 ohm-cm^2, respectively. The spread in these values is greater than that suggested by the observed current distribution among the three modules when operated in parallel as a single battery. Evidently, at the time the V vs I curves (Figures III-7 - III-9) were generated, differences in electrolyte conductivity must have existed (due to differences in concentration at varying states of charge), which account for the spread in the internal resistance values. The performance of the individual stacks, however, was sufficiently uniform to go ahead with the assembly of X-10.

Cycle testing of X-10 started off in routine fashion. Charging and discharging were done at 34.8A (20 mA/cm^2) with charge times increased from 2 hrs for the first few cycles to 3-4 hrs. A 3 hr charge at 34.8A represented a 10 kWh input at a 60 mAh/cm^2 zinc loading. Temperature rise of the electrolyte, measured in the reservoir, averaged approximately 20° over the initial value at the end of the discharge cycle. This was remarkably close to the thermal behavior observed on individual X-3 modules. A voltage plot for such a cycle is shown in Figure III-10. Here, coulombic efficiency was 71%, and voltaic efficiency was 85%. Such performance was typical for 30 cycles, as shown in Figure III-11, where coulombic efficiency vs cycle number was plotted. The values (average 70.2%), while consistent, are 10% lower than anticipated, based on performance results obtained on X-3 and 500 Wh (12V) modules. The cause of the lower efficiency was a cross-flow condition in the X-10 feed block, under which some catholyte seeped into the anolyte stream. Bromine complex in the anolyte reduces coulombic efficiency due to the direct reaction between bromine and elemental zinc. Since correcting this condition would have been time consuming, a decision was made to proceed with the testing, and to correct this condition in X-20 with an appropriate design modification. Accordingly, cycle testing of X-10 proceeded. However, severe gassing at the anode, with an accompanying loss in performance developed past cycle #30. There is strong evidence pointing to platinum contamination of the electrolyte as the cause of this gassing problem.

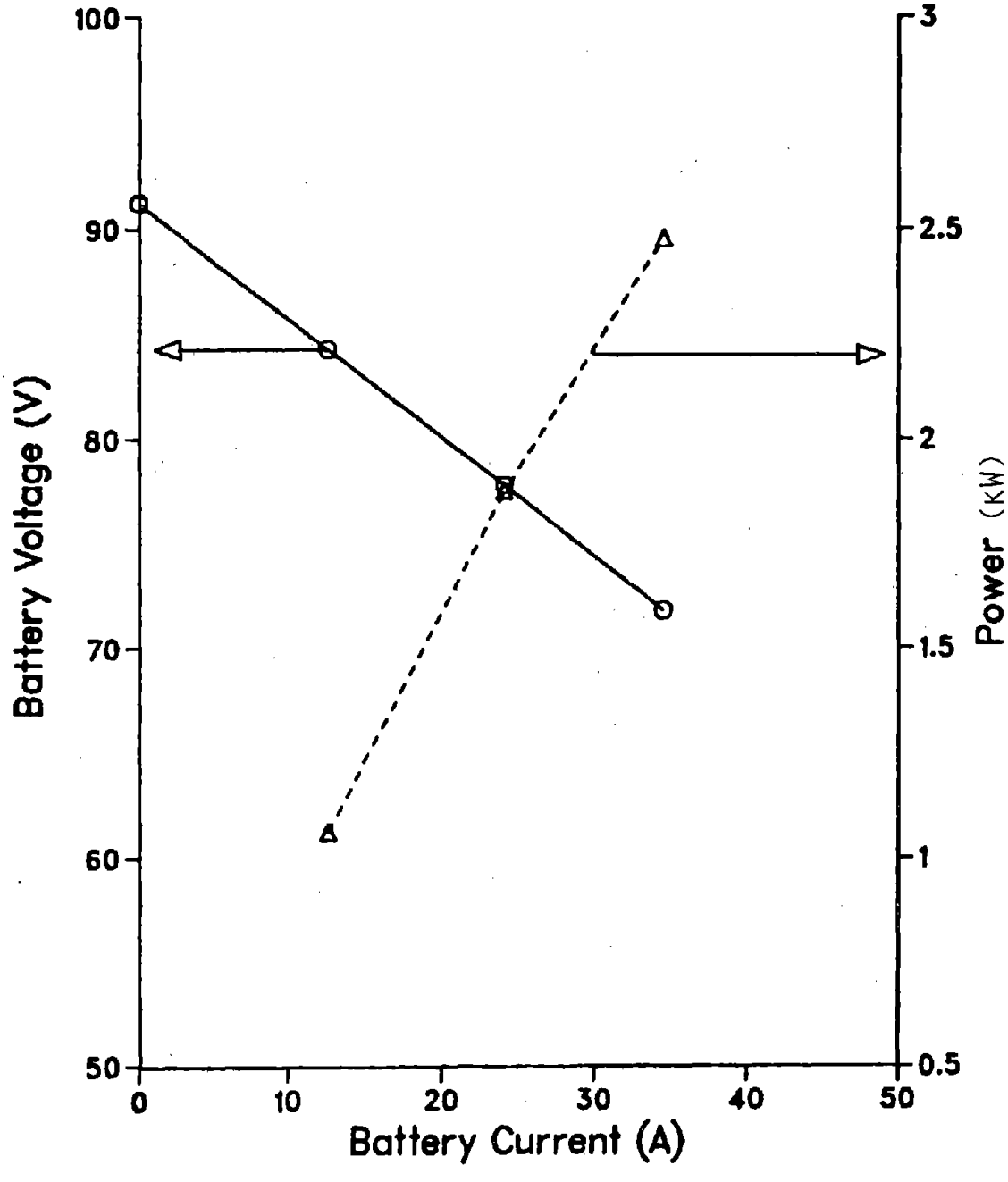

Figure III-7. X-10 Module A. Polarization and Power Curves

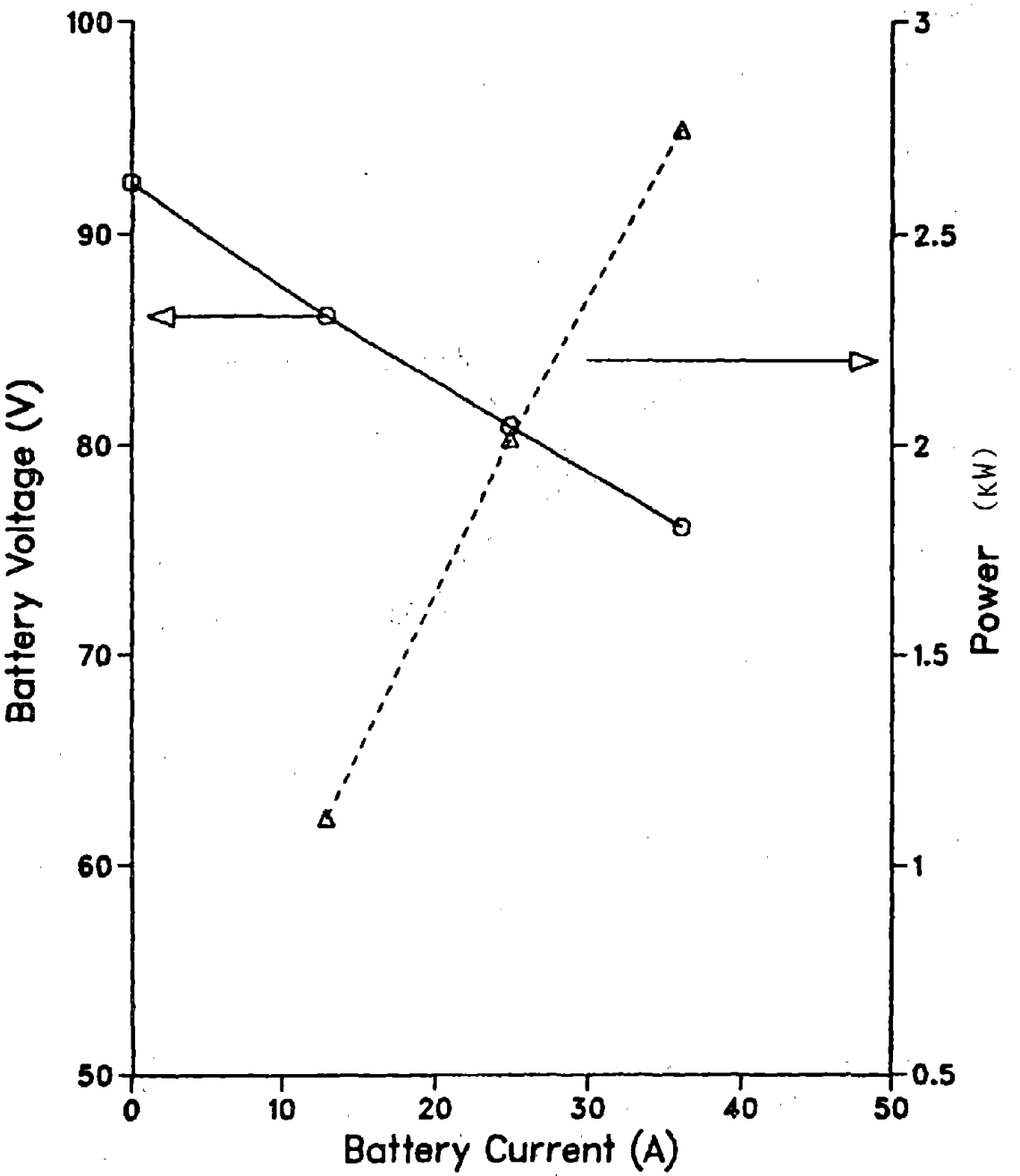

Figure III-8. X-10 Module B. Polarization and Power Curves

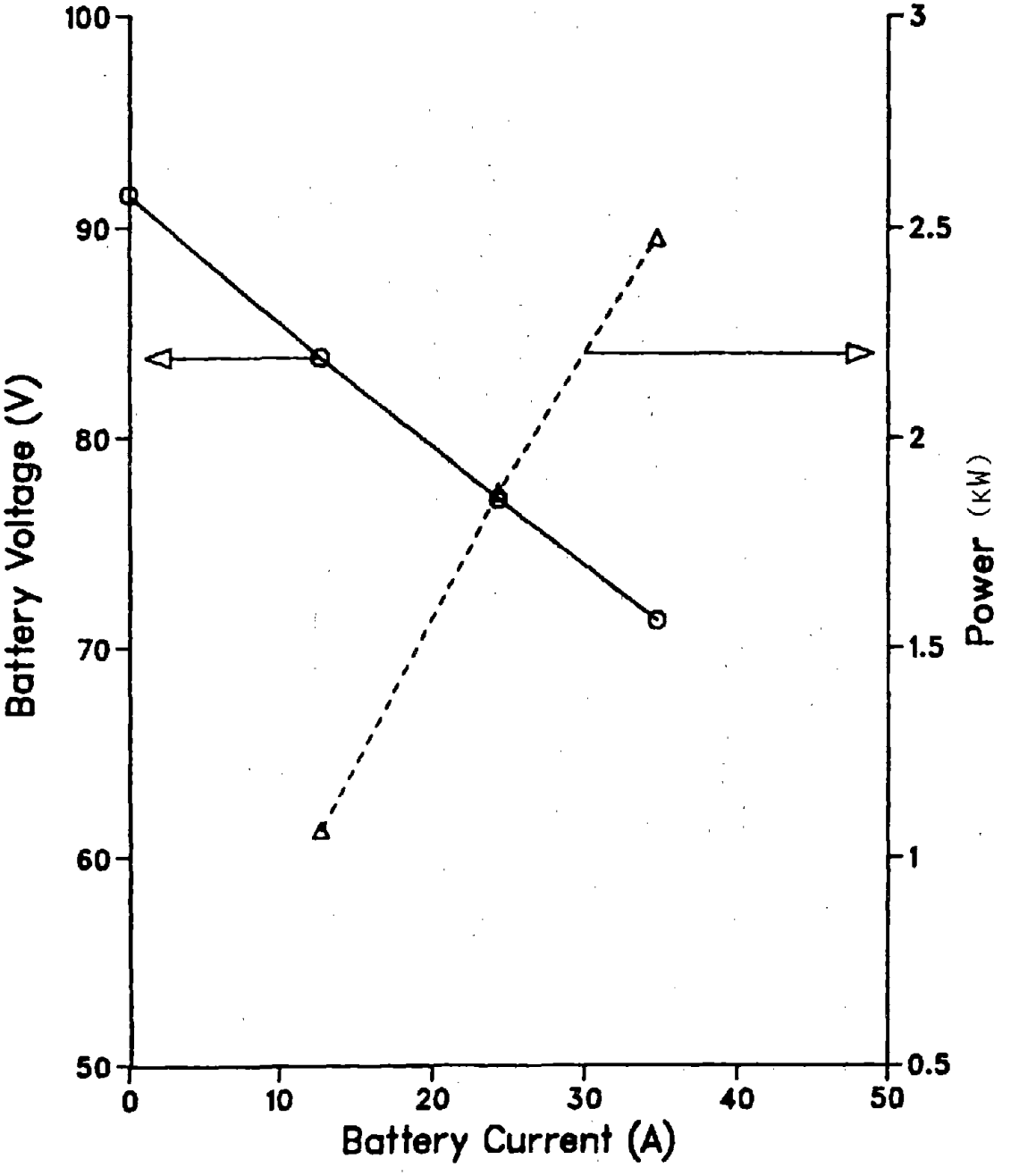

Figure III-9. X-10 Module C. Polarization and Power Curves

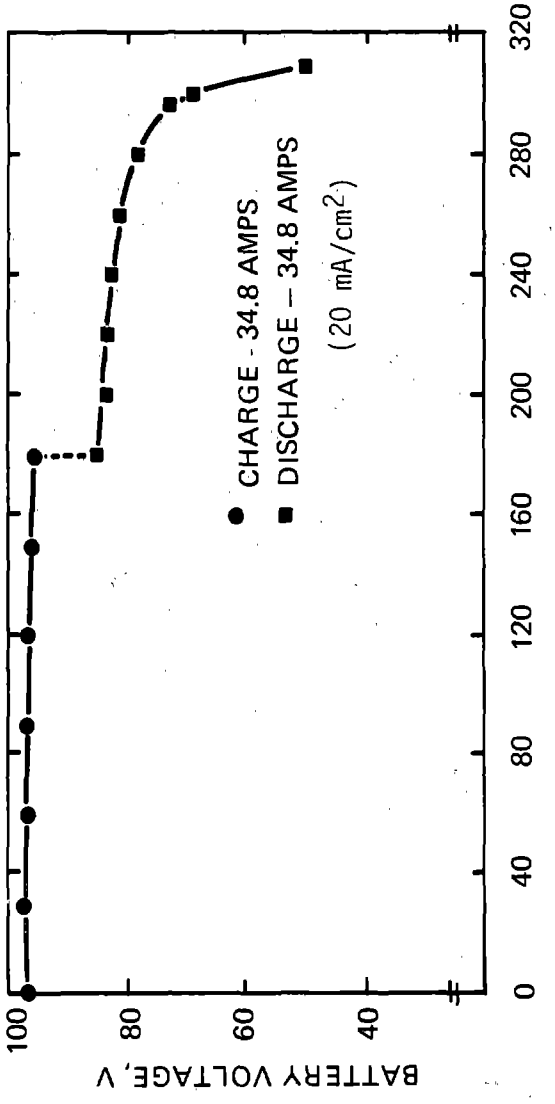

Figure III-10 Battery X-10, Voltage vs Time (Cycle #17)

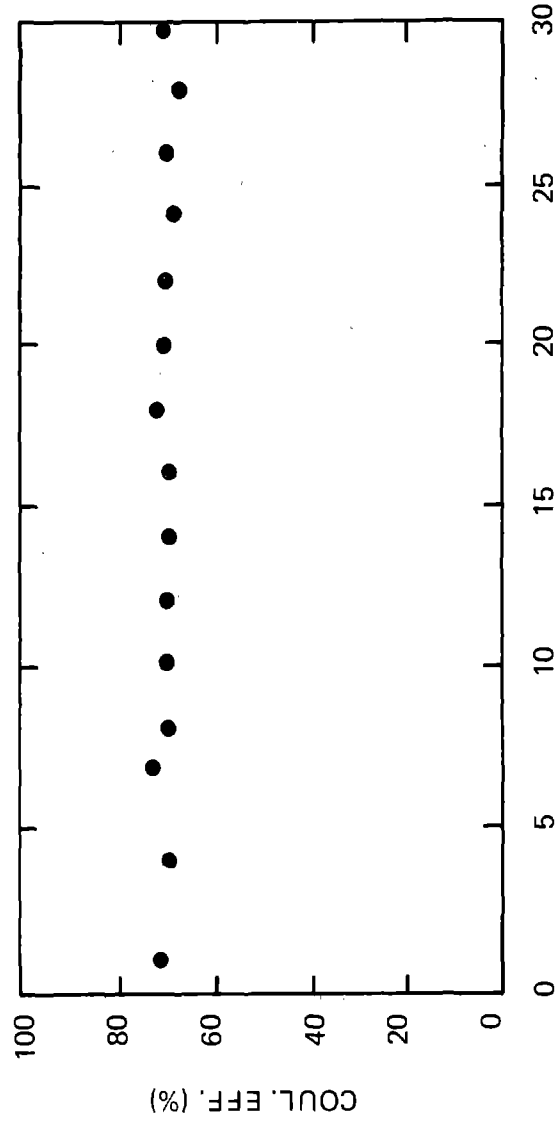

Figure III-11 Cycling Performance of Battery System X-10
(Charge/Discharge Rates 34.8-43.5 Amps
Charge Time 3-4 Hours

As described earlier, X-10 contained platinum voltage sensors, as diagnostic probes, for monitoring battery performance. These platinum probes were in contact with the cathode side of the bipolar electrodes. Earlier practice had been to locate these platinum voltage sensors on the Zn side of the bipolar electrode. However, periodically, a sensor would behave erratically, which was suspected to be due to zinc bridging. As a result, the X-10 voltage probe location was changed. As cycle testing proceeded, a very gradual increase in gassing was noted at approximately the 20th cycle mark. The gassing was in the anolyte, and based on earlier work, it was presumed to be hydrogen. At first the gassing was so slight it was almost ignored. As cycling proceeded, however, the gassing became more intense. Initially, the onset of gassing was observed at the end of discharge. Gradually gassing appeared earlier in the cycle. Past cycle #30, the onset of gassing was observed to have started before the end of charge. Perhaps more importantly, the intensity of the gassing seemed to increase significantly; so much so in fact, that coulombic efficiency began to decline. Between cycles #40 and #58, gassing became so copious that coulombic efficiency dropped below 60%, and each successive cycle yielded a lower capacity. This is shown in Figure III-12. One effect of this gassing was an increase in electrolyte pH, and frequent additions of HBr were required to maintain it in the 2.5-3.5 working range.

As the gassing condition in the battery was developing, considerable thought was given to its possible causes. The most probable cause pointed to electrolyte contamination. It is well known that certain metallic impurities, even in the low ppm range, can alter the gassing characteristics of batteries by lowering the hydrogen over-potential. In our case, platinum and iron were suspected contaminants in the electrolyte. Trace analyses of electrolyte samples at various stages in cycling yielded the following results:

Table III-1

Trace Analyses of X-10 Electrolyte

	Pt	Fe	Mn	Mg	Al
Initial values	< 0.5	< 0.1	< 1	-	-
After 25 cycles					
Anolyte	4	1	< 1	2	2
Catholyte	3	1	< 1	2	2
After 37 cycles					
Anolyte	20	5	< 1	1	4
Catholyte	7	5	< 1	1	3

Note: Initial values represent lowest detection limits. Values are in ppm.

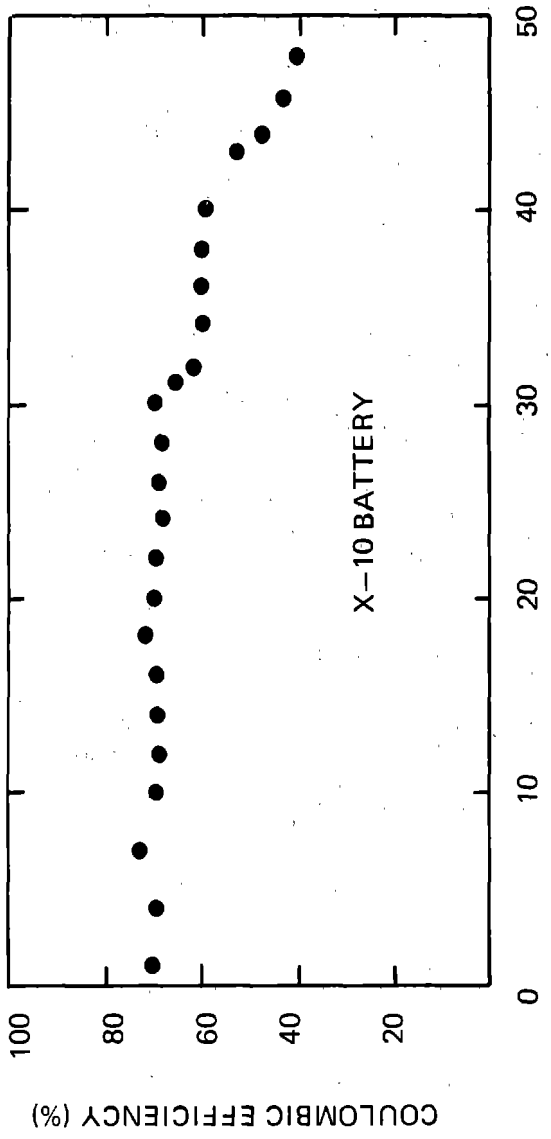

Figure III-12 Coulombic Efficiency vs Cycle No. Battery X-10

These results indicate a significant increase in the platinum content of the electrolyte. The source of the platinum contamination was the voltage probes. This was confirmed by removing and examining the Pt tabs, which showed signs of being etched. That Pt was the primary cause of the gassing was confirmed in a bench top test tube experiment. To four (4) test tubes containing "standard" electrolyte, very small amounts of hexachloroplatinic acid were added (1.1-15.3 ppm). A fifth sample was kept as a control, and a sixth sample was X-10 anolyte from the 25th cycle. A small amount of metallic zinc was placed in each of the test tubes, and gas bubble formation on the zinc was observed. All electrolyte samples containing Pt showed a greater tendency to gas than the control. The coverage of the zinc test samples by gas bubbles increased with increasing Pt content. In fact, with Pt in solution, one could see gas bubbles rising in the liquid. Gassing in the control sample was inperceptible. No attempt was made to quantify these findings.

The association of Pt contamination with gassing was demonstrated on module X-3D (the X-10 backup). This battery also showed gassing on charge/discharge cycling. Analysis of the electrolyte showed it to contain 30 ppm of Pt. At this point, the battery was drained, and after removing the Pt voltage tabs, filled with a solution that was approximately 0.5N KBr, 0.1N HBr and 0.2N Br_2. A low current (2 mA/cm^2) was passed through the stack for 30 minutes. The "cleaning" solution was dumped, refilled with a fresh solution of the same composition and the procedure repeated, with the current passed in the reverse direction. This solution was also dumped, and the battery was then rinsed twice with de-ionized water. The rationale here was to operate the battery as a Br_2/Br^- couple, (to avoid gassing), while passing a low current to oxidize any residual Pt on the electrodes to form hexabromoplatinic acid. This procedure was effective because when X-3D was retested with fresh electrolyte, the gassing "problem" had been "cured". Gas generation before the cleanup was measured in liters per cycle. Following the cleaning, gassing was reduced to a few ml per cycle.

IV. Parametric and Component Testing

This portion of Phase I was concerned with broadening the experimental data base for the zinc-bromine battery. Particular objectives were to qualify new components for eventual incorporation in the large system demonstrations, to investigate various technical parameters and interrelationships that limit system performance and to design and extend knowledge on possible life limiting mechanisms of individual system components.

IV.1 500 Wh Parametric Test Station

IV.1.1 Design of Standard Station

The 12 V 500 Wh bipolar battery test station, shown in Figure IV-1 is comprised of three major component parts:

- Battery Module
- Electrolyte Storage and Circulation
- Operating Control and Monitoring

The battery module is a 12 V (8-cell), 500 Wh bipolar unit, consisting of:

7 Bipolar Electrodes
2 Current Collectors (one Positive and one Negative)
8 Microporous Separators
16 Vexar Screen
2 Feed Blocks
2 Aluminum End Plates

The end plates constrain the battery module, making it leak-tight. Four manifolds, one in each corner, facilitate electrolyte circulation through the battery module, one each for anolyte and catholyte entry and exit. Two current leads connected to a power supply are used to charge and discharge the battery. In addition to battery voltage sensing leads, individual cell voltage sensors are included for monitoring battery performance.

The electrolyte is contained in two polypropylene reservoirs (anolyte and catholyte) connected to the battery module manifold with 1/2 in. I.D. polypropylene tubing and compression fittings. Circulation is effected by means of two 12 V DC magnetically-coupled, centrifugal pumps. Anolyte enters the battery in the lower left-hand corner, flows up, and exits in the upper right-hand corner, where it is returned to the anolyte reservoir. The catholyte enters the battery in the upper left-hand corner, flows down, and exits in the lower right-hand corner, returning to the catholyte reservoir. A 4-way valve in the catholyte feed line makes it possible to reverse flow direction to expel air on initial filling, as well as any gas which may be generated during operation. Two pressure gauges in the feed lines serve primarily as a visual indication that electrolyte flow rates are "normal", 25 ml/min. dm^2 of electrode area. For a 12 V battery, the flow rate is 1.2 l/min.

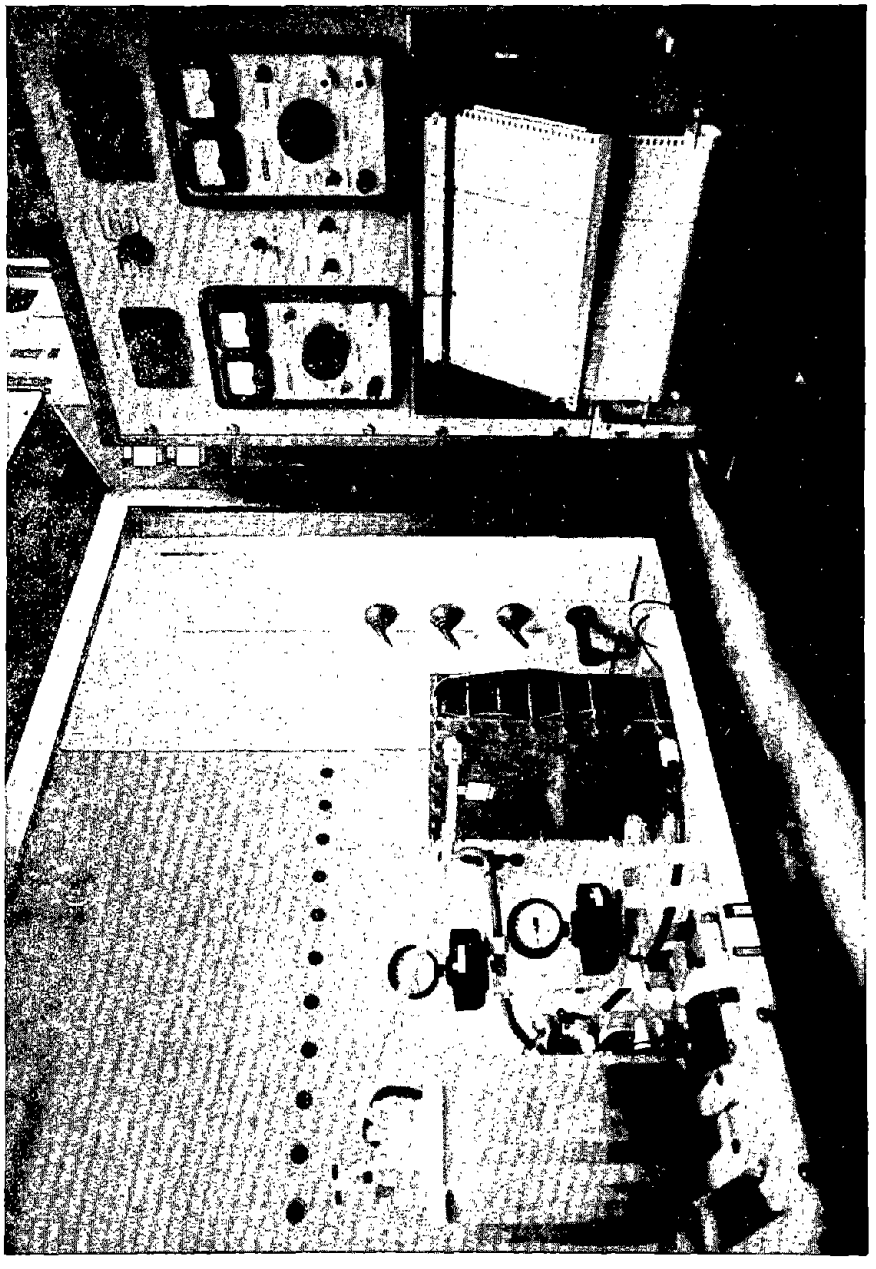

Figure IV-1 12 V Bipolar Battery Test Station with Battery on Charge

The cycler panel shows two digital panel meters (for battery voltage and current), a 9-position selector switch (8 individual cell voltages and battery voltage), two 12 V battery chargers (used to power the electrolyte circulating pumps), three toggle switches, a 2-pen strip chart recorder and a regulated power supply. The toggle switches control battery operation on charge, discharge, and even circuit. The shorting switch places the battery across the load resistor. Figure IV-2 is a simplified schematic diagram of the cycler panel. The load resistor, (a wound nichrome wire of 2 ohm, 300 W rating) is in series with the power supply when the battery is in the discharge mode, to avoid accidental shorting while the battery is on charge.

IV.1.2 Component Testing

The 12 V (8-cell), 500 Wh bipolar battery design was generated in the early phases of Exxon's zinc-bromine system development program when active electrode area was scaled up from 100 cm^2 to 600 cm^2. Since then, a number of such units were assembled and tested with the result that a useful data base was gathered. Because at the 8-cell level, testing could be carried on without the added complexity of shunt current protection requirement, this system proved useful as a test bed for evaluating battery components. Microporous separator material and the injection molded electrodes, are but two examples of components that were extensively evaluated in 12 V systems before testing their performance in larger, 52-cell modules. Qualification of new vendors (such as for $ZnBr_2$) was also done on the basis of obtaining satisfactory performance results in a 12V system. This system also proved useful for conducting parametric testing, where performance characteristics were evaluated as a function of operating parameters.

IV.1.3 Parametric Testing

Parametric tests at the 12 V (8-cell) battery level indicated that higher coulombic efficiencies were obtained at lower states-of-charge (100% SOC was defined as the condition when 100% of the $ZnBr_2$ in the electrolyte had been utilized. A 12 V battery, such as the one used in these tests, was normally filled with 4 l of 3 M $ZnBr_2$ electrolyte, which based on a 90 mAh/cm^2 Zn loading, represented a 65% material utilization. This fill level was selected on the basis of retaining a sufficient salt concentration at the end of charge to maintain adequate electrolyte conductivity.

These tests indicated that low material utilization (30%) yielded a 90% coulombic efficiency, and as material utilization increased, coulombic efficiency decreased. The observed trend was as shown in Figure IV-3, where coulombic efficiency decreased from 90% to 80% as material utilization increased from 30% to 65%. The corresponding zinc loadings are 40 mAh/cm^2 to 90 mAh/cm^2. These observations were examined further by increasing the total amount of electrolyte in the system to 6 l

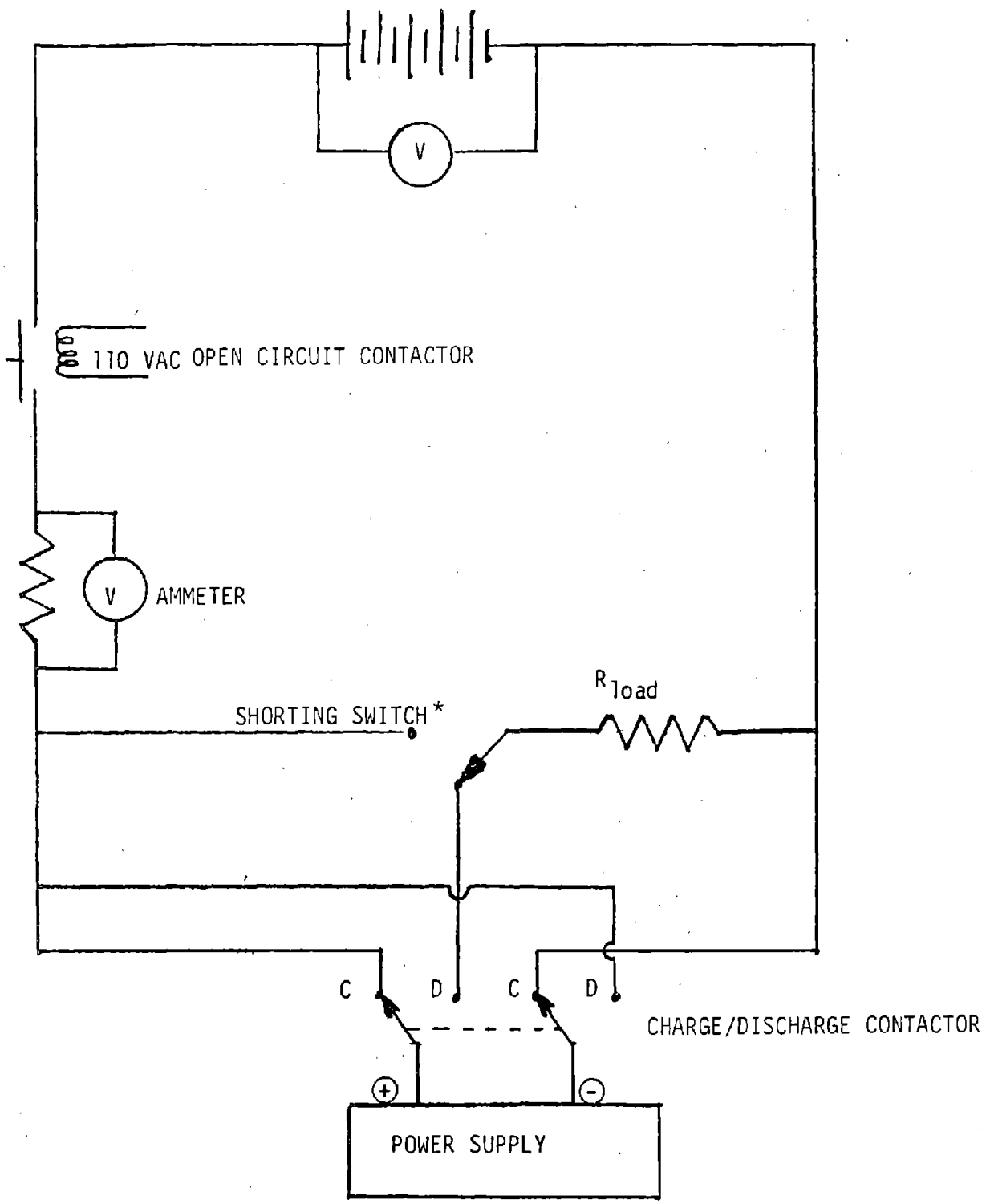

Figure IV-2 Schematic of Cycler Panel

*Shorting Switch Operable Only in Discharge Position

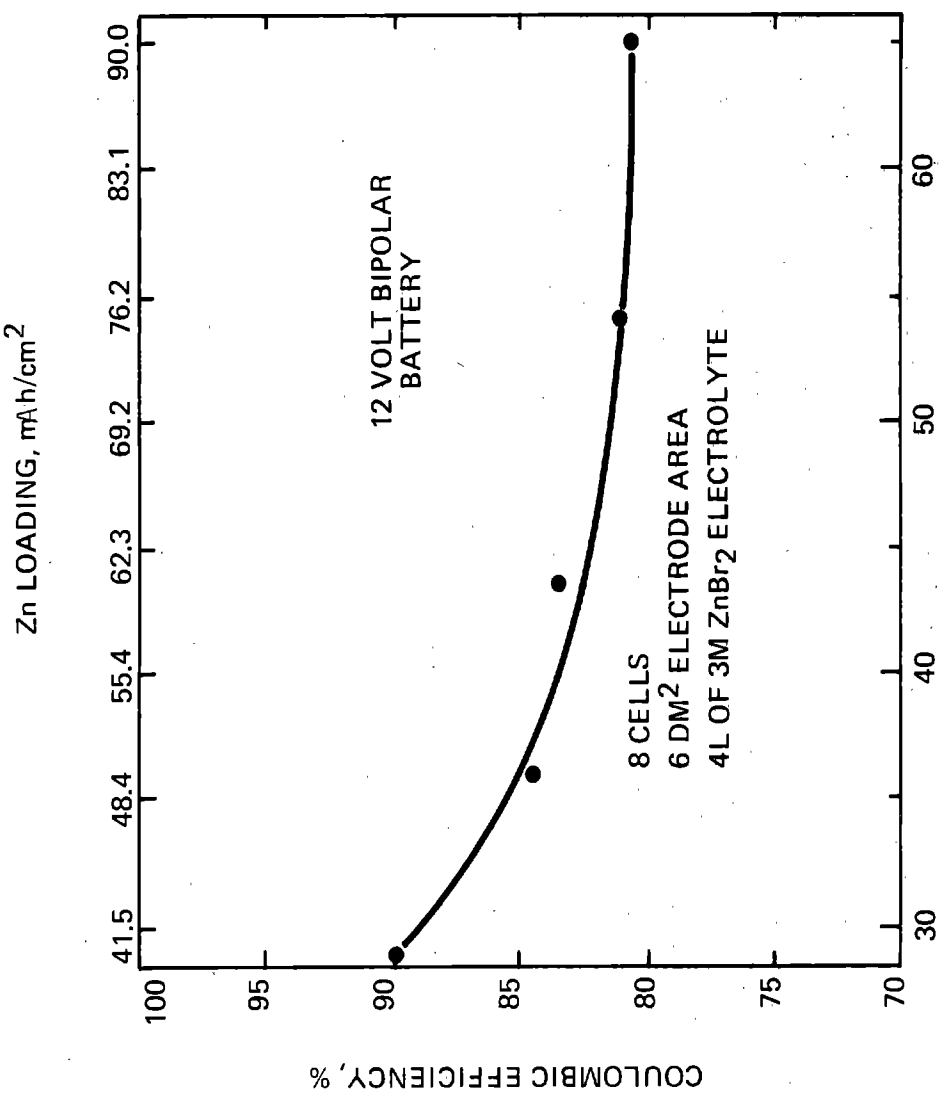

Figure IV-3 Effect of Material Utilization on Coulombic Efficiency

This in effect reduced the material utilization (M.U.)for comparable zinc loadings. For example, a 90 mAh/cm^2 zinc loading represented 65% M.U. for 4 l of solution, and 32% M.U. for 8 l of solution. These tests indicated that at 70% M.U. and below, lower zinc loading and the corresponding charge time increased coulombic efficiency. This observation is consistent with our understanding that Br_2 formed at the cathode can migrate through the separator into the anolyte where it can react directly with elemental zinc on the anode, thereby reducing coulombic efficiency.

IV.1.4 Automatic Life Cycle Testing

Key to the determination of the cycle life capabilities of the Zn/Br_2 battery system is the establishment of a reliable automatic test station which will allow continuous battery cycling. A test station has been constructed which allows around-the-clock cycling of a shunt-current protected 500 Wh 8-cell stack. The electrical circuitry which controls the basic charge-discharge cycling of the battery is controlled by a Texas Instrument Programmable Control System (Model 5TI). The present station is hardwired to allow for cycling regimes involving two different charge and two different discharge currents (which allows pulse charge/discharge capability). The shunt current control system is monitored and controlled by a separate unit which operates independently of the cycling apparatus as do the system pumps. The present test station incorporates separate system safety circuitry to monitor both catholyte and anolyte pressure and electrolyte reservoir liquid levels. Future stations will interface these sensors to the 5TI microprocessor controller to shutdown the system due to pump malfunction, electrolyte leakage, or flow blockage. Stack performance is monitored by a dual channel recorder (stack voltage and current) supplemented by a data logger which also records individual cell voltages and shunt current system parameters. Figure IV-4 shows a block diagram of the life test system as presently configured.

Initial attempts at life cycle testing led to early aborts with two cell stacks, caused primarily by poor flow distribution in life test stack #1, and shunt current control system malfunction in life cell test stack #2. Life test stack #3, now under test at the writing of this report, incorporates two modifications to overcome these problems: (1) elimination of the separate flow frame element in cells 1 & 8 by molding of the flow distribution network into the current collector itself (previously separate flow frames were necessary with flat, compression molded collectors); (2) operation of the shunt current negative electrode feed system via the catholyte pump rather than a separate bellows pump. As of March 31, 1981, life test stack #3 had accumulated more than 100 continuous cycles of operation at various depths of discharge corresponding to Zn loadings of 10-75 mAh/cm^2 with an average coulombic efficiency of 80%. Cycling of this unit will continue into phase II of this contract during which a second life test station will be put into operation.

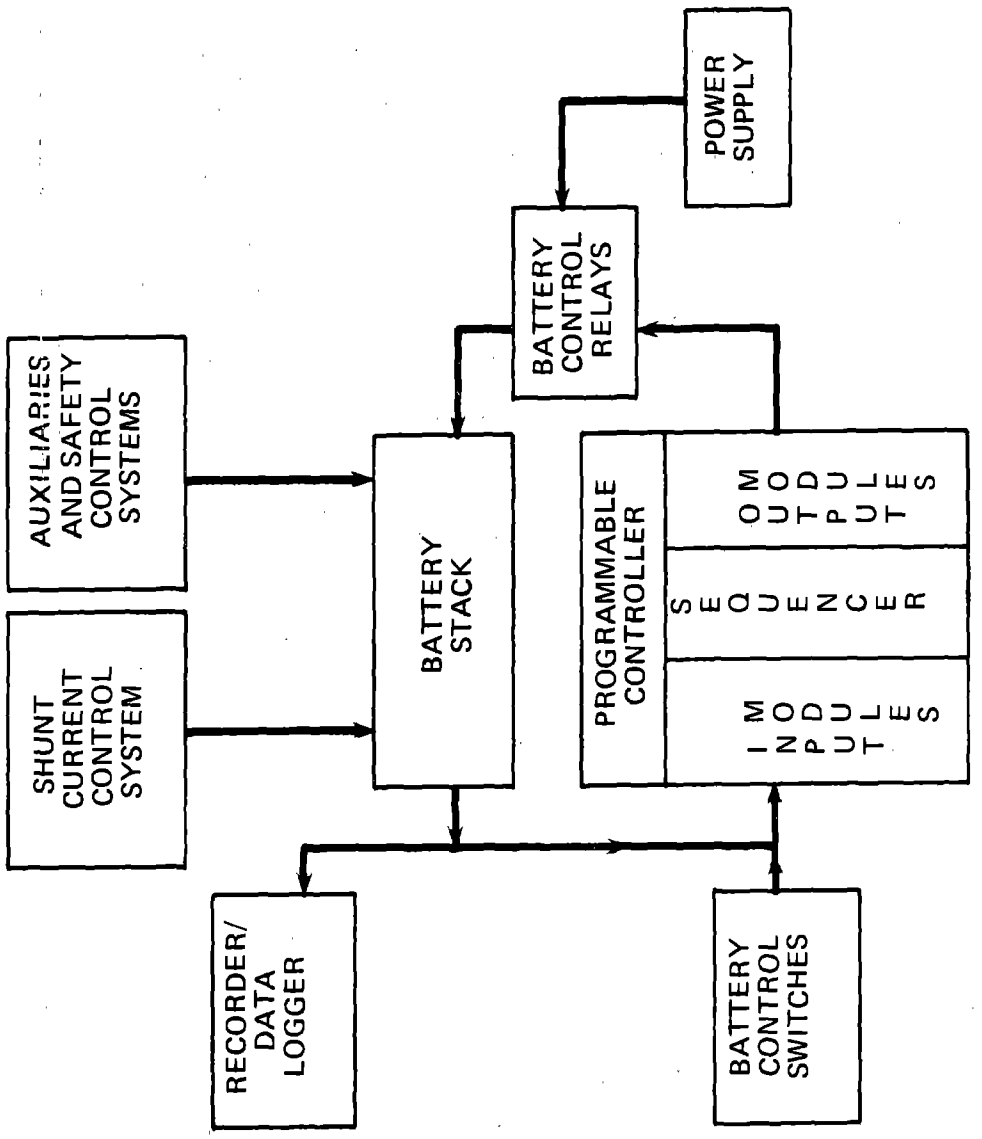

Figure IV-4 Controller Logic for Automatic Life Test Station

IV.2 Tunnel Shunt Current Protection Testing

An experiment was run to test the concept of tunnel protection in a functioning zinc-bromine battery system (see Section II.3 Shunt Current Protection). A 19 cell battery stack was assembled with special flow frames to allow tunneling. A unit cell is shown in Figure IV-5. It consists of a bipolar electrode, a flow frame with channels facing the electrode, a microporous separator, a flow frame with channels facing the next electrode and then the next bipolar electrode.

The bipolar electrode has a central conductive thin carbon-plastic body of 600 cm^2 area coated on one side with expanded surface area carbon for the cathode, compression over-molded with a non-conductive plastic border. The design thickness is 30 mils. The compression flow frames were specially designed for tunneling experiments (Figure IV-6). In comparison to the classical flow frame, these flow frames have an additional length of electrolyte cavity in the plastic frame to allow long narrow sections in the channel between the manifold and the cell electrolyte compartments. The location of the external edge of the manifold holes is inboard 1.25 inches from the classical design. The flow frame thickness was designed to be 24 mils. The cell electrode area of the flow frame is 530 cm^2. Two flow frames are used, one with a 180^o orientation, in the unit cell.

The 24 mil thick microporous separators were cut to be of the same gross area as the cell stack, thus extending to the external edges of the stack. The terminal anode and cathode electrodes were compression molded with embedded screen for current collection. Four 3/8 inch manifold forming holes were cut in each component comprising the unit cell. In addition, four tunnel holes were drilled through each plastic component (but not the microporous separators) near each manifold to form four "tunnels" through the stack. These tunnels formed interconnections between the channels for each of the anolyte and catholyte inlet and outlet streams.

The tunnels in each unit cell go through the plastic of the flow frame, from the electrolyte channel, through the microporous separator, through the solid portion of the next flow frame, through the non-conductive portion of the bipolar electrode, to the next electrolyte channel. This is shown in Figure IV-5 with lines connecting "tunnel" holes. The nominal design "effective" tunnel length, considering the tortuosity of the microporous separator, is 0.125 inch.

Tunnel theory requires that there be a gradation of resistance from cell to cell interconnection, increasing toward the center of the stack and then decreasing toward the terminal end cell. The hole diameter and the cross-sectional area, and thus the resistivity of each tunnel segment is not the same in each type of component. In addition, when viewed from the side, the tunnel resistances within each unit cell start at different points, i.e. at the anode face to the next anode face and from the base of the catholyte channel to the next catholyte channel base. The catholyte and anolyte tunnel holes in the flow frames thus have different diameters.

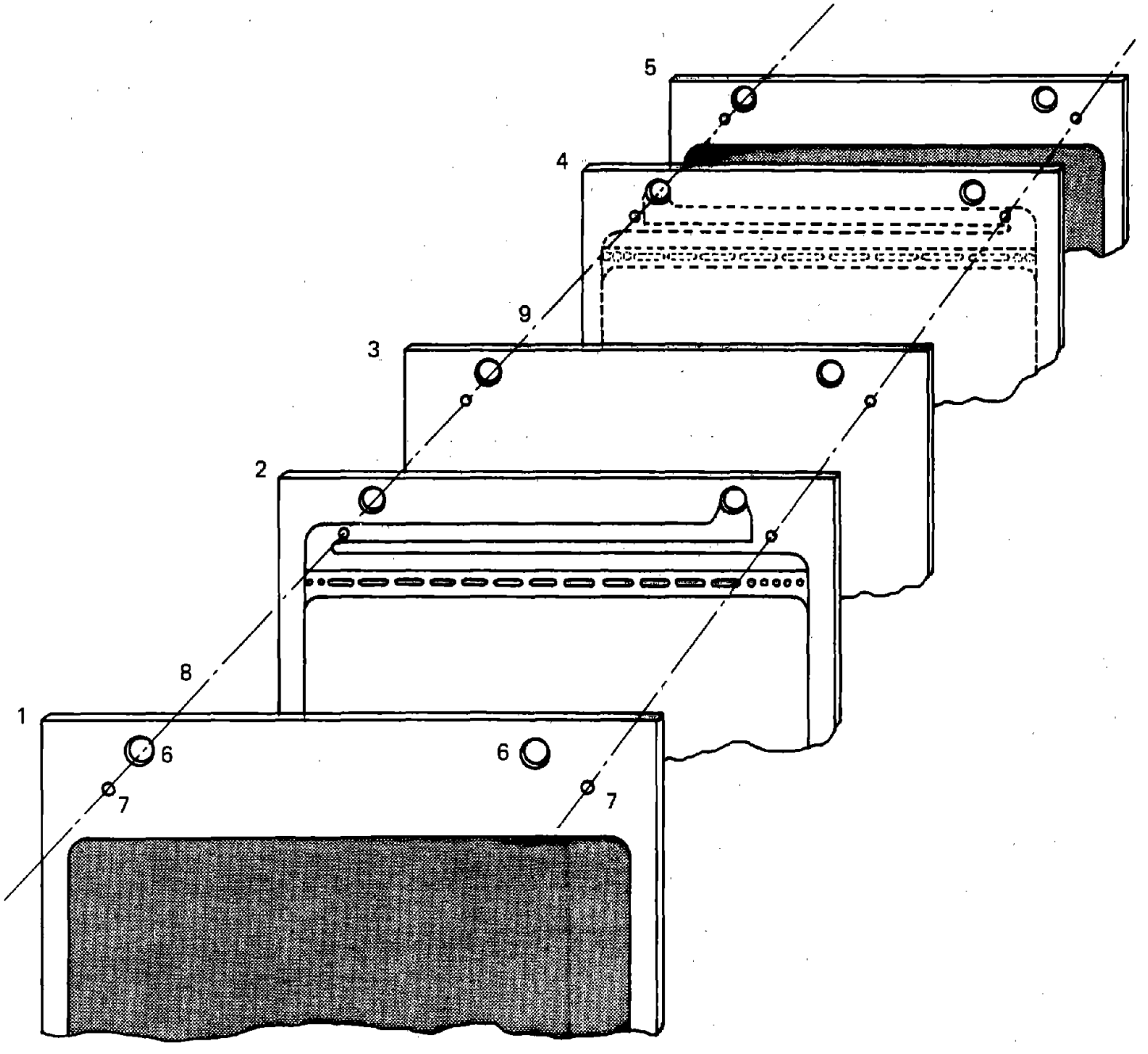

1,5 BIPOLAR ELECTRODES
2 ANOLYTE FLOW FRAME
3 MICROPOROUS SEPARATOR
4 CATHOLYTE FLOW FRAME
6 MANIFOLD HOLES
7 TUNNEL HOLES
8 ANODE COMPARTMENT
9 CATHODE COMPARTMENT

Figure IV-5 Unit Cell From "Tunnel" Protection Experiment

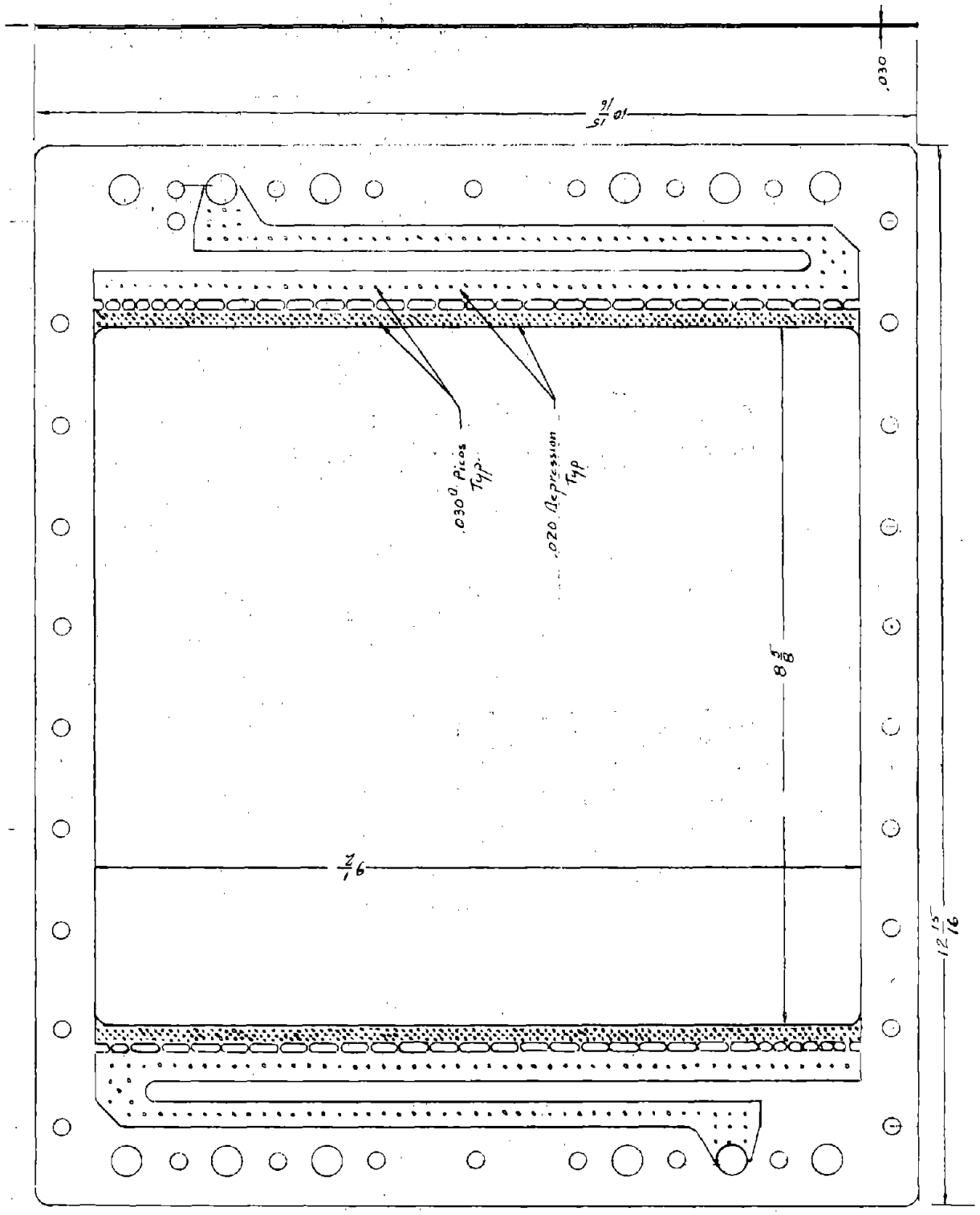

Figure IV-6 Compression Molded Flow Frame

For minimum protective tunnel currents, it is required that the tunnels in the center of the stack have infinite resistance and that the tunnels on either side of the stack center have very high resistance. This would require very small tunnel holes in this design and would present great practical difficulties in alignment of the tunnels in the stack. The center tunnels were thus chosen to have finite resistances, consequently modifying the remaining tunnel values to lower resistances.

The size of the holes was computed from the resistance values calculated from formulas given in Section I.3 and Appendix 5 using the values in Table IV-1. Drill sizes close to the computed values were used to jig drill the tunnel holes in the components. The resistance values of the tunnel ends kept these protective electrode supply streams separated from the main electrolyte streams where necessary.

The insert protective current per tunnel computed from these values is about 15 mA, compared to the 260 mA per manifold for the equivalent manifold protected case. Four tunnel protective electrodes were placed in each feed block at the junctions of the tunnels in each of the terminal electrodes. These electrodes were supplied with bromine rich electrolyte from catholyte slipstreams. Microporous inserts in the tunnel ends kept these protective electrode supply streams separated from the main electrolyte streams where necessary.

The stack was assembled between metal plates with external bolts. The flow frame thickness tolerance was very bad. The frames were considerably thicker in the center portions, top and bottom (there is more plastic material to move in these regions during the compression molding and this movement resistance makes for a thicker cross section). The cell stack initially leaked, even under high torqueing of the stack tie bolts. Plastic wedges inserted between the metal backing plate and the feed block together with reinforcing bars, eventually eliminated all leaks. However, this gave a system with double concave cell stacks and nonparallel electrodes. The alignment of the tunnel holes and the resistive path length through the tunnels is open to question.

During the stack assembly, platinum tabs were inserted in the catholyte compartments of each cell for cell voltage measurements. In addition, 4 platinum tabs were placed at the tunnel channel nodes in the terminal cells and at every 4th cell to measure tunnel node/cell voltages. Computer connection wires were soldered to each of these tabs. Unfortunately, during the placement of the stack in the test stand, many of the tab connections were broken at points where repair was inaccessable. Some of the broken tab connections were at the more critical locations.

The cell stack was run in the conventional manner, analogous to X-3A. When the protective current was applied to the tunnel electrodes, the voltage of the cells in the center of the stack increased as expected from theory. When the voltage between the sensor tabs in tunnel/channel nodes at the terminal cells approached the stack terminal voltage, the voltage of all the cells in the stack became more uniform.

Table IV-1

RESISTANCE VALUES FOR TUNNEL CALCULATIONS

V_o = 1.78 volts	I = 0
R_m = 6.68 ohm	R_e = 0.04 ohm
R_c = 7000 ohm	P = 15 ohm-cm
$RT_{N/2}$ = 333 ohm	N = 19 cells

Tunnel Number	Resistance, ohms
R_T 1	123
2	145
3	169
4	199
5	232
6	251
7	298
8	332
9	332
10	332
11	332
12	298
13	251
14	232
15	199
16	169
17	145
18	123

Simultaneously with the increase in tunnel current, the voltage differential between the terminal tunnel/channel nodes and the terminal cells decreased from an 8-10 volt condition to a few hundred millivolts. Further increase in current made the voltage differential negative. Unfortunately, this could not be checked at all points because of broken sensor tab connections.

When the voltage differences in the channel legs of the terminal cells were nearly nulled, voltages in the near cell channel legs were far from being nulled. Changing the input tunnel current could bring about near nulling in a given cell set, but not simultaneous nulling in the other sets where voltage measurements could be made. The input current to bring about a near voltage match between the terminal voltage of the stack and the voltage difference between the sensor tabs in the terminal tunnel nodes was four times higher than the calculated value, i.e., 65 mA vs 15 mA.

Reconsideration of this battery stack design pointed out a flaw in the unit cell approach, unique to this protection method. The system was designed, for example, to have the input tunnel anolyte current (10, Figure IV-7) enter the tunnel near the catholyte inlet manifold and proceed through the tunnel system. A portion (11, Figure IV-7) would split off at the anolyte channel node and proceed into the anolyte outlet manifold. A similar process would occur at the next cell. Correspondingly, input tunnel catholyte current would enter at 12 (Figure IV-7) and proceed through that tunnel system. At the catholyte channel a portion (13, Figure IV-7) would divide off and proceed through the channel into the catholyte inlet manifold. The design calculations for tunnel resistance were based upon these conditions and channel and manifold resistances in the ratio of 1050 to 1.

Unfortunately, in this design, with the microporous membrane extending to the edges, there are unintentional alternate pathways for the tunnel current. The anolyte tunnel current (10, Figure IV-7) can shunt into the catholyte inlet manifold through the electrolyte which wets the microporous membrane at 14 (Figure IV-7). Similarly the catholyte protective tunnel current can shunt to the anolyte outlet manifold at 15 (Figure IV-7). There are now in effect two parallel pathways for the protective tunnel currents to divide into the manifold system. The value of the channel resistance, R_C, is thus lower than the R_C used in the calculations for the design of tunnel dimensions and resistances. The estimated effective resistance for R_C is 800 ohms rather than the 7000 ohms used in the initial calculation. Recomputation of the value of each tunnel current using this value of R_C and $R_{TN/2}$ of 333 ohms gives 65 mA, at open circuit, rather than the previously calculated 15 mA. The experimental tunnel current values observed were in this range, when the terminal/tunnel nodes voltage difference was near the stack voltage.

With an effective R_C of 800 ohms, the actual dimensions of the tunnels are too small and thus the resistances are too large. More of the input tunnel current is diverted to the manifold than calculated. Hence, the shunt current nulling is less than exact. The system could have been rebuilt with the tunnel holes rebored to larger diameters. The resistance value for the pathway from the tunnel to manifold through

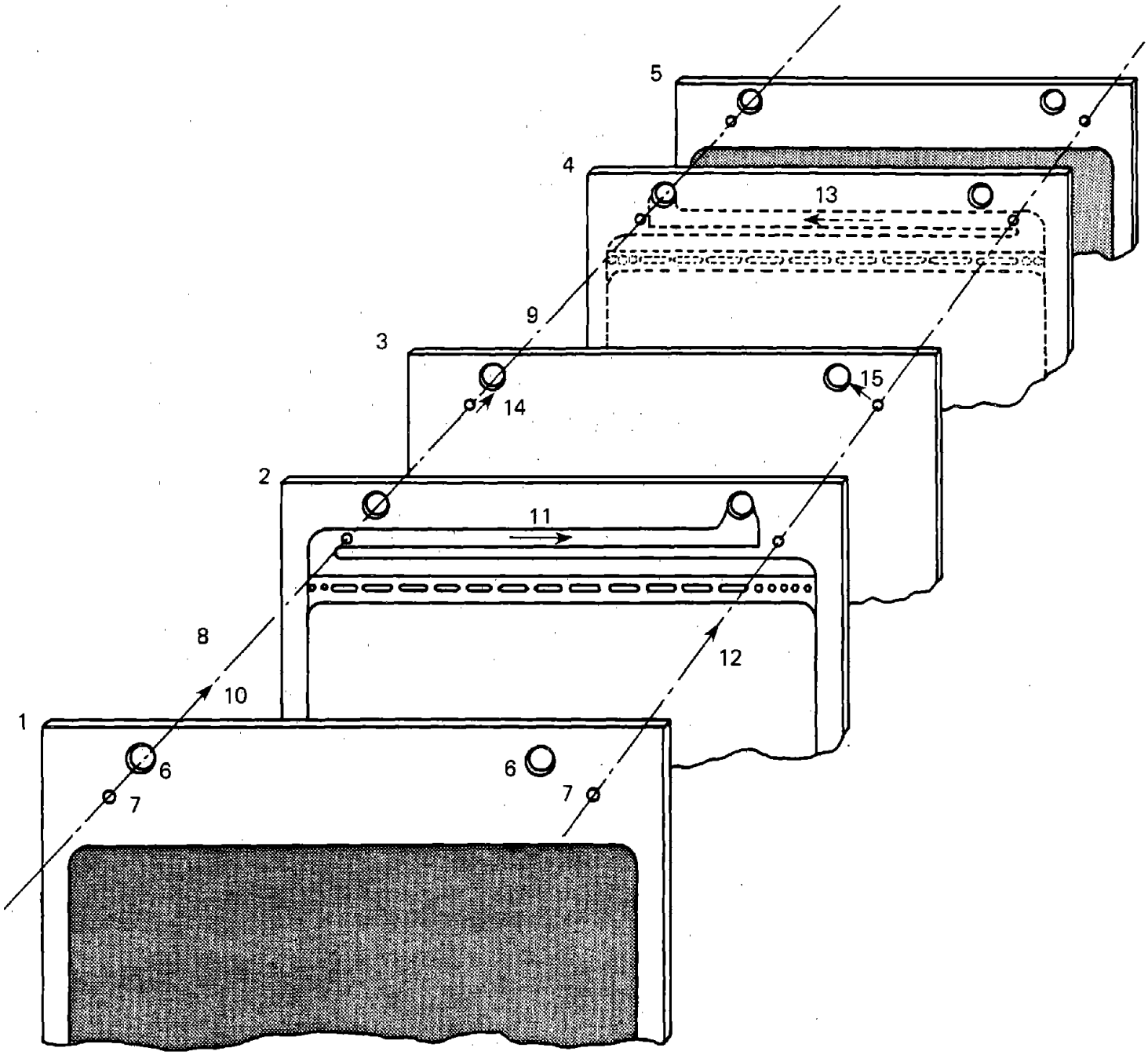

1,5 BIPOLAR ELECTRODES
2 ANOLYTE FLOW FRAME
3 MICROPOROUS SEPARATOR
4 CATHOLYTE FLOW FRAME
6 MANIFOLD HOLES
7 TUNNEL HOLES
8 ANODE COMPARTMENT
9 CATHODE COMPARTMENT
10,12 TUNNEL CURRENTS
11,13 CHANNEL CURRENTS
14,15 MEMBRANE CURRENTS

Figure IV-7 Unit Cell From "Tunnel" Protection Experiment

the microporous separator, however, is difficult to measure, predict, or change with different SOC's of the electrolyte. The present components are fabricated with old compression molding technology and have low dimensional tolerance. Such a rebuilding, while instructive, would not greatly add to the knowledge of shunt current protection in our most recent cell designs.

The experiment showed the general feasibility of shunt current protection with tunnel protective currents at significantly lower input current values than manifold protection. Although the absolute results are flawed by component problems, sufficient data was gained to redesign components, i.e. flow frames around a microporous insert would eliminate the microporous pathway from the tunnel to the manifold and allow appropriate design. This will be used in future experiments.

IV.3 Component Life Studies

The cost basis for comparing photovoltaic storage batteries is a twenty year cycle life. This life cycle cost includes initial battery cost as well as maintenance and system replacements when necessary. While a total 20 year life for a single system is not necessary, life must be acceptably long to require a minimum number of system replacements and still meet the 20 year cost goal. For example, five to ten year lifetimes are equivalent to 1500-3500 daily cycles or perhaps 500-2000 deep cycles. Time and manpower requirements have prevented total systems from being tested for these lifetimes during Phase I. However, various component studies were initiated in order to evaluate possible component weaknesses that could limit system life. So far, no clearly unavoidable life limiting mechanism has been identified, although electrolyte invariance, particularly pH, may require periodic maintenance. These component studies, plus the accomplished cycling of the X-3 to 100 plus cycles and the X-10 to 50 plus cycles, indicate that 500 cycles life should easily be obtained and thousands of cycles are likely with little or no maintenance. In fact, without a clearly defined life limit, extremely long cycle life is a distinct possibility, especially since the zinc-bromine electrodes are immune from long term problems such as shape change and solid state structural modifications.

IV.3.1 Carbon Plastic Oxidation Under Potentiostatic Conditions

The stability of carbon plastic electrode material at oxidative potentials was studied in an effort to estimate possible lifetimes in bromine containing environments. Initial cycling of carbon plastic electrodes in both monopolar and bipolar designs had shown no resistivity changes during 50-100 deep cycle tests, and stack autopsies had shown no signs of oxidative degradation. The potentiostatic oxidation method was used in order to quantitatively measure the oxidation rate of carbon plastic. This testing showed that the Faradaic oxidation rate of carbon plastic rapidly drops to almost negligible values.

Technique - The experimental apparatus shown in Figure IV-8 uses a strip of carbon plastic potentiostated relative to a combined zinc reference and counter-electrode in solutions of 3 M zinc halides. The electrolytes were sparged with N_2. Several papers from United Technologies Corporation (11, 12, 13) describe similar carbon oxidation and measurement techniques in high temperature (160°C) phosphoric acid cells. Such studies show good correlations between oxidative currents (while holding the carbon at high potentials) and CO_2 evolution. The initial coulombic oxidation, however, is more likely to oxidize various redox groups in the carbon. Studies on the conductive carbon, Vulcan XC-72, show that most oxidation occurs in the amorphous carbon material at the particle centers. The highly graphitized material near the surface of the Vulcan particles is relatively immune to oxidative attack. Therefore, high oxidation levels are required before Vulcan mixtures lose conductivity.

Results - Table IV-2 shows the results of these oxidative studies.

Initial experiments potentiostated typical carbon plastic near the bromine potential in standard solution. Carbon oxidation is accelerated by increasing temperature and potential vs. a zinc reference. There are many difficulties in running and interpreting these first experiments. Direct collection of CO_2 would require very long experimental times at these oxidation rates. Initial coulombic oxidation rates fall rapidly during the first day of immersion, presumably because of the charging of surface redox groups. Most important, the presence or evolution of Br_2 can seriously affect the results. At typical open-circuit voltages in standard solution, any currents would reflect the Br^-/Br_2 electrode. The oxidative currents at 1700 mV vs. Zn are too high because of Br_2 evolution. The initial solution contains no Br_2, but the equilibrium Br_2 at 1700 mV is about .002 M. If all the oxidative current at 1700 mV produced Br_2, it would require over a year for the cell to reach .002 M Br_2! The data at 1500 and 1600 mV are not flawed by this problem.

Extrapolating the 1500 mV and 1600 mV data via a Tafel activation model to 1750 mV predicts an oxidative current of 6.8×10^{-9} Amp/cm^2. The energy of activation is about 10.4 Kcal/mole at these potentials. For cells operating at temperatures of about 31°C, the extrapolated current 6.8×10^{-9} Amp/cm^2 oxidizing 30 mil carbon plastic to CO_2 represents .015%/year. Assuming that the interior of a conductive carbon particle is oxidized, even 5% oxidation should be tolerable. This represents a useful life of 336 years.

Because of possible ambiguity with Br_2 evolution at potentials approaching the OCV of the Zn/Br_2 battery, further studies were conducted using 3 M $ZnCl_2$, which has no measurable Cl_2 evolution at 1750 mV vs Zn. All of this data was obtained after 3 days of oxidation, after which the oxidation rate was stable, i.e., dropped less than 10%/day. Some individual points seem anomolous, although a clear pattern exists.

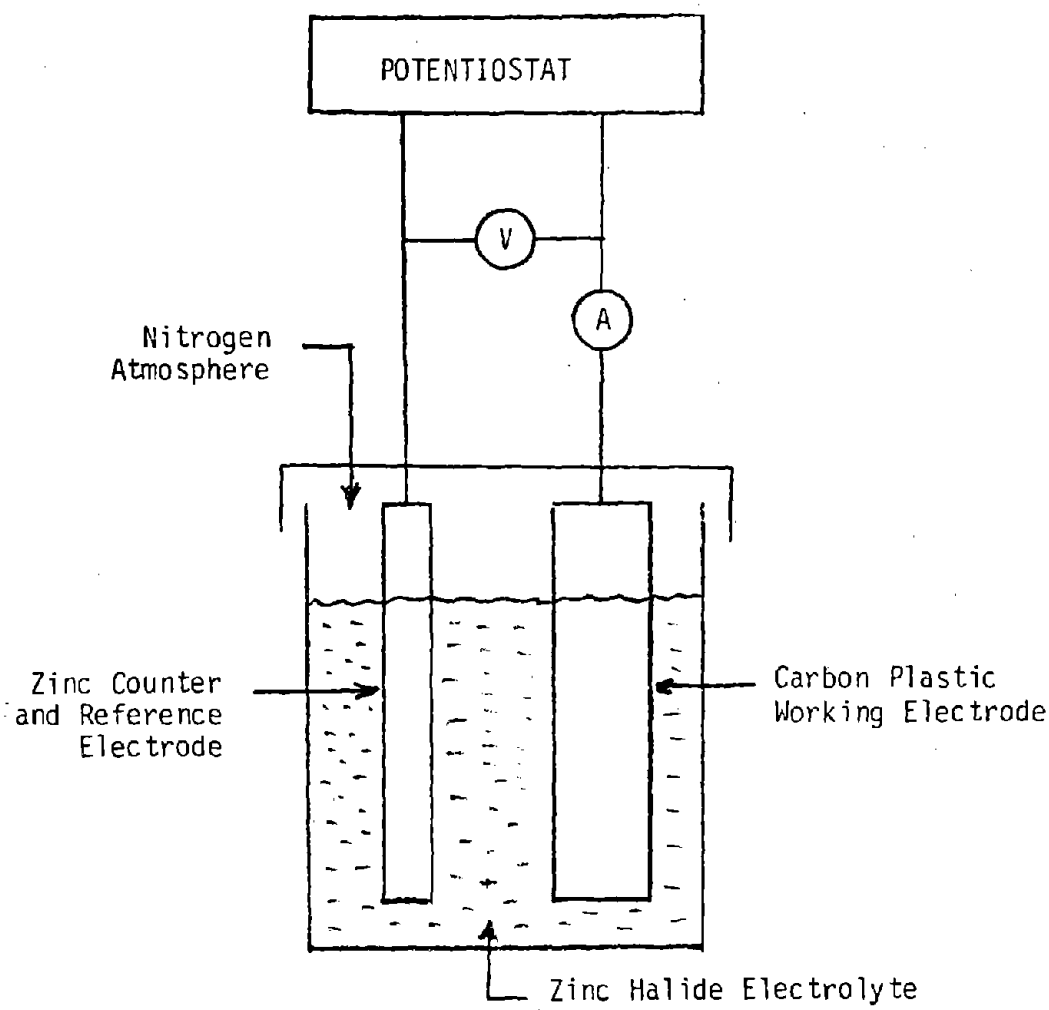

Figure IV-8 Potentiostatic Oxidation of Carbon Plastic

TABLE IV-2

OXIDATION RATES OF CARBON PLASTIC VS. POTENTIAL

Electrode	Electrolyte	Temperature °C	Oxidation Currents ($A/cm^2 \times 10^{-9}$) vs Potential (mV/Zn)				
			1500	1600	1700	1750	
Extruded Carbon Plastic	3 M $ZnBr_2$ 1 M MEMBr 0.2 M $ZnSO_4$	31	.64	1.65	9.7	--	
		57	2.4	6.7	67	--	
Extruded Carbon Plastic	3 M $ZnCl_2$	34	--	28	30	34	
		55	--	24	35	52	
Sanded Carbon Plastic	3 M $ZnCl_2$	34	--	40	30	73	
		56	--	25	30	440	
PV-1 + Carbon Plastic	3 M $ZnCl_2$	34	--	2900	4040	11000	
		53	--	6140	6000	25000	

Comparison of the $ZnCl_2$ data with the standard solution data at 1600 mV vs Zn shows that $ZnCl_2$ seems to promote the oxidation more than $ZnBr_2$ and that the effect of temperature is less severe with $ZnCl_2$.

A series of carbon plastic samples were lightly sanded with emery paper to remove the possibility that a surface plastic layer was insulating most of the carbon plastic from oxidation. The data for sanded plastic (Table IV-2) show no significant increase in oxidation rate.

Next, a cathode with a typical cathode catalytic layer on one side was tested. The catalytic layer increases the oxidation rate by at least 100-fold, although at 34 C and 1750 mV vs Zn, this current is still only a few $\mu A/cm^2$ and would probably be less in $ZnBr_2$. The high oxidation rate of high-surface area carbon has been reported by Kinoshita for fuel cells (13). The carbon used in the cathode layer has a large surface area. This complete area is probably not necessary for Br_2 kinetics, but its many surface groups could oxidize rapidly. Separate long-term testing of the cathode catalyst layer (Section IV.2.2) showed stable operation throughout 5 months. Therefore, the higher measured oxidation rates of the cathode layer may have been part of a long term transient which would have fallen off with extended potentiostatic testing. More work is planned in this area.

IV.3.2 Cathode Catalyst

A high surface area carbon layer (PV-1) is applied to the cathode side of the bipolar carbon plastic electrode. This layer catalytically activates bromine's Faradaic reactivity, particularly the reduction of Br_2 during discharge. Previous oxidation studies, (see above), have shown high Faradaic oxidation rates on these catalytic layers. Therefore, long term activity studies were begun. These studies showed negligible changes in electrode polarization. The studies were prematurely ended by a pump failure.

Technique - The experimental apparatus utilized a flow cell model composed of two 100 cm^2 cathode current collectors. Electrolyte, approximating catholyte at 50% SOC, was circulated between two electrodes which were separated by only a single Vexar screen. The electrolyte generally flowed downward to prevent build-up of Br_2 complex in the cell, except for occasional flow reversals to remove entrapped gas. The electrolyte was circulated in a closed loop between the reservoir and cell using a small centrifugal pump with a magnetic drive. Current was continuously passed through the cell at 20 mA/cm^2, causing oxidation and reduction of Br^-/Br_2 at the two electrodes. Polarity of the current was changed at 2 to 4 week intervals over a five month period.

Results - Initial voltage across the cell was 0.104 V and, was 0.211 V on terminating the test. The total cell voltage includes any electrode overvoltages, plus internal electrolyte resistance between the cells. During the experiment, approximately 60% of the original Br_2 escaped from the system. This would increase the resistivity of the electrolyte as more quaternary ammonium was extracted back into the aqueous - phase, and could explain the increase in cell voltage.

The experiment was discontinued when the magnetic drive of the pump became disengaged. Electrolyte then drained out of the cell and back into the reservoir. Current continued to pass through any electrolyte still remaining in the cell. A localized hot spot developed, charring and warping both electrodes, precluding reassembly of the stack.

IV.3.3 Bromine Complex

At the conclusion of the cathode study mentioned above, the remaining "bromine oil" in the reservoir was analyzed via proton NMR techniques using Br_2 as "solvent" for quaternary ammonium bromide. A "normal" NMR trace for MEMBr was observed with no new peaks which would be indicative of either bromination or other degradation of the amine. Similar studies at the end of battery cycling have also shown no degradation of the amine.

IV.3.4 Electrolyte pH

Battery cycling during early Phase I showed significant improvements in pH stability of the electrolyte (maintaining values of 2.5-3.5), with X-3A reaching 100 plus cycles of operation with stable pH. However, much of the earlier testing of the zinc-bromine system prior to Phase I, showed steady pH increases during the initial 20 to 40 cycles. As pH rises above 4.0, plating tends to become mossy, and coulombic efficiency inexplicably drops. Further pH increases cause a colloidal precipitation of zinc oxides/hydroxides. This precipitate increases system pressure drops and quickly causes electrolyte distribution problems. Fortunately, small additions of HBr quickly reduce the pH and dissolve the precipitate. However, repeated HBr additions are eventually required. Two mechanisms of pH increase have been identified (see below). Both mechanisms seem easily controllable, so that the need for HBr addition should be reduced or eliminated.

Mechanisms Causing pH Increases

H_2 Mechanism

$$2H_2O + Zn^0 \rightarrow Zn^{++} + H_2 + 2OH^-$$

O_2 Mechanism

$$O_2 + 2\ Zn \rightarrow 2\ ZnO$$

$$ZnO + H_2O \rightarrow Zn^{++} + 2\ OH^-$$

Hydrogen Evolution - Hydrogen evolution was the obvious candidate for pH increases by the mechanism shown below. Hydrogen bubbles can be seen forming on the surface of Zn in Zn/Br_2 solutions and gas bubbles can be observed in the anolyte as it leaves the stack. However, the amount of gassing generally observed is usually quite small and can account for only a small fraction of the observed pH changes. The only exception is when specific impurities enter the electrolyte and act to catalyze H_2 evolution at the anode. For example, Pt sensor tabs at the cathode of X-10 (Section III.2) slowly corroded so that after 30 cycles, H_2 was being evolved fast enough to significantly increase the internal resistance of the battery. Fortunately, Pt sensors are not necessary and in future designs will be eliminated or replaced by Ta sensors at the anode.

The pH increase from H_2 evolution can be controlled by passive recombination of H_2 with Br_2 to form HBr as described in Section IV.4. Furthermore, if the electrolyte does become contaminated, it can be treated to remove impurities such as Fe, Ni, and Pt which catalyze H_2 evolution.

Oxygen Infiltration - Oxygen appears to be the primary source of pH increases particularly during the cycling, prior to Phase I. The mechanism of pH increase by oxygen infiltration shown above is that it dissolves in the electrolyte where it can react non-Faradaically with Zn, followed by hydrolysis to generate hydroxyl ions. The oxygen mechanism was inadvertently discovered when the observed small quantities of H_2 failed to explain the magnitude of pH increases. By checking experimental logs, it was confirmed that frequently inspected reservoirs (direct exposure to air) and loose plastic fittings (aspiration of air into the electrolyte) correlated well with unusually fast pH increases. In vitro experiments quickly showed that electrolyte in contact with zinc powder showed stable pH under N_2, but rapidly increasing pH when exposed to air.

Since that observation, several batteries have passed 100 cycles without needing HBr additions. This improved stability is attributed to cycling large systems (fewer points for air infiltration) with start-up under N_2 atmosphere in the reservoirs, and achievement of tighter plumbing by using solvent welded PVC fittings, rather than compression plastic fittings that loosen with time. Hydrobromic acid addition still provides a quick fix for any long term pH increases and could be added automatically by a system microprocessor controller.

IV.3.5 Zinc Cycling

Discharge Potential of Zinc on Carbon Plastic Electrodes at Low Loadings

The discharge potential of zinc on carbon plastic electrodes falls off dramatically at low loadings of zinc. The effect is enhanced at higher current densities. The effect is not seen with zinc on zinc electrodes.

A carbon plastic electrode (16 cm^2) was placed counter to a large zinc foil, (60 cm^2) separated by 2 cm. The cell compartment was filled with standard electrolyte, 3M $ZnBr_2$, 1 M MEM^+ Br^- and 0.2 M $ZnSO_4$, only. Luggin capillaries with calomel (SCE) electrode reference were placed at or near each electrode. Provisions were made to record the half-cell potentials of the carbon plastic electrode, the zinc foil electrode, and the total cell potential. The total coulombs passed through the system were also recorded.

The potential of the carbon plastic electrode at the beginning of each discharge was essentially constant for all cycles. However, the potential of the carbon-plastic electrode vs. the calomel electrode at the end of a 200-second discharge was greatly dependent upon the zinc loading (Figure IV-9a). Even at an apparent loading of 7 mAh/cm^2, there was a sloping discharge curve; 50 mV/200 sec in contrast to a flat curve for zinc-on-zinc. With low loadings, i.e., 1 mAh/cm^2, the end of discharge potential was near that of bromine evolution.

The current levels for charge/discharge were then changed to 80 coulombs charge, and 95 coulombs discharge, respectively, to reduce the zinc loading (25 and 29.7 mA/cm^2). The end of discharge voltage decreased as the zinc loading diminished (Figure IV-9b). The carbon-plastic electrode surface was initially loaded to 1.51 mAh/cm^2, 87 coulombs. The system was discharged for 200 seconds, passing 30 coulombs of oxidative current. Then it was charged for 200 sec, passing 40 coulombs of reductive current. After a few cycles, the order was changed to 90 coulombs reductive and 60 coulombs oxidative current (28 and 18 mA/cm^2).

After 13 cycles (86.6 minutes), the total zinc loading had increased to 7.82 mAh/cm^2. The potential of the zinc foil electrode was constant during charge and discharge at any loading level. The potential difference between charge and discharge was about 35 millivolts, and the potential was square wave.

When the apparent loading was less than 3 mAh/cm^2 (at the beginning of discharge), the potential at the end of a 200 second discharge fell to a plateau of about plus 100 mV vs. SCE. During 18 additional cycles (2 hours), the zinc loading was slowly reduced to 1.7 mAh/cm^2.

The cycle was changed to 120 coulombs charge, 60 coulombs discharge (18.75 and 37.5 mA/cm^2), to rebuild the zinc loading. The end of discharge potential traced the previous zinc build-up curve at 18 mA/cm^2 discharge. After 12 more cycles (80 minutes), the apparent zinc loading had built up to 11.37 mAh/cm^2. The charge/discharge coulombs were changed to 120 each (37.5 mA/cm^2) for 4 more cycles. The end-of-discharge voltage was then constant at .85 volts vs. SCE). The discharge curve slope was 70 mV/200 sec.

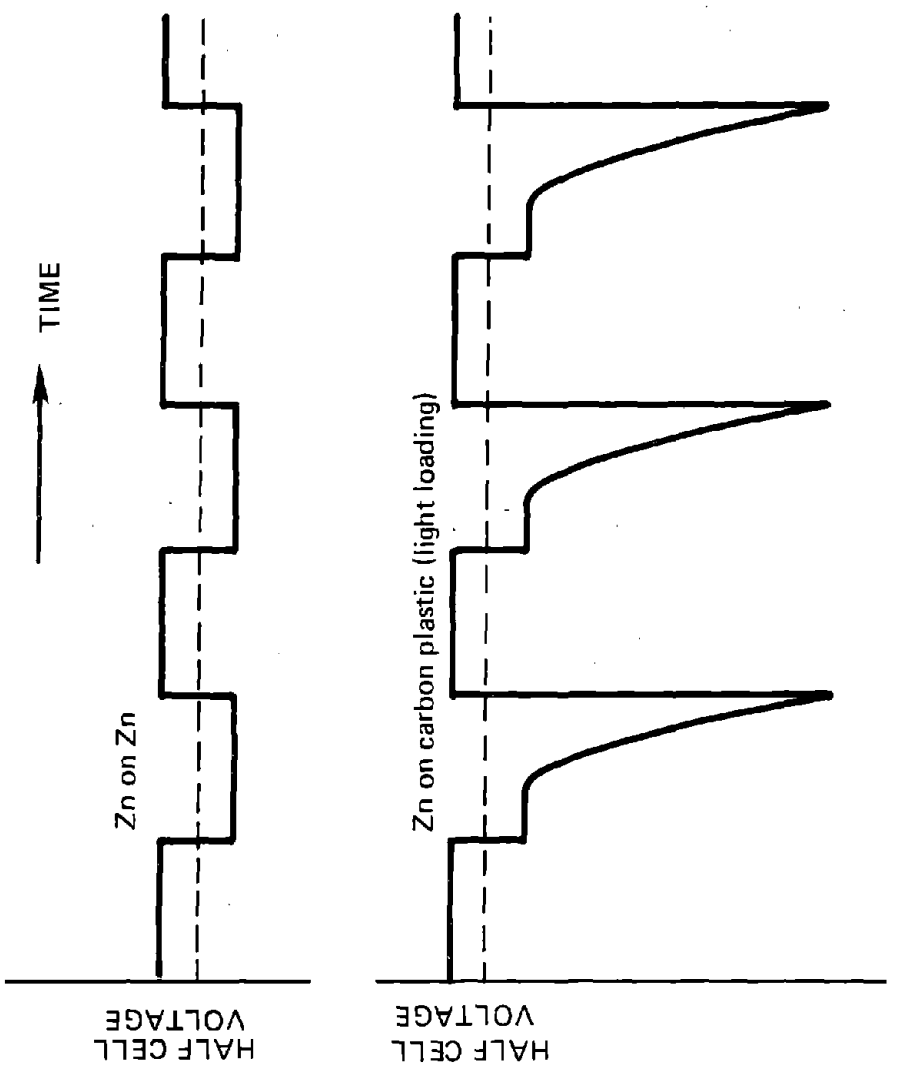

Figure IV-9a Discharge of Zinc on Carbon Plastic

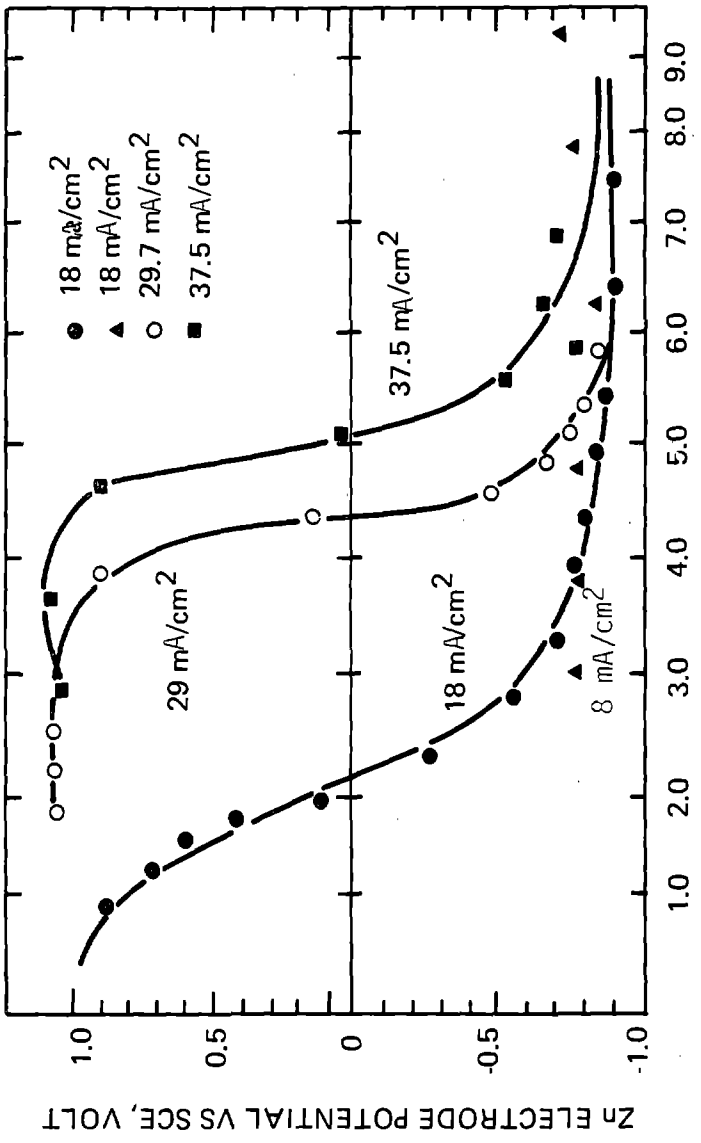

Figure IV-9b Zinc Plate Thickness (mAh/cm^2) on Carbon Plastic

The cycle was then changed to slowly strip off the zinc loading at 37.5 mA/cm^2 (120 coulombs discharge 90 coulombs charge). When the apparent loading had decreased to between 4 to 5 mAh/cm^2, the end of discharge potential had fallen to more than 1 volt vs. SCE (some IR included). The cycling was continued at this rate to a total of 67 cycles (7.5 hours), after which the coulomb count total was reduced to 2.6. However, the start of zinc discharge potential remained essentially constant during the last 20 cycles. Based upon the potential at the beginning of discharge, the system behaved as if it were a zinc electrode.

In the experiment, over 5 million total coulombs put on the carbon plastic electrode were essentially all recovered. There was no apparent loss due to H_2 formation and escape. It would appear that at zinc loadings below 10 mAh/cm^2 the zinc-on-carbon plastic electrode does not behave as a zinc electrode. At loadings below 5-6 mAh/cm^2, the sloping of discharge curve becomes very significant and the end of discharge potential can be very low. The loading level before the effect becomes significant is a sharp function of current density; thus, final discharge of the zinc bromine battery at ever decreasing current densities allows a high coulombic efficiency (to a fixed cut off voltage).

IV.3.6 Plastic Compatibility in Bromine Containing Electrolytes

Prior to the start of the Phase I contract a considerable amount of material screening had been accomplished. Literature sources and simple short term bromine compatability tests eliminated most metals except Ti, Ta, and various carbons. In the case of plastics an early decision was made, that, if possible, only cheap commercially available plastics would be utilized. Also, it was desired that the plastic already be available in its end use form, i.e., pipes, valves, tanks, or as pellets suitable for mass processing such as extrusion or injection molding. Again, through literature sources and simple screening tests, the decision was made to concentrate on polyolefins, PVC, and, where necessary, fluorinated materials such as Teflon.

To test the compatability of each of the plastics under consideration, test samples were placed in electrolyte and monitored over the course of several months. These samples included carbon plastic electrode material, various structural plastics, and Daramic separators. For each material, four 1.5 in^2 samples were cut and carefully weighed. Three of the samples were tested and one was held back as a control. The triplicate samples were placed in individual glass jars which had Teflon liners on the lids. The electrolyte added was prepared by charging a battery to a 50% state-of-charge (SOC) and then utilizing equal volumes of catholyte aqueous and Br_2 containing oil phases. These samples were then placed in an environmental chamber, (Figure IV-10) which was thermostated at 55^{o}C.

Physical appearance of each sample was monitored on a monthly basis without opening any of the jars. At the end of three months one

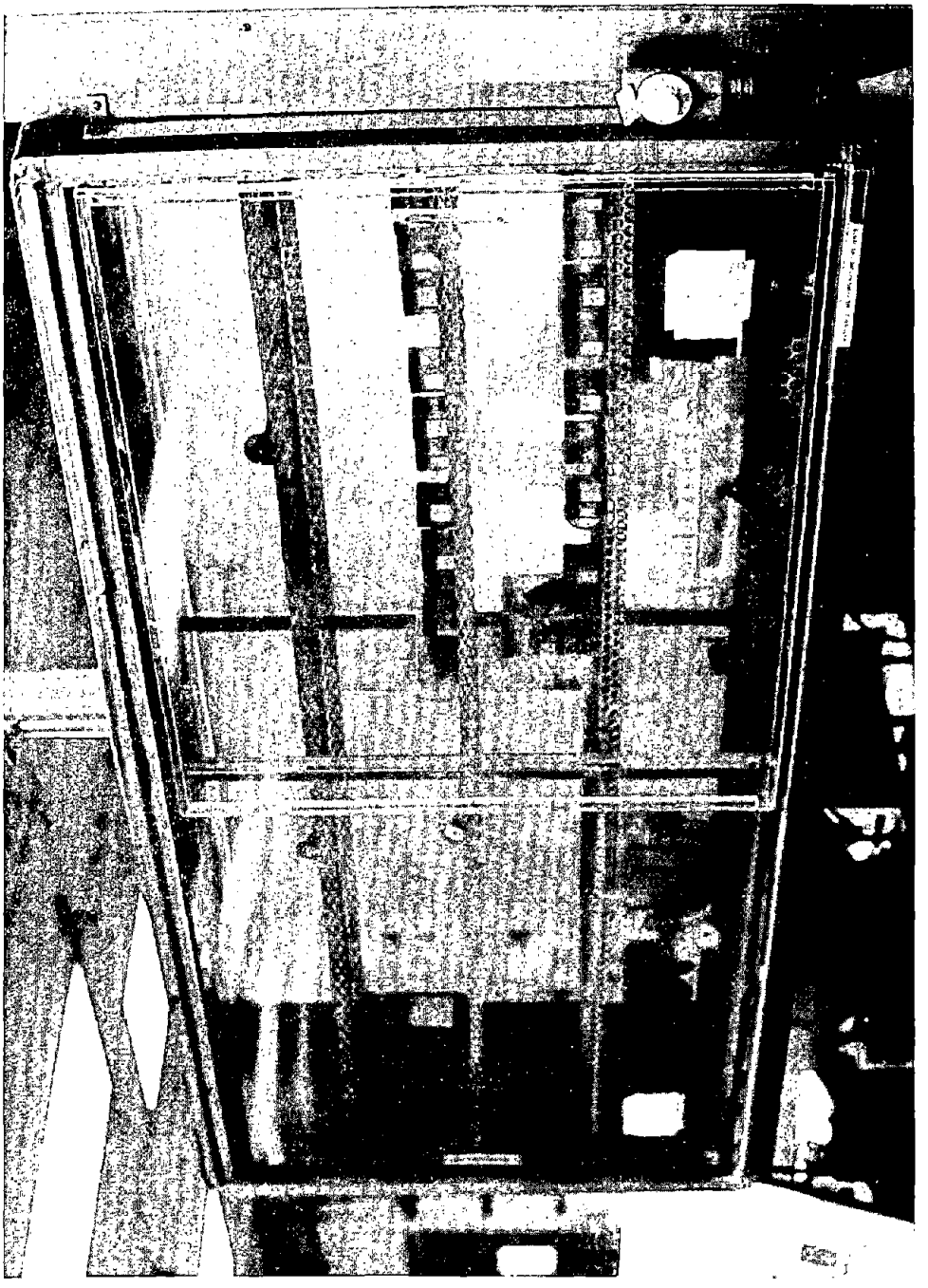

Figure IV-10 Environmental Chamber for Testing Plastics

of each of the triplicate samples was removed for more careful examination. Weight gain measurements were also made after the sample had been water washed and vacuum dried to a constant weight (±2 mg) over a minimum four hour period. For some samples, only nine month weight data are available.

The physical appearance of these samples was identical to that observed when using them in batteries. All of the transparent or filled samples quickly showed a bromine discoloration. When samples were removed and subsequently broken in two, this coloration was found throughout but with decreasing intensity farther from the surface, as expected. After three months all samples except Daramic were less resilient. These were the only observable changes, and were no different after twelve months.

Weight gains are given in Table IV-3. In general, the same percentage weight gain was found for each duplicate sample after 3 and 12 months (the third sample remains on test), indicating that the Br_2 uptake at this temperature all happens in the first three months.

Future studies will include more of these static tests, shorter term kinetics studies and an attempt to determine if the Br_2 uptake is due to absorption or reduction. Tests will also include the continued autopsies of batteries. It should be noted that in using these materials we have not observed any battery failure attributed to failure of its materials of construction.

IV.3.7 Pumps

The pumps used for electrolyte flow are commercially available AC centrifugal pumps with magnetic drives. Typically, these were changed to DC motors to facilitate experimentation with varying flow rates. Individual pumps have had nearly continuous usage for well over a year without failure. Longer test times have not been available since we only recently moved to 600 cm^2 size batteries. We have evidenced no material degradation within the pump heads. The only pump related problem has been occasionally misaligned shafts on incoming pumps which, if not corrected, can lead to premature motor failures. To date it is anticipated that pump life will be the same as found in other similar applications and that there will not be problems peculiar to Zn/Br_2.

Earlier testing with 100 cm^2 electrodes prior to Phase I, had depended on peristaltic pumps with flexible Viton tubing. Wear of the tubing required monthly replacement of the Viton and several battery cycling studies were interrupted when electrolyte leaked from slits in the Viton. These peristaltic pumps have been totally replaced by centrifugal pumps, because of safety, reliability and higher volumetric capacity.

Table IV-3

Bromine Absorption by Various Plastics

	Sample	3 Months Wt. Gain (mg)	3 Months Wt. Gain (%)	12 Months Wt. Gain (mg)	12 Months Wt. Gain (%)
1.	24-mil - Extruded carbon plastic	66	9	45	6
2.	Same as #1 - but more carbon	245	14	336	19
3.	Same as #2 - but with additive	186	13	318	21
4.	Same as #2 - but more carbon	206	18	113	9
5.	Same as #3 - but more carbon	370	12	241	13
6.	Same as #5 - but more carbon	213	18	190	16
7.	Polyolefin	274	39	249	35
8.	Polypropylene filled polyolefin-1	118	12	148	16
9.	Filled polyolefin-2			197	12
10.	Filled polyolefin-3			204	12
11.	20% Talc Polypropylene* Filled polyolefin-4			99	13
12.	Daramic with Oil	226	93	(170)	(8)
13.	Daramic without Oil	105	47	57	28

*9 Month Data

IV.4 Hydrogen-Bromine Recombination

Hydrogen Production

Small quantities of hydrogen are produced during operation of the zinc-bromine battery. The effect of this on capacity of the battery is very small, and hydrogen production is merely a nuisance problem in any given battery. In battery systems such as lead-acid, the hyrogen is vented and water is added to replace it.

In a circulating electrolyte zinc-bromine battery, long term effects of hydrogen production are of some greater concern. Prolonged hydrogen production leads to pH changes in the electrolyte. Simplistically, the production of hydrogen in the battery can be viewed as due to a reaction of zinc with water:

$$Zn + 2H_2O \rightarrow Zn^{+2} + H_2 + 2OH^-$$

Thus, the pH of the electrolyte is increased by the hydrogen prodution process, and can lead eventually to precipitation of zinc as oxide, hydroxide, and oxyhalide.

Recombination

The consumption of zinc by reaction with water leaves behind an equivalent amount of excess bromine in the charged zinc bromine battery. Recombination of the hydrogen produced with this bromine will yield hydrobromic acid, and neutralize the hydroxyl ions produced in the hydrogen production as follows:

$$Zn + 2H_2O \rightarrow Zn^{++} + 2OH^- + H_2$$

$$H_2 + Br_2 \rightarrow 2H^+ + 2\ Br^-$$

$$2H^+ + 2OH^- \rightarrow 2H_2O$$

The summation reaction is:

$$Zn + Br_2 + 2H_2O \rightarrow Zn{+}{+} + 2Br^- + 2H_2O$$

Thus, the net effect of recombination would be a small loss of capacity equivalent to the hydrogen produced. The electrolyte pH, however, would be invariant. Hydrogen produced in the zinc-bromine battery is swept from cells by the flowing electrolytes and carried into the reservoir headspaces. Therefore, the obvious location for hydrogen recombination is in the reservoirs.

Gas Phase Recombination

Hydrogen and bromine can be combined catalytically. The free energy of the gas phase reaction:

$$H_2 + Br_2 \rightarrow 2HBr$$

is -46 KCal at 25°C. The catalyst can be chosen from noble metals, i.e. Pt, unsupported or supported on conductive substrates such as carbon, or nonconductive substrates such as alumina.

Experimentally, catalysts were suspended over 100 ml of synthetically prepared "50% SOC" electrolyte (1.5 M $ZnBr_2$, 0.25 M MEMBr, 0.25M Q-14 and 1 M Br_2) in 250 ml flasks. The gas space was purged with hydrogen and a vacuum gauge was attached to the flask. The pressure decreased as the hydrogen reacted with bromine, and the HBr formed dissolved in the aqueous phase.

The location of the catalyst in the system influences the reaction rate. The hydrogen and bromine in the gas phase at or above the catalyst react rapidly. The reaction rate then slows and is dependent upon the slow diffusion of bromine vapor upward from the gas/liquid interface to the catalyst.

Interfacial Recombination

Placing the catalyst partially in the gas phase and partially in the electrolyte, allows a H_2/Br_2 fuel cell type reaction. In this case, hydrogen from the gas phase reacts anodically at the meniscus (gas/liquid/solid interface) producing protons and releasing electrons to the catalyst and the conductive substrate (carbon). These electrons are plassed into the liquid/solid interface region where bromine in the electrolyte is reduced to bromide ions. The migration of these ions together with proton migration into the electrolyte completes the circuit.

In experiments similar to the above description, Pt black catalyst was lowered partially into a 50% SOC aqueous electrolyte. The pressure decreased as the hydrogen reacted with the bromine. However, when the platinum catalyst was in contact with both aqueous and bromine complex phases, the pressure did not decrease and the platinum black in contact with the bromine complex phase was chemically/electrochemically attacked.

Earlier, in another set of experiments, cathode activation layer (PV-1) coated carbon plastic strips were partially submerged in 50% SOC electrolytes and streams of 7% H_2 in 93% He (for safety) were passed over the solutions (the gas streams were preconditioned by first passing over 50% SOC electrolytes). The aqueous phase colors changed from orange/yellow to light yellow and the pH of the aqueous phase decreased, indicating an increase in protons. However, under these flow conditions, the pressure decrease was minimal.

Thus, we have demonstrated that hydrogen can be recombined with bromine catalytically in the gas phase, or electrocatalytically at a gas/liquid (containing bromine) interface. More work is needed to define optimum recombination conditions and to determine hydrogen production levels in engineered systems.

IV.5 Electrolyte Flow Distribution in Stacks

Electrochemical reactions, whether they are batteries, fuel cells or electrolyzers, are frequently designed with circulating electrolytes. Electrolyte circulation can improve performance by adding reactants, removing products, enhancing mass transfer, and assisting thermal management. Circulation offers all of these advantages in the zinc-bromine battery and, in particular, improves zinc plating with the avoidance of shape change or dendrites.

Flow maldistribution can be a problem, however. Most circulating electrolyte designs assume a uniform flow over the electrode face, but factors in the manifold, flow frame and electrode spacers can cause regions of weak circulation or even "dead spots". When the flow stagnates, the benefits of circulation disappear and conditions may arise which lead to decreased life. Sometimes higher flow rates can supply more circulation to "dead spots", but this requires higher pressure drops and larger consumption of auxiliary pump power. Controlling pressure drops can occur in exterior plumbing, common manifolds, manifold branches or on individual flow frames, depending on the design. Modification of controlling pressure drops can sometimes, but not always, improve flow distribution. Studies of the manifold and flow manifold have provided new insights on factors which encourage maldistribution, and new pressure drop vs. flow rate studies are underway, the results of which will be valuable in final system optimizations.

IV.5.1 Flow Frame Studies

A typical zinc-bromine battery flow frame is shown in Figure IV-11. Electrolyte enters in the upper right corner from a common manifold, down a manifold branch, distributes horizontally across the flow frames, flows down through a matrix of electrode supports (i.e., Vexar screen - not shown), into the lower horizontal distributor, across to the lower manifold branch and finally back into the lower left common manifold. Common manifolds in the opposite face feed the other electrolyte stream to an identical flow frame on the other side of the bipolar electrode.

Experimental flow frame apparatus made use of a single flow frame held between clear plexiglas plates. Appropriate plumbing connections supplied electrolyte at controlled flow rates. Dye tracers were used to record flow distribution by tracing the dye front every 5 seconds with a wax pencil directly on the plexiglas windows. For typical flow rates the flow frame was traversed in 15 to 30 seconds, so that each dye injection showed 3 to 6 progressive fronts. At these flow rates, pressure drops were small relative to those anticipated in the manifold.

Flow studies with Vexar screens generally showed uniform progress of the front with no general dead spots. However, in some grades of Vexar, the cross weave intersection is not at right angles and can

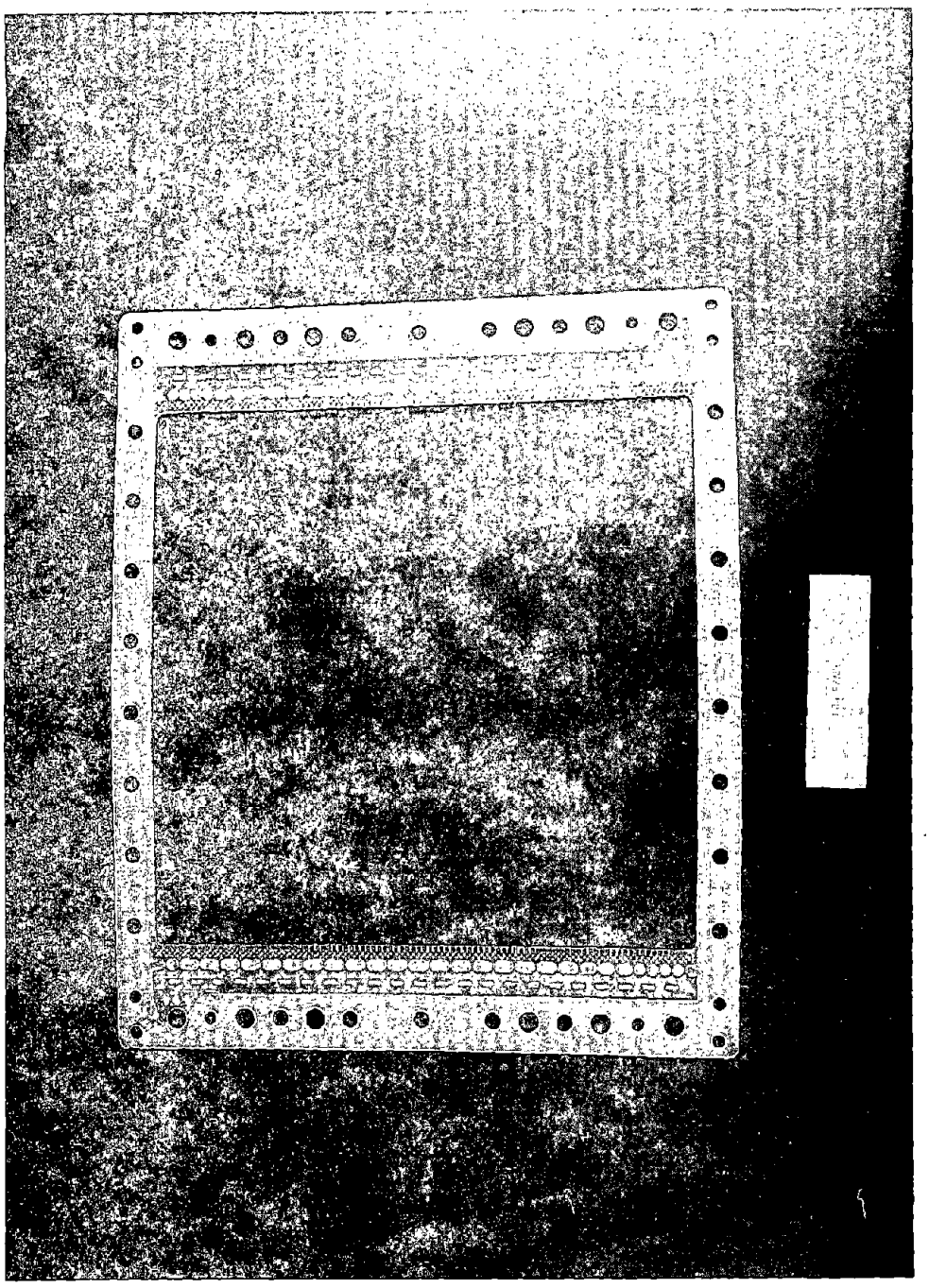

Figure IV-11 Zinc-Bromine Battery Flow Frame

approach 75°. If this diagonal bias of the Vexar favors the diagonal bias between the two common manifolds, the electrolyte tends to short curcuit, leaving dead spots as shown in Figure IV-12b. The opposite diagonal bias (Figure IV-12a) gives uniform distribution. Therefore, this "short circuit bias" can be avoided during stack assembly. Another observation with Vexar was higher flow at the edge of electrodes beyond the edges of the Vexar. Conversely, when the Vexar touched the edge of the electrode, a dead spot was produced. Again, this detail can be controlled during assembly. The most significant observation, however, was that large gas bubbles have trouble being removed from the Vexar matrix, even with surfactants. The horizontal portions of the Vexar act as gas traps. These trapped gas bubbles act as points of stagnation. Early program autopsies, after high pH excursions and/or unusual gassing, showed nodular zinc growth around what had been gas bubbles. The elimination of these horizontal traps seems very desirable.

Incorporating electrode spacers onto the separator has the advantages of removing horizontal gas traps as well as reducing part count. Both "ribbed" or "posted" designs have been considered (See Section III.4.3). Posts were favored because they offer the minimum reduction in electrode cross-sectional area, and therefore, has least increase in internal resistance. No gas bubbles are retained using these "posted" electrode spacers. Dye tracer flow frame studies with posts showed a tendency to short circuit flow, leaving dead spots as shown in Figure IV-13. As a result, the flow frame horizontal distributor was modified to the present design in order to eliminate these dead spots. Dye tracer studies on these improved flow frames are also indicated in Figure IV-13.

Ribbed electrode spacers show little gas retention and no tendency for short circuited flow. Except for the reduced electrode cross-section, "ribbed" and "posted" supports are both attractive substitutes for Vexar.

IV.5.2 Manifold

With manifold shunt current protection, the diameter of the common manifold should be as small as possible in order to reduce the magnitude of the protective current. However, small manifold diameters cause the pressure drop to increase, and also can lead to electrolyte maldistribution. Therefore, one must optimize the diameter in terms of these opposing considerations. Tunnel shunt current protection will decouple these design considerations (Section I.3), but a knowledge of manifold pressure drops is still useful.

A simulated manifold was constructed to empirically study manifold flow. This apparatus, a stack of plexiglass sheets, is shown in Figure IV-14. The stack consisted of two alternating sheets, one with two 3/8" holes and the second with the same two holes and an interconnecting

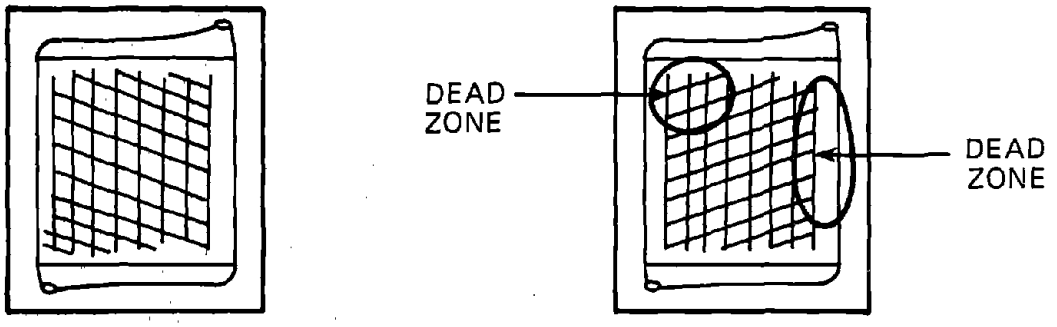

Figure IV-12 Vexar Bias Relative to Flow Frame Manifolding

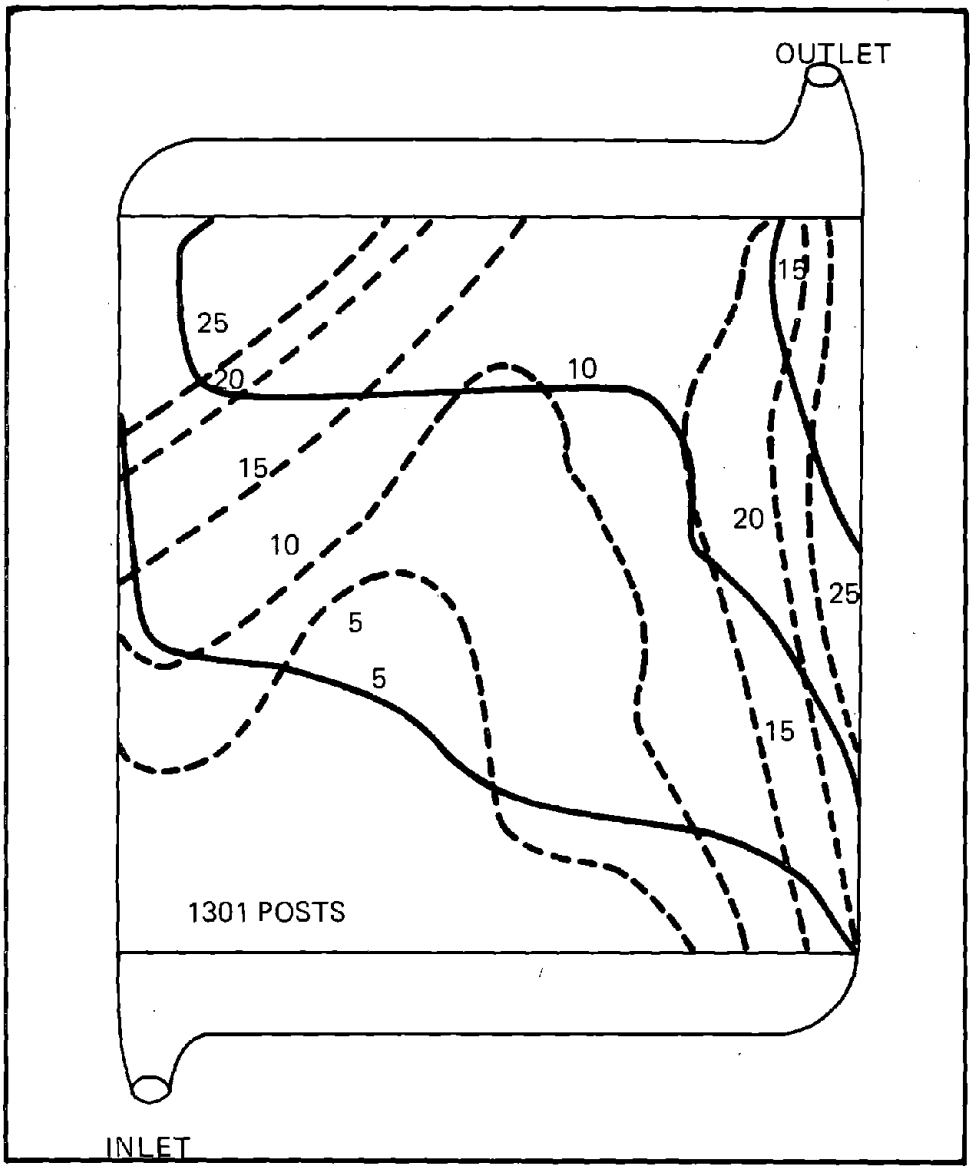

DYE TRACER MOVEMENT

(5 SECOND INTERVALS)

---- NORMAL FLOW FRAME
—— MODIFIED FLOW FRAME

20-25 ml/dm^2 MIN FLOW RATE

Figure IV-13 Electrolyte Distribution in Flow Frames

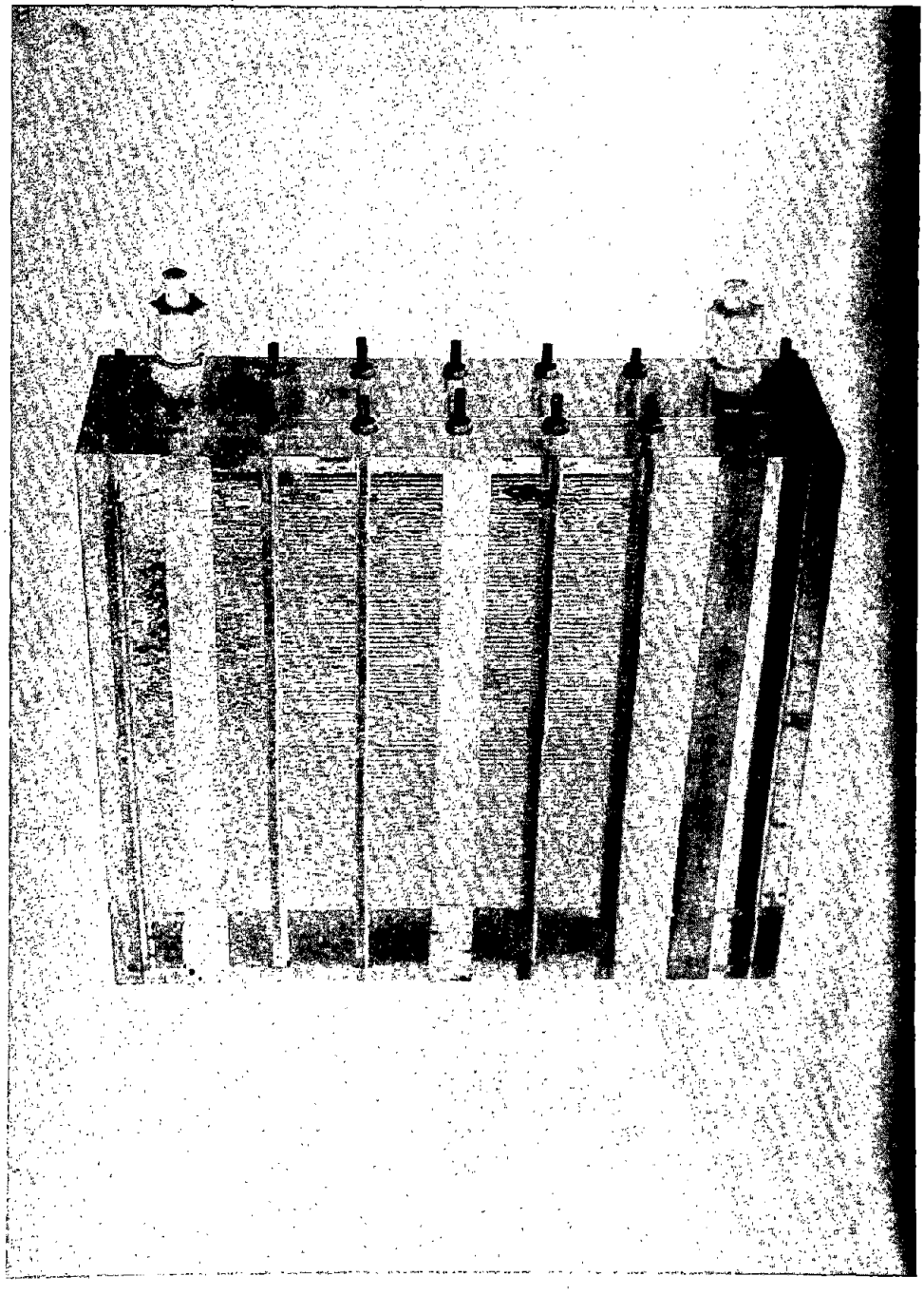

Figure IV-14 Manifold Flow Simulation

3/8" slot. The slots simulate flow frames or cells. Each sheet was .025 + .004 inches thick. The ends of the stack were connected to a variable speed pump and had various pressure taps. Pressure drop vs. flow rate were measured under various conditions. Dye tracers gave visual indications of maldistribution. In some cases, individual channel flow rates were measured directly by high speed photography of the dye tracers. The effect of stack size was measured by increasing the number of "flow frame" components. The effect of manifold diameter was measured by placing a crescent shaped insert into each manifold, which effectively reduced the manifold from 3/8" to 1/4" or 3/16". These inserts were made from 3/8" teflon rods by using a hemispherical mill to remove approximately circular cross-sections. Most flow studies were performed with distilled water.

Experiments concentrated on the "U" configuration as opposed to the "Z", as shown in Figure IV-15. The "U" configuration is preferred to avoid shunt currents in the external plumbing. Very large stacks or small manifold diameter favored maldistribution. In the "U" configuration, cells nearest to the flow inlet get the most flow. In the "Z" configuration, cells furthest from the flow inlet get the most flow. Figure IV-16 shows the results of pressure drop vs. flow rate for water at various diameters and stack sizes in the "U" configuration. Regions of extreme maldistribution are indicated.

A study was made to develop correlations of the pressure drop for flow of liquid through the Zn/Br_2 battery, since pressure drop is one aspect affecting optimum cell design and operation. The resulting correlations are based on the simulator, using either water or standard electrolyte as the circulating fluid. Only the "U" configuration data was correlated. Literature articles helped to firm up the theoretical basis used in correlating flow distribution manifolds (14, 15).

The theoretical analysis correlates the data reasonably well over the full range, except for some runs using standard electrolyte with the 1/4" manifold. These runs show somewhat higher pressure drop in the manifold, which might be explained by a small change in location of the pressure taps and/or by a small restriction in diameter. The theory is based on a simple picture as follows. Overall pressure drop is the sum of a viscous flow pressure drop within the cells, plus a turbulent flow pressure drop for the in and out manifolds. These flow regimes are confirmed by the calculated Reynolds Numbers. Thus, the relative contribution to pressure drop of cells and manifolds is reflected in the slope and curvature of experimental curves for pressure drop versus liquid flow rate. Also, the number of cells in parallel has less effect at higher flow rates where turbulent pressure drop becomes dominant, but the number of cells is a major factor at very low flow rates.

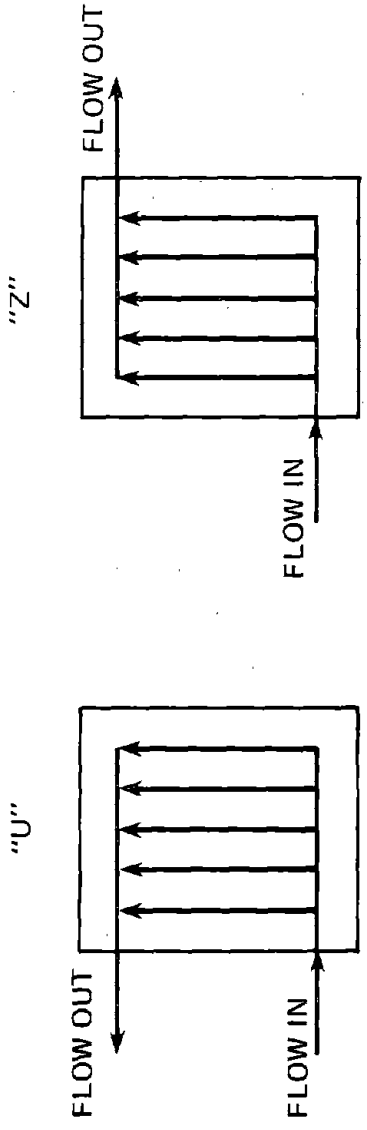

Figure IV-15 Comparison of "U" and "Z" Manifold Connections

The analytical approach was tested first against the experimental data with water as shown in Figure IV-16. At the lowest flow rates, pressure drop corresponds mainly to viscous flow as judged from the slope of pressure drop versus flow rate. Similarly, at the highest flow rates tested, turbulent flow pressure drop predominates. Since both turbulent and viscous flow are important factors, these tests provided a severe test of the model, and also made the analytical study more difficult. Some test runs were made using a solution of gum in water, and these runs define the effect of liquid viscosity on pressure drop.

Experimental results on battery electrolyte are shown in Figure IV-17 in three groups based on diameter of the manifold insert used. Lowest pressure drop is with 3/8" diameter manifolds, as shown at the right on Figure IV-17. The number of cells in parallel has a large effect at low flow rate, but less at high flow rate. The curves also show an increase in slope as flow rate increases, since turbulent pressure drop becomes dominant.

Predictions of pressure drop with electrolyte were made from data on water, assuming a 1.6 density and a viscosity 2.7 times that of water. Predicted points are shown and are in good agreement with the data.

At the left on Figure IV-17 are data with the smallest manifolds, 3/16" diameter. Pressure drop is much higher, and the slopes are close to two, as would be expected for turbulent flow. Predicted points are also shown on the same basis as before. The simple model predicts a continued decrease in pressure drop as the number of cells increases, whereas the data show a reversal. The reversal is probably due to increasing length of manifolds which causes an increase in pressure drop when the number of cells becomes large and the L/D ratio for the manifold exceeds 25. Allowance for this effect can be easily added to the model; however, it is not significant in the range expected to be of interest for the battery.

Overall pressure drop for the manifolds (in and out) is included at 1.3 velocity heads for all systems, with water or complex. This assumption fits the data fairly well and is consistent with theory and the literature. It is estimated that there is a pressure regain in the inlet manifold of about 0.5 velocity head. At some time, it might be desirable to refine the model by using a variable factor rather than 1.3, in order to give a better prediction of pressure drop. With long manifolds of small diameter, it will probably be a function of L/D for the manifolds.

Data for the 1/4" diameter manifolds is shown in the middle part of Figure IV-17. Results with water flowing are predicted well by the simple model, but the predictions are low for flowing electrolyte.

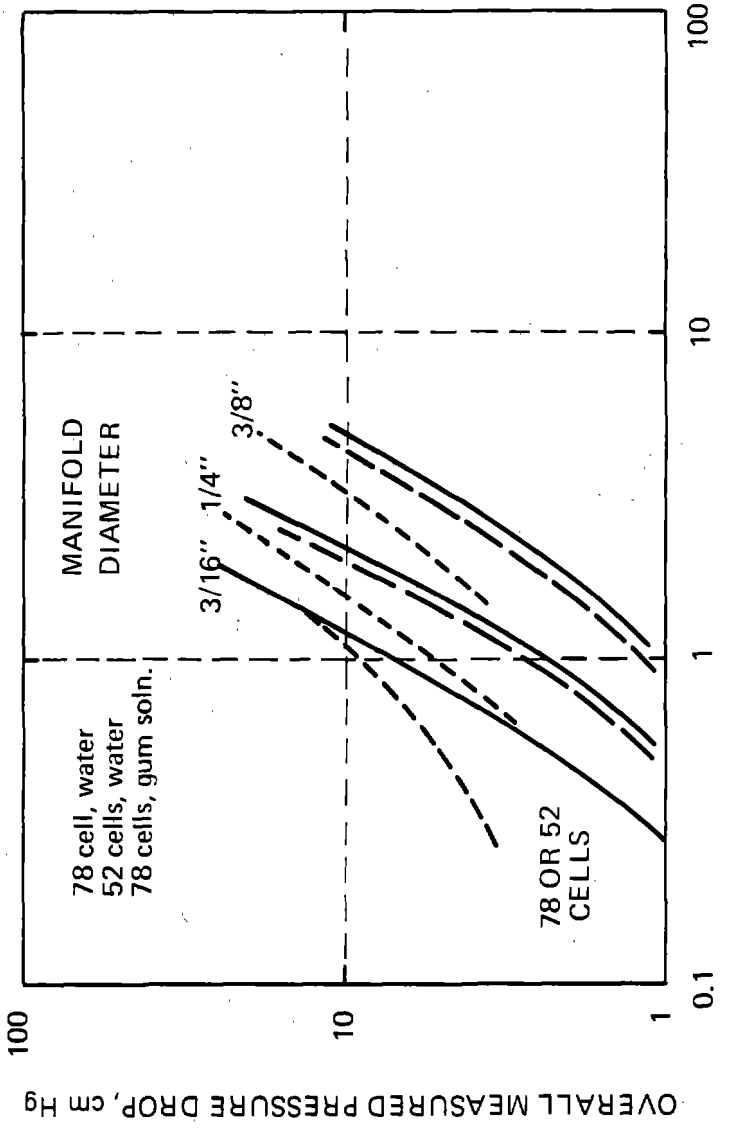

Figure IV-16 Pressure Drop Through Manifold Simulator with Water

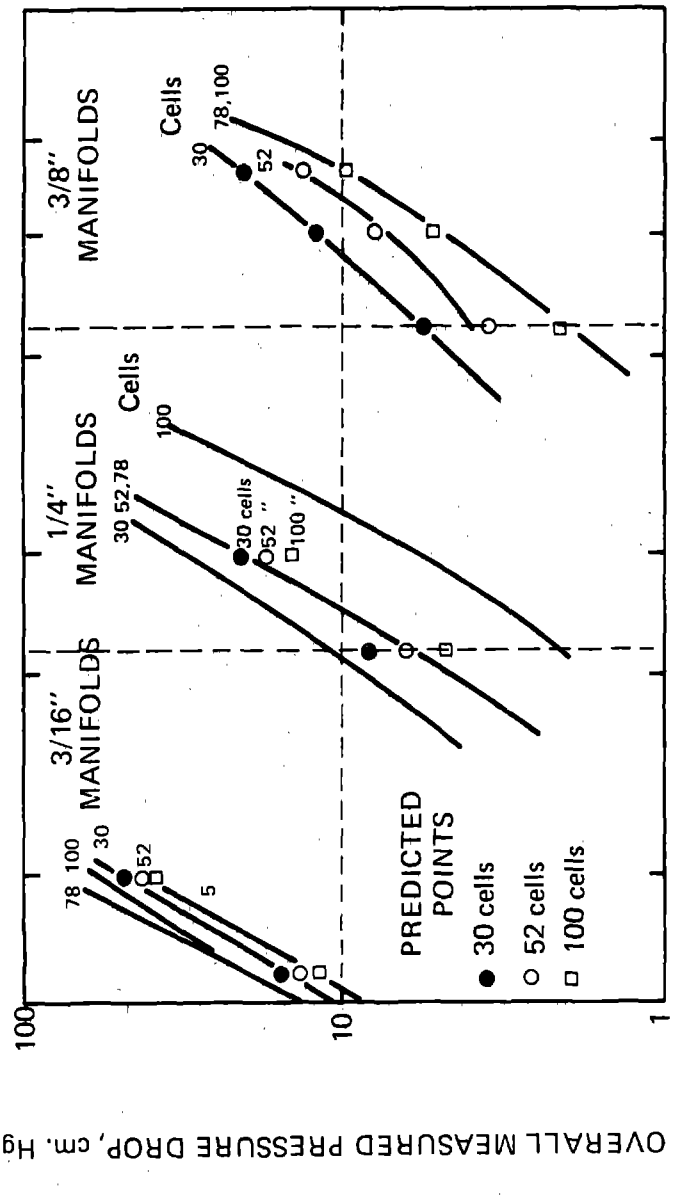

Figure IV-17 Pressure Drop Through Manifold Simulator with Standard Electrolyte

In addition, the experimental slopes are steeper, indicating more turbulent flow pressure drop than predicted. Possibly, this could reflect some variation in placement of the manifold insert. The data for 100 cells with electrolyte appears to be out of line, showing lower pressure drop than with water.

In general, the mockup results seem to be consistent with pressure drop found in operating batteries. If desired, refinements could be added to the model to make empirical adjustments and to allow for effects such as gas bubbles, etc. A generalized equation for pressure drop in the mockup cells using standard electrolyte is as follows:

$$P = \frac{55\mu(Q)}{N} + \frac{S(Q)^2}{134d^4}$$

P = Measured pressure drop, cm. Hg
μ = liquid viscosity, centipoises
Q = flow rate, gallons per minute
N = number of cells in parallel
S = liquid density, g/cm^3
d = manifold diameter, inches

To convert to psi pressure drop, the above numbers should be divided by 5.9. This factor includes a correction for density difference in the manometer legs.

V Phase II Program

Phase II is an intermediate step in an overall three phase program whose goal is the delivery of an optimized stand-alone 20 kWh zinc-bromine battery. This battery will be delivered to the contract monitor at Sandia National Laboratories for testing and evaluation in domestic photovoltaic applications. The principle focus of Phase II is to serve as a stepping stone to the final delivery, by concentrating on broadening the technology base and gaining more experience with large batteries, in continuing the scale-up to a full 20 kWh module. The overall time table for Phase II shown in Figure V-1 is based on an eight month period of active investigation and development followed by a final report. Specific sub-tasks which go beyond Phase I activities are described below.

20 kWh (X-20) Module - This activity represents the scale-up to the ultimate storage capacity envisioned for the final Phase III deliverable. However, this scale-up to 20 kWh (X-20) represents more than just two 10 kWh submodules (X-10's) in parallel. In fact, X-10 represented considerable system improvements beyond being merely three 3 kWh submodules (X-3) in parallel. The X-10, in addition to being an initiative in multistack operation, demonstrated several new technology improvements that had shown great promise in parametric testing but were never fully tested at the X-3 level. These changes and the reason for their substitutions are shown in Table V-1a. During the building and cycling of X-10, new components became available, and design improvements and modifications became apparent. The major changes envisioned for X-20 over X-10 are shown in Table V-1b. These changes represent an additional system learning curve by allowing for further "shakedown" of the system. Figure V-2 shows the anticipated layout of X-20. Six stacks will be run electrically and hydraulically in parallel. The stacks will be fed by a common central block which incorporates the interstack manifold for electrolyte distribution. The stack will be located above a tray which serves as the cover for the electrolyte reservoirs. The stacks are spaced to allow for voltage sensors and occasional inspections. Each stack will be composed of 52 bipolar cells, giving a nominal 80 V discharge. The electrodes will be insert injection molded, alternating with Daramic separators and Vexar support screens. The electrolyte will be circulated by two centrifugal pumps. A reversing valve will allow periodic degassing of the catholyte. All components for X-20 are currently either available or on order.

Microprocessor Controller Development - Stand-alone battery operation requires a "smart" battery that knows how to turn on, turn off, charge, discharge, and hold, as well as perform occasional system maintenance. The degree of complexity and the stand-alone duty cycle seems appropriate for low cost 4-or 8-bit microprocessor control. Because of greater versatility and the availability of support documentation, an 8 bit system was selected for initial development. System control inputs and outputs will be defined and software will be developed to allow delivery of a microprocessor controlled battery to Sandia for testing early in Phase III.

FIGURE V.I PROPOSED PROGRAM PLAN, PHASE II

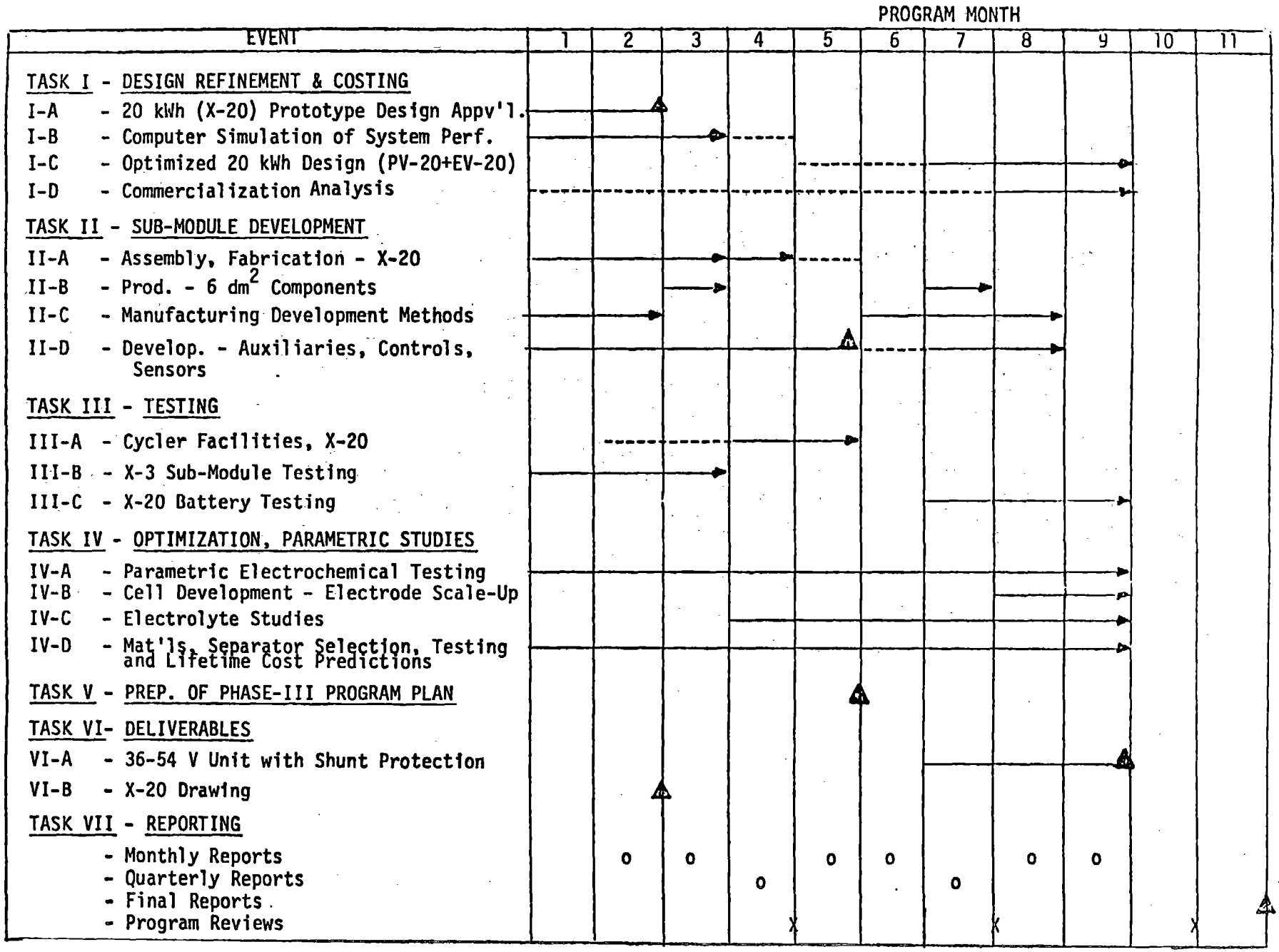

Table V-1a Comparison of X-3 vs X-10 Technology Changes

Characteristic	X-3A	X-10	Comments
Configuration	One 52 cell stack	Three 52 cell stacks	Scale-up Capacity Multistack Operation
Electrodes	Compression Molded Separate Flow Frames	Injection Molded Combined with Flow Frames	Faster Production Battery Tolerance Control
Separator	Ion Selective	Microporous and Electrolyte additive	Cost Effective Design
Shunt Current Protection	External Negative Electrode	Internal Negative Electrode	More efficient operation
Stack Compression	Internal Bolts	External Bolts	Faster Assembly
Heat Exchange	None	Tantalum Tubes	Control Thermal Build-up
Voltage Sensing Tabs	Pt at Anode	Pt at Cathode	Accommodate change to injection molded electrode
Pumps	Centrifugal	Reversible at Catholyte	Simplify Design

Table V-1b Comparison of X-10 vs X-20 Technology Changes

Characteristic	X-10	X-20	Comments
Configuration	Three 52 Cell Stacks	Six 52 Cell Stacks	Scale-up Capacity
Pumps	Reversible at Catholyte	Centrifugal	More Reliable
Voltage Sensing Tabs	Pt on Cathode	Ta at Anode Reduce number	Eliminate Sources of Gassing Speed System Assembly
Protective Electrodes	Internal Electrodes	Improved Internal Design	Easier Assembly Better Reproducibility
Heat Exchange	Tantalum Tubes	FEP Tubes	Eliminate Leaks Less Expensive
Interstack Manifold	Flat Polyethylene Gasket	Foamed Polyethylene Gasket	Eliminate Cross Flow

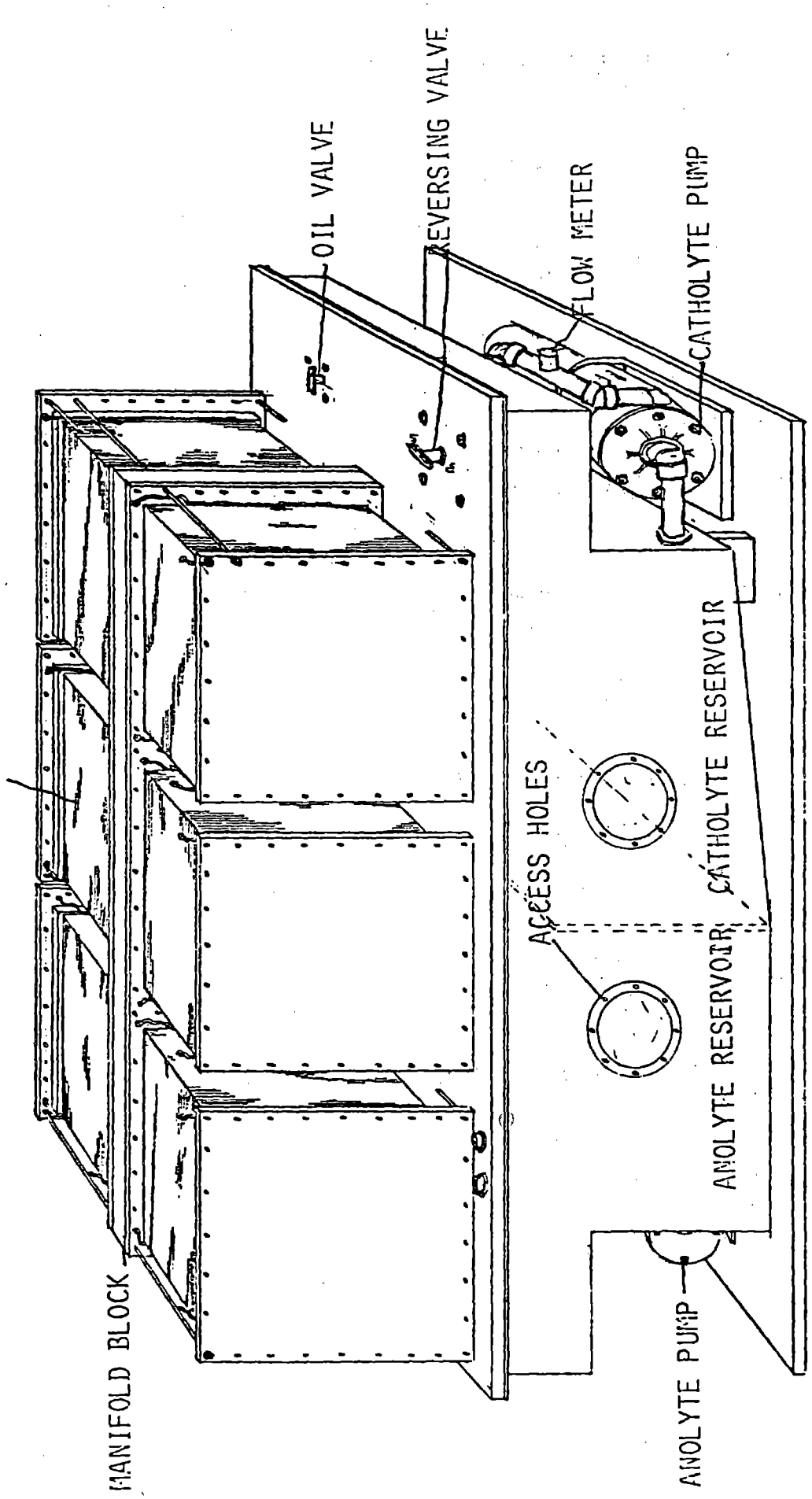

Figure V-2 20 kWh Zinc Bromine Battery - X-20

Sensor Development - Various inputs to the microprocessor controller will require the modification or adaptation of existing sensors and materials. Various sensors for state-of-charge (SOC) monitoring and electrolyte pH will be investigated.

Computer Simulations - In order to further optimize the system performance, a computer simulation will be developed. It will describe both cell electrochemistry and system interactions, in particular, auxiliary power requirements for shunt current protection (manifolds and tunnels) and pumping power. The model will furnish a firm basis for comparing system modifications in terms of changes in electrolyte properties, separators, flow rates and system dimensions. This should facilitate both additional improvements in system performance as well as allow tailoring of the zinc-bromine system to specialty applications.

Electrode Scale-Up - Present electrodes based on 600 cm^2 active areas and present operating parameters, require six stacks to achieve 20 kWh capacity. Recent cost studies (Section I.2) showed that significant stack costs were associated with the ends of each stack, i.e. the current collectors and the protective electrodes. An additional scale-up to at least 1200 cm^2 electrodes is planned. This will reduce the number of stacks, thereby improving system cost by reducing the external plumbing, electrical connection and end-of-stack costs.

Extended Automatic Life Cycling - Two automated life stations are being constructed to allow continuous, round-the-clock testing of bipolar parametric batteries. This will allow the more rapid accumulation of life cycle data and provide experience in automatic control, to guide development of the microprocessor controller.

VI Deliverable Batteries

The Phase I work statement called for the delivery of two (2) battery systems as part of the contract effort. The first deliverable was a 12 V (8-cell), 500 Wh system, such as the one described in Section IV, and was due six months after the start of the contract period. This battery system was delivered to Sandia Laboratories in September of 1980, as scheduled. A detailed operating manual formed a part of this package.

The second deliverable was a 30 V (20-cell), 1250 Wh battery system, similar in design and construction to the larger (52-cell) units described earlier. Because of the higher operating voltage, the system included shunt current protection. A complete description of the system, along with photos and schematic diagrams, operating instructions, and parts lists was submitted as an Operating Manual under separate cover. This deliverable, which was due at the end of the contract period, was delivered in April, 1981, as scheduled.

The 12V battery has been under cycle testing at Sandia Laboratories. A summary of their first 100 cycle test results is included as Appendix 4.

VII Conclusions from Phase I

Phase I is now complete, and all specified program tasks have been accomplished. In many areas, progress has exceeded our original goals. With the experience gained during Phase I, we are confident that the remaining tasks in Phases II and III can be completed in a timely fashion, and that a stand-alone Zinc-Bromine Photovoltaic Battery can be delivered to Sandia at the conclusion of Phase III. Some concluding comments on specific accomplishments and some thoughts for the future are given below:

VII.1 Cost Effective Design - Successful commercialization of any advanced battery system will require that it is cost competitive with its existing competition. Our recent manufacturing cost estimate is based on a better defined system and on more actual plastic fabrication experience than our previous estimates. In many areas, present estimates are still conservative. Of course, more work remains to be done to tie down auxiliary costs and indirect manufacturing costs. All factors considered, at the present state of technical demonstration and manufacturing development, we feel that Exxon's zinc-bromine battery is a cost effective advanced battery candidate. This is an important asset as advanced markets develop.

VII.2 Forgiving System - Batteries based on zinc and bromine have many forgiving characteristics and an inherent system resilience which promises long cycle life. With circulation, zinc plating is flat and uniform. But, even if the plating changes, a slight excess of Br_2 permits the complete discharge of plating mistakes. The electrodes do not interact with the active zinc-bromine so shape and morphology changes are ruled out. Overdischarge and overcharge are tolerable. Bromine complexing agents improve plating and reduce H_2 evolution. H_2/Br_2 recombination should allow pH invariance. The bipolar structure and resistive membrane also stabilize uniform plating. These and other forgiving aspects have combined to make recent scale-ups to 600 cm^2 electrodes and multi-stack, multi-kWh demonstrations relatively trouble free.

VII.3 No Clear Life Limiting Mechanism - Recent expansions in cycle life, particularly in the 3 kWh (X-3A) submodule, are encouraging in terms of short range system life limits. Longer range studies of individual components in the stack and in the electrolyte have yet to show any clear life limiting mechanism. Problems have occured in earlier designs from electrolyte maldistribution, but these occured during initial cycling and seem to be eliminated by the new flow frame design and the increased uniformity of injection molding. Shunt current problems are under control. Microporous membranes show better long term stability than ion-selective materials, in addition to being more cost effective. Electrolyte pH increases have limited several earlier system life cycle studies, but the mechanisms are now known and seem easily controllable, particularly with H_2/Br_2 recombination.

Extending system life can be like peeling an onion. Cutting away each outer layer exposes a new one. More component testing and automated life cycle testing are the only ways to speed extension of any system's proven cycle life. These areas will be given more effort during Phase II. Until some clear failure mechanism is identified, the ultimate system life is difficult to predict but perhaps life will be predictably long.

VII.4 Rapid Progress - Substantial progress has been made during the last two years. Electrode scale-up from 100 to 600 cm^2 and system scale-up from a three-cell bipolar stack to a shunt protected 10 kWh submodule have remained close to schedules. Because of this progress, Exxon's circulating zinc-bromine system has become leading contender among advanced battery systems, for a wide variety of applications.

VII.5 Multimarket Strategy - As a project evolves from research to development to commercialization, the required talents, perspectives and pressures change. Adaptability is essential to survival. In evolving markets, timing can be as important as performance specifications and costs. Costs and performance projections for Exxon's circulating zinc-bromine battery are attractive. However, the timing of the photovoltaic storage market depends on many factors, foremost among which is the cost of solar power. This factor makes the projected timing of the solar storage market uncertain.

Fortunately, the zinc bromine battery's performance (See Section I.1), is also suitable for advanced applications in bulk energy storage and electric vehicles. These applications are presently limited by the lack of a suitable battery rather than by peripheral or support technology. Both of these applications have uncertainties, but the timing and scale of their markets are more easily predicted than the solar case. The present Exxon zinc-bromine system could be readily adapted to these other applications with minimal redesign. In terms of developing the timing of market strategies, this broad adaptability of the zinc-bromine system is a major asset. Commercialization with this multi-market strategy, in terms of cash flow, rates of expansion and return-on-investment, offers Exxon's zinc-bromine battery more flexibility in timing than some other advanced batteries, which are suited to only single applications.

References

1. Eustace, D. J. and Malachesky, P., "Metal-Halogen Electrochemical," U.S.P. #4,064,324, December 20, 1977.

2. Venero, A., U.S.P. #4,105,829, August 8, 1978.

3. Clerici, G., Rossi, M., and Marchetto, M., Power Sources 5, D. H. Collins, Ed. Oriel Press, (1975).

4. Walsh, M., U.S.P. #3,816,177 (1974).
Walsh, M., Walsh, F., Crouse, D., Proceedings, 10th IECED, 1141 (1975).

5. Bellows, R., Eustace, D., Grimes, P., Schropshire, J., Tsien, H., and Venero, A., Power Sources 7, J. Thompson, Ed., Academic Press, London, 1979.

6. Putt, R., "Assessment of the Zinc-Bromine Battery for Utility Load Leveling," Interim Report (Sept. 1977), EPRI Contract #RP635-1.
Putt, R., "Assessment of the Zinc-Bromine Battery for Utility Load Leveling," Interim Report (Jan. 1977), EPRI Contract #RP635-1.

7. Will, F., Proceedings, 12th IECEC, 250 (1977).

8. Lim, H. S., Lackner, A. M., and Knechtli, R. C., J. Electrochem. Soc., 124, 1154 (1977).

9. Will, F., and Spacil, H.S. J. Power Sources, 5, 173-188, (1980).

10. Caskey, D., Caskey, B. and Aronson, E., "Parametric Analysis of Residential Grid-Connected Photovoltaic Systems with Storage", Sandia Laboratories. SAND 79-2331.

11. Eustace, D., J. Electrochem. Soc. 127, 528 (1980).

12. Kinoshita, K. and Bett, J., Carbon, 11, 237-403, 1973.

13. Kinoshita, K. and Bett, J., Carbon, 12, 525, 1974.

14. Gruver, G., J. Electrochem. Soc., 125, 1719, (1978).

15. Bajura, R. A., and Jones, E. H. Jr., Journal of Fluids Engineering, ASME, 654-666, (1976).

16. Acrivos, A., Babcock, B. D., and Pigford, R. L., Chem. Eng. Science, 10, 112-124 (1959).

APPENDIX I

Advanced 20 kWh Design Calculations

The design for X-20 was based on the following parameters:

- Net output - 75 mAh/cm^2 at an average discharge of 1.55 volts/cell.
- Electrolyte composition - 3M $ZnBr_2$ and 1 M quaternary amine bromide complexing agent. - specific gravity 1.6
- Electrolyte utilization - 70%
- Coulombic efficiency - 80%
- Auxiliary energy discharge - 5% of capacity
- Apparent state of charge, SOC, - 70% of the total zinc in electrolyte
- Apparent loading - 94 mAh/cm^2
- Average charge voltage - 1.9 volts/cell
- Average discharge voltage - 1.55 volts/cell
- Discharge time - 3 hours at 25 mAh/cm^2
- Charge time - 3 hours at 31 mAh/cm^2
- Gross output - 21.05 kWh during 3 hours
- Net output - 20 kWh during 3 hours
- Output conditions - 75 mAh/cm^2 at 1.55 volts average for 3 hours
- Peak power - 26 kW

The quantity of zinc bromide electrolyte needed for a given Zn/Br_2 battery system can be calculated as follows:

$$\text{Liters} = \frac{\text{kWh}\ (1000)}{V_d(F)(F/M)(M/L)(U)(E)}$$

where:

kWh = gross kilowatt hour capacity of battery

V_d = average discharge voltage per cell

F = Faraday = 26.8 amp-hours/equivalent

F/M = Faradays per mole; for zinc, 2

M/L = moles per liter of zinc

U = utilization of electrolyte (state of charge)

E = coulombic efficiency

The weight of electrolyte is the product of electrolyte volume and its density.

Weight of electrolyte = (liters) (density).

The volume and weight of electrolyte can be minimized by increasing the discharge voltage, concentration, utilization, and efficiency on discharge. These, however, are not independent variables and must be determined or fixed for specific conditions.

Using the above formulas and with coulombic inefficiency assigned to discharge, the volume of electrolyte is 150 liters and the weight is 240 kg or 530 pounds. The electrolyte net energy density terms are 133 Wh/liter or 2.2 Wh/in^3 and 81 Wh/kg or 38 Wh/#.

The battery construction is shown in Figure 0.3. The weight estimates are given in Table A-1. The conservative estimates of volume and weight yield 1.41 Wh/in^3 - 1.8 Wh/in^3 and 28.5 Wh/# or 63 Wh/kg.

TABLE A-1

BATTERY WEIGHT ESTIMATES FOR 20 kWh DESIGN

Component	Weight (pounds)
Electrolyte *	536
Bipolar Electrodes (157)	31
Separators (156)	5.2
Separator Frames (156)	41.6
End-Support Block (2)	8.3
Center Feed Block	8.3
Reservoir	12.9
Reservoir Tray	3.0
Accessories	
Tie Rods, Nuts, Washers	3.0
Motors & Pumps	25.0
Miscellaneous Controls	8.0
Bus Bars & Miscellaneous Hardware	10.0
Plumbing & Miscellaneous	10.0
	702
Additional for EV	10

* Electrolyte weight and volume based on present operational parameters.

APPENDIX 2

Costing of 20 kWh Battery

INTRODUCTION

The major factor in the utilization of any battery system is the initial battery cost. Another important factor is the battery life as measured by cycle life (number of cycles and the character of the cycle). The power density, energy density, and overall or 'round trip' efficiency are also very important considerations. (The relative importance of these factors varies with the actual battery use and the design is often dictated, at least in part, by this desired battery use).

TWO STACK - 20 kWh ZINC BROMINE BATTERY

BATTERY CONSTRUCTION

The battery module shown in Figure A1 uses basically an all plastic construction. It consists of two stacks of 78 separator and frame assemblies alternating with 77 bipolar electrodes. At each end of the 78 cell stacks are the collectors, one anode and one cathode collector for each stack. The collectors are also made of plastic and incorporate conductive plastic electrodes with metallic screens for current collection. The two stack module is assembled on a tray which serves as a cover for the electrolyte reservoir. The electrolyte pumps (pump heads) are within the reservoir while the DC motor drives (operating from the battery itself) are external to the reservoir. The configuration shown is designed for motive power. For bulk energy storage or solar (photovoltaic) use, the cover, inner tray and safety shield would not be required. The tray and shield serve to confine the catholyte in the event of a vehicle collision where the electrolyte tank might be ruptured. For stationary systems the base tank (reservoir) would incorporate a divider to separate the catholyte from the anolyte. Each stack has a nominal 120 V DC output. The battery stacks are wired in parallel. The electrolytes (anolyte and catholyte) would be fed by the pumps up through a center plastic 'feed' block between the two battery stacks. No external plumbing would be required. All the stack components other than the four reinforcing corner tie rods and the metal screen collectors are of compatible plastic and simple heat sealing of the top, bottom, and sides provides sufficient strength and sealing of battery surfaces.

BIPOLAR CELL CONSTRUCTION

Each cell consists of two components, the electrode and separator. The bipolar electrode, a thin sheet of electrically conductive plastic with a non-conductive border, has a catalytic surface on one side. The entire electrode can be extruded and coated with the catalytic layer. Alternating with the electrode is a thin sheet of a microporous plastic serving as a separator. The separator is held in an injection molded plastic frame. Manifolds providing for the electrolyte flow are incorporated in the frame.

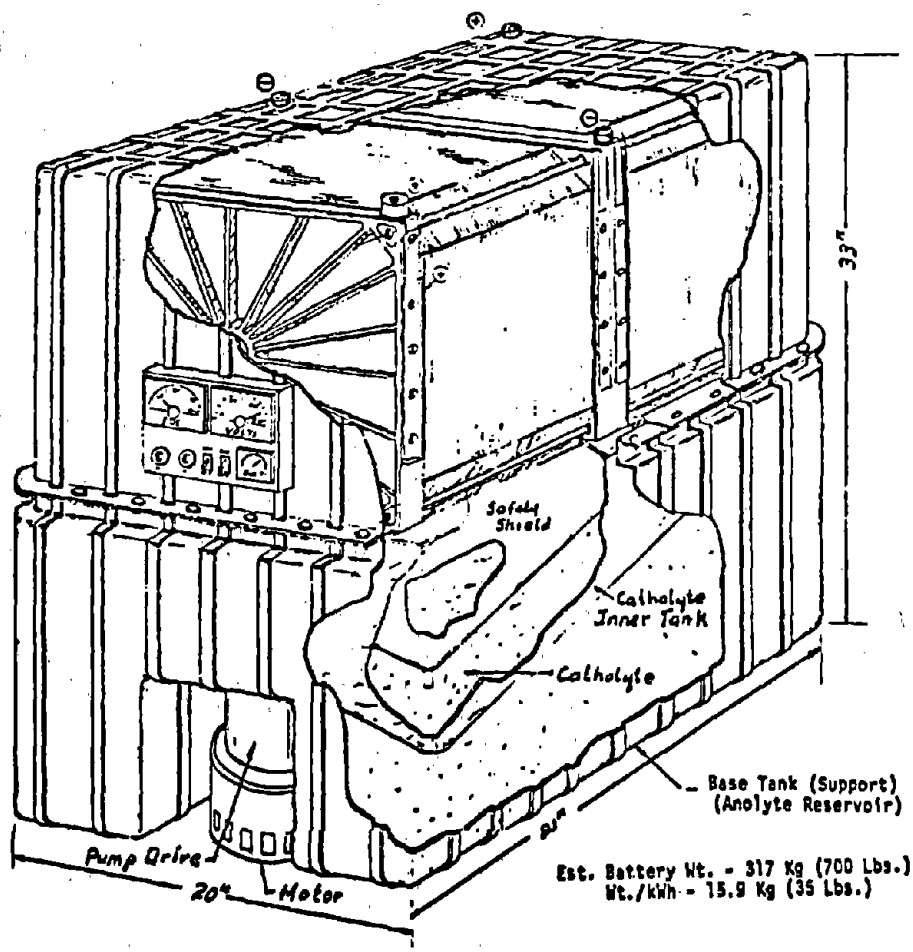

Figure A-1 20 kWh Zinc Bromine Battery

The 20 kWh battery as described has electrodes with about 1200 cm^2 active areas, double the active area in present prototype batteries. The scale-up is considered moderate and no problems are anticipated. The present 600 cm^2 electrodes, scaled up from the original 100 cm^2 electrodes, have been extensively tested in .5, 3 and 10 kWh submodules and have shown no scale-up problems.

BATTERY COSTING ANALYSIS

A study of direct factory costs to produce this 20 kWh design was conducted at various production rates. The costing methodology assumed an assembly type operation where most of the components would be purchased from outside vendors. Estimates of purchased components are based on present quoted costs of machine and operator. Accessory items, not yet fully defined, (pumps, controllers etc.) are best estimates. In-house factory labor estimates are based on station by station time estimates as anticipated after the second or third year of operation when the problems of an initial start up have been solved. In-house labor consists primarily of the assembly of battery stacks, the attachment of the stacks to the reservoir, installation of accessories and final testing of the assembled module.

The assembly plant approach has certain advantages and disadvantages. Quotes from experienced vendors are likely to be more reliable than in-house estimates of component fabrication, so that uncertainties in the cost estimates are reduced. In limited production, extensive use of outside vendors is likely because this approach reduces capital and labor requirements where full time production personnel are not required. Thus capital, labor and space are only required for the final assembly.

The "assembly plant" approach however, tends to be conservatively high for large scale production estimates. Dependence on several outside vendors would require higher inventories and more lead time for coordinating production. In large scale production, plastic fabrication machinery (the largest capital expenditure) could be occupied full time. Therefore a shift to total in-house production would undoubtedly reduce costs by eliminating intermediate overhead and profits as well as inventory requirements. Future studies will investigate a more integrated in-house plastic fabrication approach.

The term "factory cost" includes most direct charges for assembly of 20 kWh units. It does include required raw materials, purchased components, accessories, direct labor costs, worker benefits, quality control and supervision. It does not include indirect charges such as inventory costs, depreciation of plant and equipment, working capital, tooling, sales and general administration costs, development costs and return on investment (ROI).

An overview of the factory cost study for this 20 kWh battery indicates the factory cost to be $28/kWh at a production rate of 100,000 units per year (1980 dollars). Various indirect costs as described above need be added to arrive at the selling price (OEM). Figure A-2 is a 'pie chart' cost breakdown showing the major costs such as purchased stack and reservoir parts, accessories, electrolyte and in-house labor. The low in-house labor percentage reflects the assembly plant viewpoint since labor is required only for final assembly. Additional labor and overhead are included in the cost of purchased components. A more complete breakdown is shown in Table A-2. Major cost items are the battery stack components (bipolar electrodes, separator assemblies and current collectors) and the electrolyte. Detailed cost analysis of these items follows.

- Bipolar Electrode These are fabricated by co-extruding carbon plastic sheet 11-1/4" wide with side borders of non-conductive plastic 2-3/8" wide. A layer of conductive-high surface area material is applied to the carbon plastic area. Total cost of the Bipolar Electrode will be about $0.15 each, plus or minus $.02, depending upon the final process. An additional $.01 is added for acid cleaning and handling. At battery production rates of over 1,000/year, the extruded materials above would be applied continuously and the extrusion would be pierced and blanked continuously. For a 20 kWh battery, 154 bipolar electrodes are required. At an estimated 2% rejection of material, 157 electrodes will be considered.

Normal 2-1/2" extrusion machines can produce 300 lbs/h. Because of the high viscosity of carbon plastic and the co-extrusion process, it is estimated that 100 lbs/h is more feasible. Machine and operator cost is $33.00/h. Five hundred parts per hour would thus be produced.

*Material per electrode	$.178	* Includes added factor of 5%
Labor - Extrusion (Outside purchase)	$.066	
Total Cost/Unit	$.244	
Total Cost/Battery (157 pieces)	$38.30	

- Separator Assembly The separator assembly consists of a non-conductive plastic frame injection molded around a 'separator' insert. The insert is 11" x 16-3/8" x .024" thick Daramic with numerous 'posts' (average thickness, .027"). The separator stack is purchased on rolls 11-1/2" wide. A length of 17" is allowed for blanking (1.36 ft^2 required per unit). Based on 1979 prices for .010" separator material of $.05/$ft^2$, the .024" material would be approximately $.12/$ft^2$, or $.163/unit. Pierce

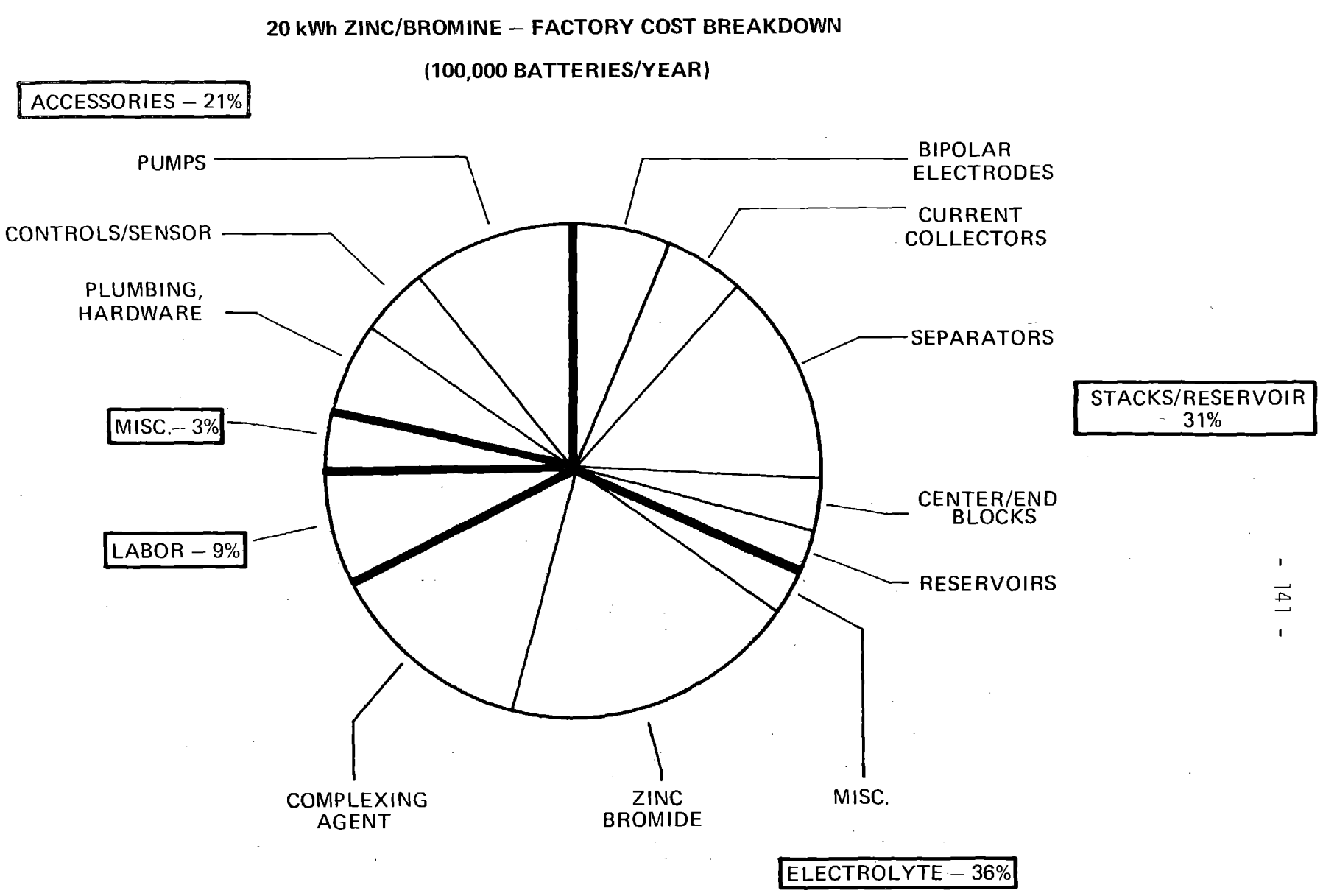

Figure A-2 Factory Cost Analysis

TABLE A-2

TOTAL FACTORY COST -
20 kWh ZINC-BROMINE BATTERY

Bipolar Electrodes	38.30
Current Collectors	28.20
Separator Assembly (Inc. outside labor)	77.44
End-Support Block Assembly	10.52
Center-Support Blocks (Inc. outside labor)	10.36
Reservoir	8.59
Reservoir Tray	2.95
Battery stacks - Total	176.36
Electrolyte Pump	24.00
Electrolyte Pump Motor	16.00
Isolating Drive System	10.00
Protective Electrode System	10.00
Pump Pressure Sensor	4.00
Electronic Control Board	12.00
Electrolyte Level Sensor	2.00
State-of-Charge Sensor	4.00
Voltage Cut-Out	1.50
Temperature Probes (3)	3.00
Hydrogen Recombination	2.00
Plumbing & Fittings	10.00
Bus Bars - Tie Rods & Hardware	20.00
Batt. Access., Controls, Etc. - Total	118.50
Electrolyte	200.00
Packaging & External Case	18.49
Materials - Total	513.35
In-House Labor	47.75
Factory Cost Total, $/Unit	561.10
Factory Cost Total, $/kWh	28.05

& blank operations produce 1800 pieces per hour. 156 pieces are required plus 4 rejects - totalling 160 pieces. The frame is .075" thick and is 14-1/2" high x 18" wide.

Frame Volume = 7.42 in^3
Frame Weight = .256 lbs.
At $.45/lb, Base Material Cost (Frame) = .115 + .163 = $.278/Unit
- Talc-Filled PP is assumed @ $.45/lb.
- Molding Costs (outside) are assumed to be a two out operation at 1,000 batteries/yr., or more. Machine and operator at $23.00/hr. Cycle-time is estimated at 60 seconds.

*Material (Frame & Insert)	$.292	*Includes added factor of 5%
Labor (Outside Purchase)	$.192	
Total Cost/Unit	$.484	
Total Battery (160 Pcs.)	$77.44	

- Current Collectors Anode and cathode collectors are similar, except for the coating on the cathode. Each collector would be a 'sandwich' structure, consisting of a bipolar electrode, a silver-plated 'expanded' lead foil, and a plastic backing sheet. 3.9 oz. plastic (.030" x 14-1/2" x 18") at $.42/lb costs $.103 each. The lead sheet (.015" thick) would be expanded 3:1 (.005" equivalent). Silver plating would be .0003" both sides and around strands.

	Mat'l.	Labor
Silver	6.31*	-
Lead Foil	.15	-
Expanding Foil(outside)	.20	-
Plating Ag. (outside)	.15	-
Bipolar Electrode	.24	
Laminating Electrode-Compression Mold @ 30 pcs./h		$.50 (In-house Operation)
	*(Based on $22./ troy oz.)	

Material/Unit	7.05
Material/Battery	28.20
In-house Labor per Battery	$2.00

- Electrolyte The standard electrolyte is 3M $ZnBr_2$ and 1M quaternary ammonium bromine complexers which is 70% utilized at 80% coulombic efficiency in this design. Zinc bromine solution production costs from zinc dust and HBr are $.46/lb of contained salt. As a check, this compares favorably with zinc chloride solution which is commercially made from zinc oxide and HCl. Quaternary ammonium halide quotations have been given in the range of $1.00/lb. This leads to a conservative electrolyte price of $200.00 for this battery.

Zinc-Bromide Salt 241 lbs @ $.46/lb	=	$110.00
Quaternary Amine Halide 75 lbs @ 1.00/lb	=	75.00
De-Ionized Water plus handling	=	15.00
Cost per Battery		$200.00

CONCLUSION

Future work on Exxon's Zinc-Bromine Battery will focus on extending the demonstrated system life via automatic testing as well as a scale-up to the large 12 dm^2 electrodes. Basically the present design is highly cost effective in terms of $/kWh. This is due to the extensive use of plastics in the battery structure, particularly plastic electrodes, and the intrinsic low cost of zinc and bromine. This costing reflects a higher degree of system definition than previous studies so that the cost estimates much more realistic than in earlier studies. The present costs are sufficiently low so that redesigns aimed at further cost reductions have a very low priority.

APPENDIX 3

ANALYSIS OF SHUNT CURRENT ELIMINATION METHODS IN ELECTROCHEMICAL SYSTEMS HAVING COMMON ELECTROLYTE

Electrochemical cell systems can have many cells connected in series to make a high voltage device as shown in Figures A-3a and A-4a. In many systems reactants are supplied to the cells from a common manifold system. The cells are connected to these manifolds by channel/pipes. The products are removed from the cells by another set of channels and manifolds.

Circulating electrolytes are used in these systems for ease of addition of reactants and removal of products, uniformity of reaction at electrodes, uniform plating and thermal management.

These advantages outweigh the hydraulic complexity.

In these systems, however, there are shared or common electrolytes. The common electrolyte form a single physical continuum through each cell through the common manifold containing shared electrolyte through individual cell channels. The common electrolyte provides alternate current pathways for the system current to shunt around cells during charge or to self-discharge by shuntage during open circuit or discharge.

Currents supplied to or removed from the electrochemical device will, in part, shunt or bypass the cells through the common electrolyte.

This shuntage causes:

- non-uniform distribution of cell capacities
- non-uniform current densities
- maldistribution of products
- contamination of products
- corrosion of electrodes
- irregular plating
- safety hazards
- power loss

These problems have hindered the development of high energy density, low cost batteries and electrochemical reactors.

The effects of the shuntage currents can be eliminated by the passage of an appropriate current through the common electrolyte manifold, Figure A-3b or through interconnections between the channels Figure A-4b. These interconnections are referred to as tunnels. The resistances of the tunnels may be uniform or they may, as seen later, be progressively increased towards the middle of the system of the series of cells and then progressively and symmetrically decreased. This approach is called tapering or tapered tunnels.

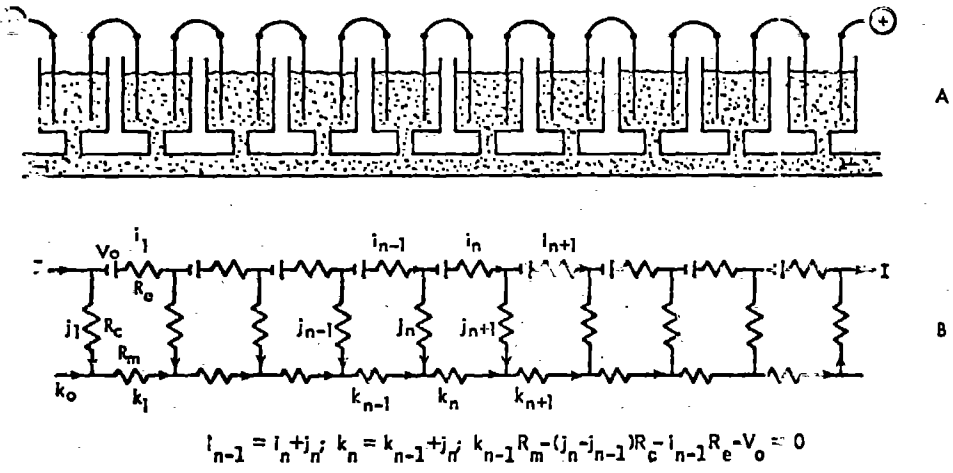

Figure A-3a Series-Connected Cells with Common Electrolyte Manifold

Figure A-3b Lumped Resistive Equivalent Circuit with Governing Difference Equations

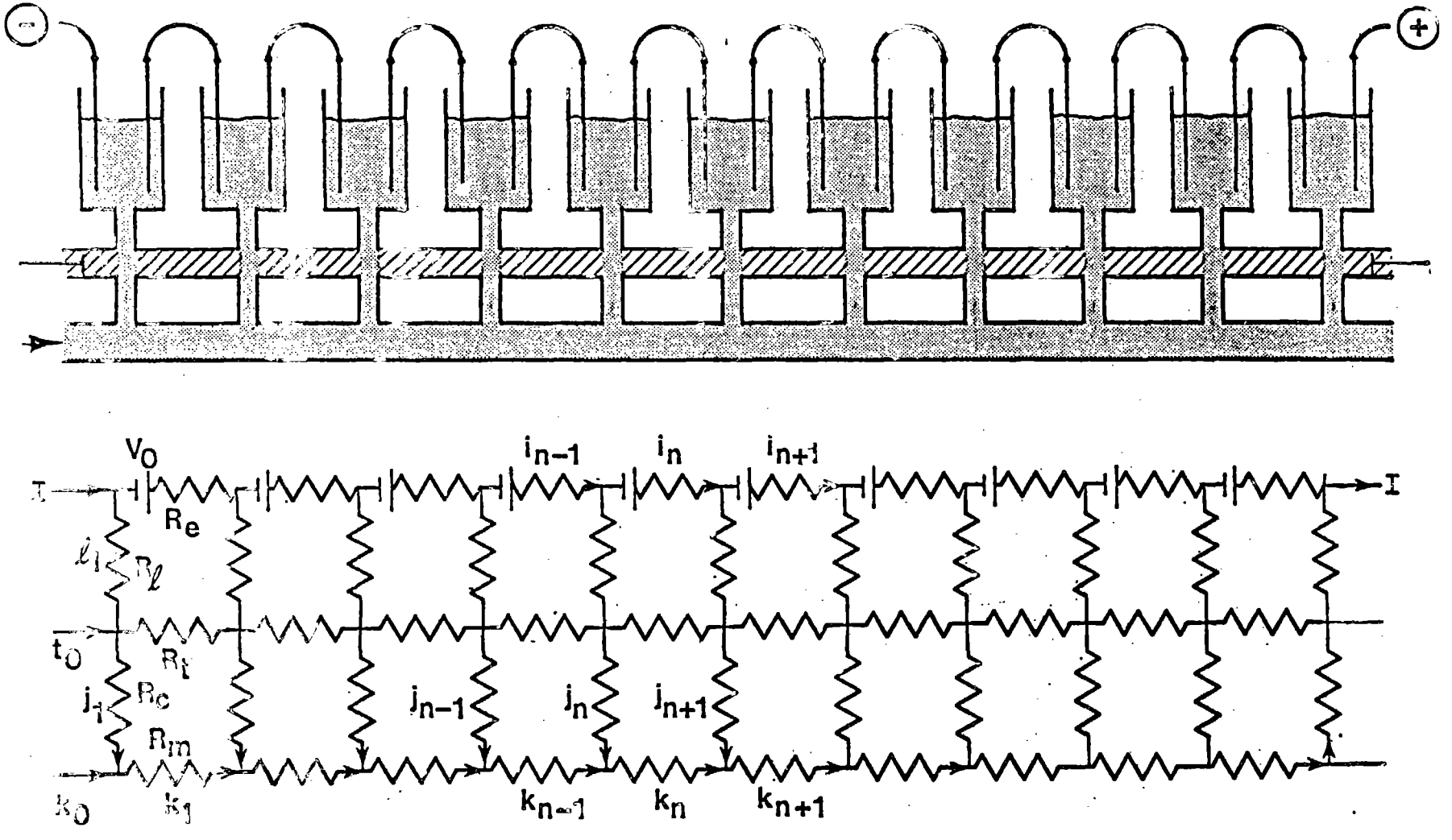

Figure A-4a Series-Connected with common Electrolyte Manifold and Channel Interconnections.
Figure A-4b Lumped Resistive Equivalent Circuit.

The tunnel approach, while more complex, requires less power than the manifold approach.

Manifold Protection

The analysis of the shuntage in common electrolyte systems and the derivation of the shunt current elimination equations followed from a resistance equivalent circuit model of an electrochemical device with common electrolyte, Figure A-5a.

The shunt current model was developed with the assumption that all of the cells in the device are identical. Based on this assumption, the governing circuit equations were written as linear, constant coefficient difference equations for which general closed form solutions were obtained for currents in the electrolyte within the cells (intercells), within the channels and within the manifold (shared electrolyte). Because the channel resistance was found generally to be much larger than the manifold and intracell electrolyte resistances, approximate algebraic solutions were also developed. It was demonstrated that a single externally imposed current passed from the last cell to the first cell through the manifold can result in minimization of shunt currents and, optimally, may effectively set all channel currents to zero.

Each cell was modeled as an ideal voltage source V_o equal to its open circuit potential, in series, with an intracell electrolyte resistance R_e. Then, as shown in Figure A-5a the current through the electrodes divided so that some current passed through each channel into the manifold (shared electrolyte). The variables used in Figure A8a are as follows:

R_m = manifold resistance;
R_c = channel resistance;
R_e = intracell electrolyte resistance (including internal components such as separators and membranes);
V_o = open circuit cell voltage;
V = actual cell voltage including ohmic voltage drop;
i_n = the principal electrolyte current through the nth cell;
j_n = the channel shunt current through the nthchannel;
k_n = the manifold shunt current through the manifold between the nth and the nth + 1 channels;
k_o = the current through the manifold needed to reduce shunt currents to zero; and
I = the total terminal current through the electrochemical device.

As shown in Figure A-5a the electrochemical device is illustrated schematically and contains cells 4, 6, 8, 10, 12, and 14, electrically connected in series. Current I passes through the cells from end plate 16 to end plate 18. Common electrolyte (not shown) forms a single physical continuum through each cell via common manifold 20, containing shared electrolyte carried in parallel to each individual.

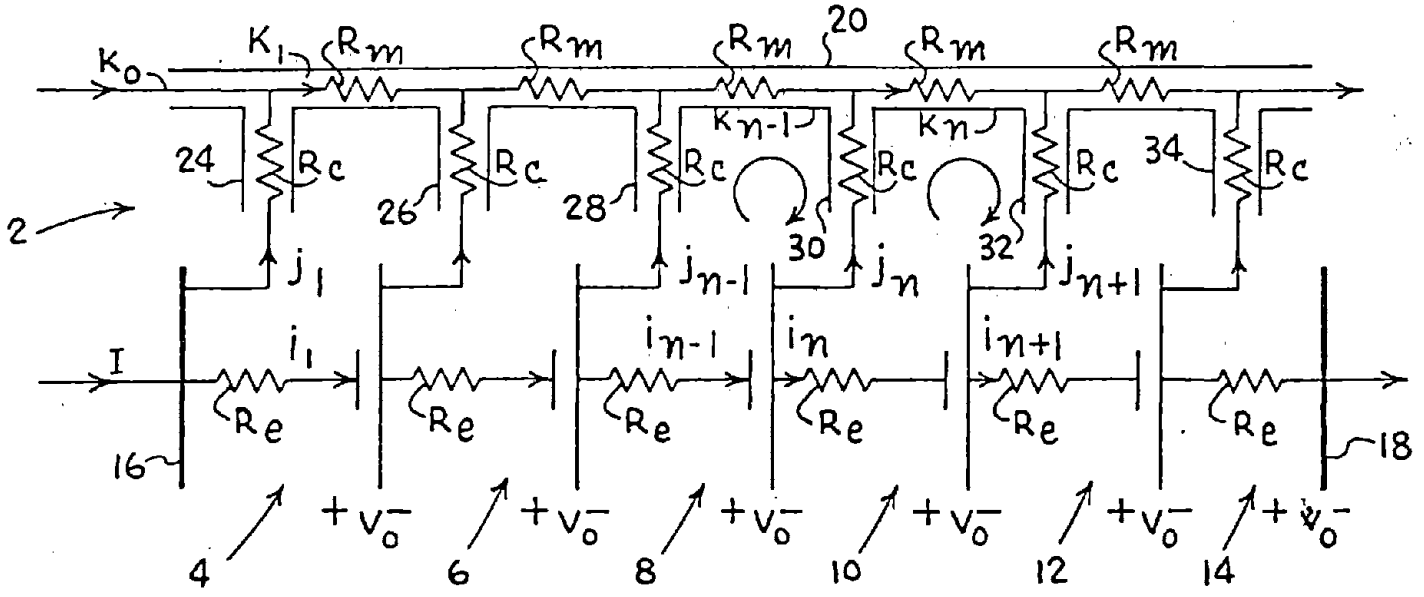

Figure A-5a Shunt Current Model

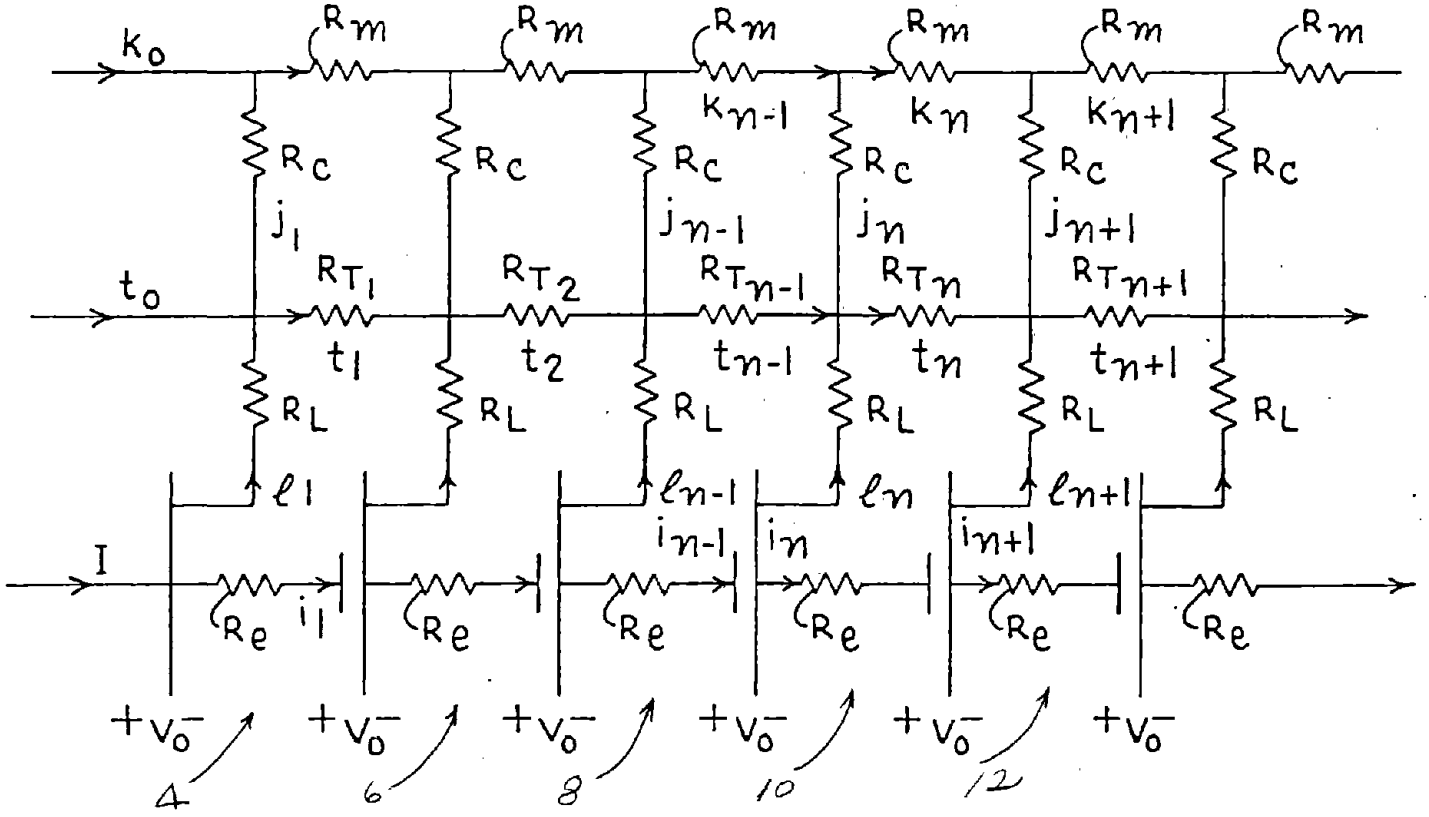

Figure A-5b Tapered Tunnel Shunt Network

cell by channels 24, 26, 28, 30, 32, and 34. The resistance of the electrolyte in each cell is shown as R_e. The resistance of the manifold is shown as R_c. The currents i_n, j_n and k_n, as defined above, are also illustrated.

Each electrolyte section was modeled with its appropriate resistance. Kirchoff's current and voltage laws applied at the nth cell requires:

$$i_{n-1} - i_n = j_n \tag{1}$$

$$k_{n-1} - k_n = -j_n \tag{2}$$

$$k_{n-1} R_m - R_c(j_n - j_{n-1}) - i_{n-1} R_e = V_o \tag{3}$$

Similarly, Kirchoff's current and voltage laws applied at the n + 1 cell requires:

$$k_n R_m - R_c (j_{n+1} - j_n) - i_n R_e = V_o \tag{4}$$

Then by substracting (4) from (3) the terms involving the i's and k's just equal j_n from (1) and (2) so that a single equation for the channel shunt currents is obtained:

$$j_{n+1} - B j_n + j_{n-1} = 0 \tag{5}$$

wherein B is equal to $2+ (R_e + R_m)/R_c$.

Just as linear constant coefficient differential equations have exponential solutions, linear constant coefficient difference equations as in (5) had power law solutions of the form:

$$j_n = A\lambda^n \tag{6}$$

wherein A is the amplitude and wherein the characteristic parameter (analogous to natural frequencies in continuous systems described by differential equations) was found by substituting the assumed solution of (6) back into (5):

$$A\lambda^{n-1}[\lambda^2 - B\lambda + 1] = 0 \tag{7}$$

For non-trivial solutions ($A \neq 0$, $\lambda = 0$), the bracketed term in (7) must be zero:

$$\lambda = B/2 \pm \sqrt{(B/2)^2 - 1} \tag{8}$$

Note that the two solutions in (8) are reciprocals of each other:

$$B/2 + \sqrt{(B/2)^2 - 1} = \frac{1}{B/2 - \sqrt{(B/2)^2 - 1}} \tag{9}$$

Because (5) is linear, the most general solution was a linear combination of both allowed solutions:

$$j_n = A_1\lambda^n + A_2\lambda^{-n} \tag{10}$$

where λ is either root in (8).

The amplitudes A_1 and A_2 were evaluated by the boundary conditions. By symmetry, the current in the first cell $j_1 = J$ had an equal magnitude but opposite direction to the current in the last cell, $j_n = -J$. Thus:

$$j_1 = J = A_1\lambda + A_2\lambda^{-1} \tag{11}$$

$$j_N = -J = A_1\lambda^N + A_2\lambda^{-N}$$

with solutions:

$$A_1 = \frac{-J(1 + \lambda^{-N-1})}{\lambda^N - \lambda^{-N+2}} \qquad A_2 = \frac{J\lambda(\lambda + \lambda^N)}{\lambda^N - \lambda^{-N+2}}$$

Applying algebraic reduction, the channel currents were:

$$j_n = \frac{J}{\lambda^N - \lambda}\left[-\lambda^n - \lambda^{N-n+1}\right] \tag{12}$$

At this point, J was not yet known. However, j_n was used in solving equations (1) and (2). Focusing attention on (1) the homogeneous solution was first found by assuming j_n as zero. Assuming power law solutions, the natural solution was a constant:

$$i_{n-1} - i_n = 0;\ i_n = Ap^n \tag{13}$$

$$Ap^{n-1}(1-p) = 0;\ p = 1;\ i_n = A \tag{14}$$

The driven solution must have the same power law dependence as the j_n and so were of the same form as (10). The total solution was then:

$$i_n = I + \frac{J\lambda}{(\lambda^N - \lambda)(\lambda - 1)}\left[\lambda^n + \lambda^{N-n} - 1 - \lambda N\right] \tag{15}$$

where the constant A in (14) was adjusted so that $i_0 = I$, where I is ther terminal current. Under open circuit conditions, I = 0. When the battery is being charged, I is positive; while under load, I is negative.

Similarly, the manifold shunt currents were:

$$k_n = k_0 - \frac{J\lambda}{(\lambda^N - \lambda)(\lambda - 1)}\left[\lambda^n + \lambda^{N-n} - 1 - \lambda^N\right] \tag{16}$$

where the initial manifold current k_0 was yet unspecified.

The important parameter J, which is the first channel current, was not yet known. Substituting (13), (14), (15), and (16) in (3) for any value of n and evaluating at n = 2, yields (17) or (18)*:

$$J = \frac{V_o + IR_e - k_o R_m}{R_m + R_e + R_c \frac{(\lambda-1)(\lambda^{N-1}+\lambda)}{(\lambda^N - \lambda)}} \qquad (17)$$

$$J = \frac{(V_o + IR_e - k_o R_m)(\lambda^N - \lambda)(\lambda - 1)}{\lambda (R_e + R_m)(1 + \lambda^N)} \qquad (18)$$

The foregoing equation (17) or its alternative equivalent form (18), revealed that J could be modified if k_o had a value other than zero. If J, the shunt current in the first branch channel, was reduced, then the j_n's (equation (12)) were reduced. If k_o had a value such that:

$$k_o = \frac{V_o + IR_e}{R_m} \qquad (19)$$

then J was zero and likewise all the j_n's were zero.

In this condition, equations (12), (15) and (16) reduce to:

$$i_n = I,\ k_n = k_o;\ j_n = 0 \qquad (20)$$

Thus, the foregoing suggested that the passage of a single protective current through the shared electrolyte in the manifold, in a device similar to that in Figure A-3a, might minimize (reduce or eliminate) shunt or leakage currents.

The direction of this current is the same as the unprotected k_n currents, i.e. the shunt current through the shared electrolyte.

It can also be seen from the above equations and the model in Figure A6a that when a k_o equal to that defined in equation 19 is passed through the shared electrolyte, that the voltage at each junction of the branch channel and the shared space is equal to that cell voltage. Thus, when the voltage drop through the branch channel is zero, there is no current. The voltage through the branch channel is nulled.

However, the voltages in the branch channels are not nulled when k_o is different from equation (20). Nonetheless, the shunt currents in these channels were reduced by applying some protective current and this was found to be useful in practical electrochemical devices wherein an exact k_o from equation (20) was not feasible.

From the practical standpoint, the utility of the foregoing approach required a non-zero R_m. Furthermore, the utility was enhanced by geometric effects which increased the magnitude of R_m. Such effects could be increasing the length of the shared electrolyte space between

---

*The equality of equations (17) and (18) can be shown by setting the right hand portions of (17) and (18) equal, and then solving for $(R_e + R_m)/R_c$. Then one substitutes $(\lambda^2-1)/\lambda$ for $(R_e + R_m)/R_c$. This is derived from $\lambda^2 + B\lambda - 1 = 0$ (equation (7)) and $B = 2 + (R_e + R_m)/R_c$ equation (5).

cells and a reduction of the cross-sectional area of the shared electrolyte space. The ratio of the protective current to the current of the electrochemical device was thus reduced when the ratio of R_m/R_e was increased. Hydraulic factors, however, should be considered, in particular with circulating systems, and design compromises made between flow of electrolyte and the passage of current in the shared space may be appropriate.

The foregoing analysis assumes a model in which the values of R_m, R_c, R_e, and V_o are the same for all cells. However, in a practical device, these values will be determined by system geometry and manufacturing tolerances. It is obvious, however, even in such cases, that the passage of protective current through the shared electrolyte will modify and reduce currents in the branch channels, although in such cases absolute nulling may not be accomplished.

Thus, to summarize, shunt currents (and their effects) can be reduced or eliminated by a passage of a current through the manifold electrolyte (in the same direction as the shunt currents) and the passage of this current will be accompanied by a voltage drop down the manifold. The voltage difference between the cells through the channels to the manifold will be reduced, and, as the current is increased, the voltage difference approaches zero. (At sufficiently large currents through the manifold, the voltage difference through the channels becomes negative.)

The shunt currents from the cells through the shared electrolyte, as the voltage difference is nulled, become smaller and are eliminated. It follows that the power requirements for the reduction or elimination are determined by the resistance of the manifold and are independent of the resistance of the channels. The power requirements (P) for the protective current through the manifold directly above the N cells in a series of cells is approximated by:

$$P = \frac{(NV)^2}{NR_m} \quad \text{or simplifying } P = NV^2/R_m \qquad (21)$$

where N is number of cells, V is the cell voltage and R_m is the resistance of a single manifold segment.

Tunnel Protection

The power requirements for reduction of shunt currents can be markedly reduced by adding connecting tunnels between the individual cell channels. The protective current is applied at the junction of the tunnel with the first channel and at the junction of the tunnel with the last channel so as to pass through the connecting tunnels. The power and current requirements are lower, the closer the tunnels are to the junction of the channels to the cells. Optionally, additional protective current may also be inserted in the manifold via k_o, as desired. Thus, it is possible to operate with k_o equal to zero and to thereby achieve or approach total shunt current elimination.

The resistor network for this system is shown in Figure A-5b. The variables are as follows:

R_e = intracell electrolyte resistance;
R_c = channel resistance;
R_m = manifold resistance;
R_T = tunnel resistance;
R_L = leg resistance;
r_o = tunnel input current needed to minimize shunt currents;
t_n = tunnel current;
l_n = leg current;
j_n = channel shunt current
k_n = manifold shunt current;
i_n = cell current;
V_o = open circuit cell voltage;
I = total terminal current

The electrical circuit of Figure A8b will be used to develop an analysis for two electrochemical devices shown in Figures A-6 and A-7. Where applicable, like elements are provided with the same numerical and alpha-numerical designations in Figures A-6 and A-7. While the manifolds of Figures A-6 and A-7 are shown beisng fed at mid-portion thereof, it is to be understood that they could easily be fed at either or both ends.

Referring to Figure A-6, a dual electrolyte (anolyte and catholyte) multicell battery device is featured wherein protective currents are introduced to tapered tunnels 101a, 101b, 101c, and 101d, respectively, via electrodes 102a, 103a, 102b, 103b, 102c, 103c, and 102d, 103d, respectively.

The protective current in Figure A-6 is preferably introduced into tapered tunnels 101a, 101b, 101c, and 101d, respectively, at the junction of the tunnel 101a with the first and last channels 104a and 104aa, respectively; tunnel 101b with the first and last channels 104b and 104bb, respectively; tunnel 101c with the first and last channels 104c and 104cc, respectively; and tunnel 101d with the first and last channels 104d and 104dd, respectively, of the manifold and channel network illustrated in Figure A-6.

The electrochemical device generally comprises a plurality of cells (typical in which anolyte and catholyte are respectively circulated through respective cell compartments). The cells are electrically connected, at least in part, in series, and fluidically communicate in parallel via a plurality of typical channels 104 which are fed by respective manifolds 106a, 106b, 106c and 106d, respectively.

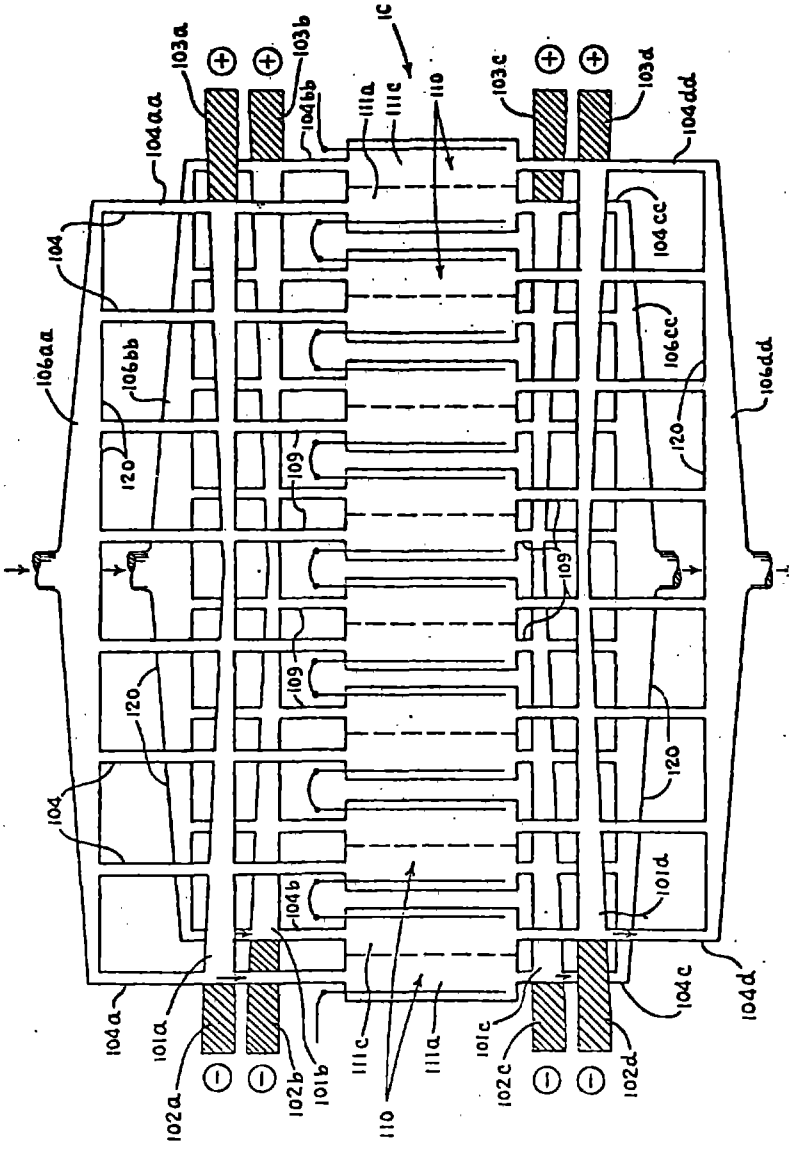

Figure A-6 Tapered Tunnel and Manifold Protection System

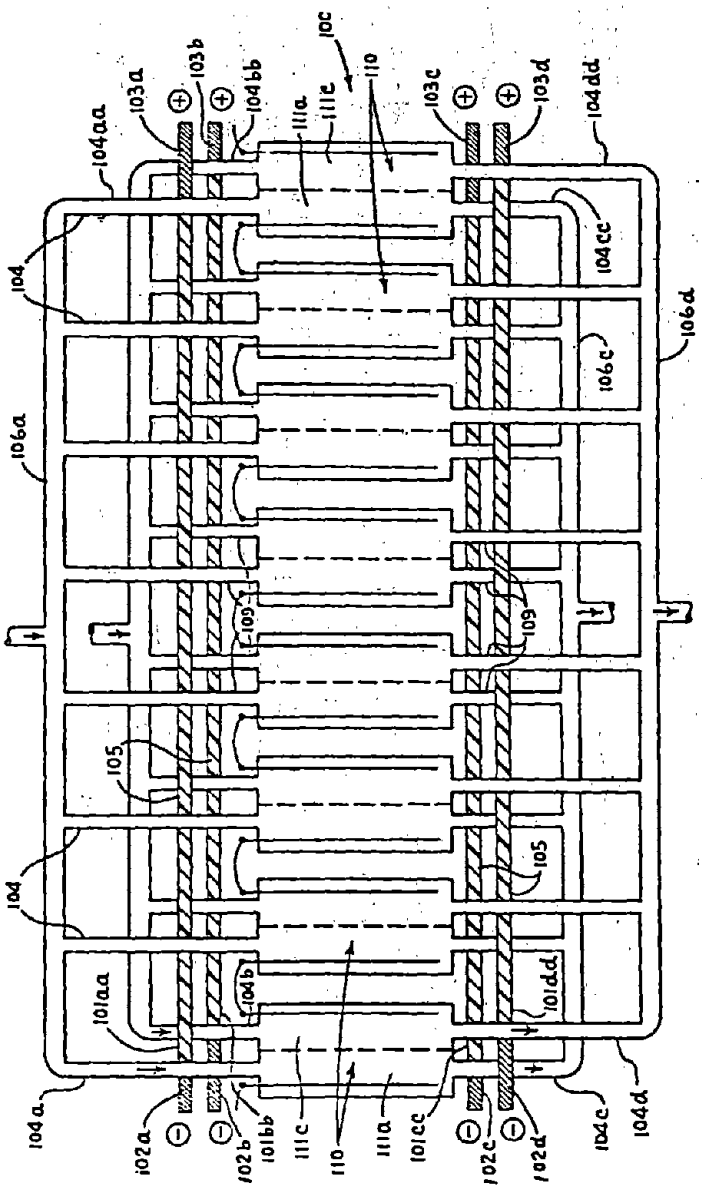

Figure A-7 Tapered Resistor Protective System

The protective current into the tunnels passes through the electrolyte(s) in the channels 104 above tunnels 101a and 101b, and below the tunnels 101c and 101d, in addition to the manifolds. In the case where the tunnels contain electrolyte(s) the protective current will also pass through the tunnels.

The tunnels 101aa, 101bb, 101cc, and 101dd of Figure A-7 are resistively tapered and do not contain electrolyte(s), as shown for Figure A-6. In the device of Figure A-7, the tunnels 101aa, 101bb, 101cc and 101dd are not part of the electrolyte system and may contain a plurality of solid resistive elements or segments 105, which elements are defined as one of the following: a salt bridge; an electronic conductor or resistor; an ion-exchange membrane; or a porous plug with ionic conductors, etc.

The only requirement for the tunnels is that the tunnels be an ionic or electronic conductor. The segments 105 are distributed along the tunnels 101aa, 101bb, 101cc and 101dd as between the channels 104, and have an increasing resistance as they approach a mid-portion of their respective tunnel.

Where the device contains electrolyte in the tunnels as respective devices in Figure A-6, the conduction is ionic throughout the tunnel-channel-manifold system. Where the device has solid resistive elements 105 in the tunnels 101aa, 101bb, 101cc and 101dd, as between channels 104 as illustrated in Figure A-7, a redox reaction is required at some or all of the tunnel-channel intersections in order to convert to and from ionic and electronic conduction. Such a scheme may be most desirable in a redox battery system. Also, with electronic conductor elements 105, it is relatively easy to add or subtract current at intermediate points in the tunnel system. Such intermediate additions or subtractions are more difficult in ionic conduction tunnels.

The increasing of the resistance along the tunnels to their mid-portions in the respective devices depicted in Figures A-6 and A-7 is for the purpose of reducing or eliminating shunt currents with a minimum of input power. Each of the devices can be respectively represented by the analogue resistor circuit shown in Figure A-5b and the analytical analyses for these representative devices will be with reference thereto.

In the case of the devices (tapered tunnels only) of Figures A-6 and A-7, respectively, each cell 110 is modeled as an ideal voltage source V_o equal to its OCV potential, in series with the current resistance product. The resistances of each tunnel segment as between the channels (e.g., elements 105 in Figure A-7) are chosen or defined as those which will provide a voltage drop equal to the voltage of the cell immediately beneath it. The small protective current passed into the tunnels via the electrodes may be supplied by an external source or from the terminus cells 110 of the electrochemical device shunt voltages for each cell 110. When the tunnel current "t_n" is passed, it by definition will cause the cell voltages to be equal to the voltage drop through resistor "R_{Tn}" (Figure A-5b) such that:

$$t_n R_{Tn} = V_o + IR_e$$

When this condition is met, the voltage on the channel legs 109 (Figures A-6and A-7) between the tunnels 101 and the cells 110 is nulled, and there are no currents in the legs 109.

The electrical resistor network analog is then equivalent to Figure A-5b.

Kirchoff's current and voltage laws applied at the tunnel loop above the nth cell requires that:

$$\text{Where } V_o + IR_e = t_nR_{Tn} = t_{n-1}R_{Tn-1} \tag{22}$$

$$k_{n-1} - k_n = -j_n \tag{23}$$

$$t_{n-1} - t_n = j_n \tag{24}$$

$$k_{n-1}R_m - j_nR_c + j_{n-1}R_c - t_{n-1}R_{Tn-1} = 0 \tag{25}$$

where:

k_n = manifold current in the nth manifold segment.

t_n = current in the tunnel.

j_n = current in the channel.

and R_e, R_m and R_{Tn} are the corresponding resistances of the cell, manifold, and a tunnel.

Increasing the index by one, the nth + 1 loop is:

$$k_nR_m - j_{n+1}R_c + j_nR_c - t_nR_{Tn} = 0. \tag{26}$$

Subtracting (26) from (25), the k terms equal j_n and the t terms cancel, from (24) and (23), leaving:

$$-j_nR_m - 2j_nR_c + j_{n+1}R_c + j_{n-1}R_c = 0 \tag{27}$$

Dividing (28) by R_c gives:

$$j_{n+1} - Cj_n + j_{n-1} = 0 \tag{28}$$

where

$$C = 2 + \frac{R_m}{R_c}$$

SOLUTION FOR CHANNEL CURRENTS

Linear constant coefficient difference equations (29) have power law solutions of the form:

$$j_n = D\lambda'^n \tag{30}$$

where λ' can be found by substituting the assumed solution of (30) into (29)

$$D\lambda'^{n-1}\left[\lambda'^2 - C\lambda' + 1\right] = 0 \tag{31}$$

For non-trivial solutions, ($D = 0$, $\lambda' = 0$), the bracketed term is thus zero, or:

$$\lambda' = C/2 \pm \sqrt{\left(\frac{C}{2}\right)^2 - 1} \tag{32}$$

For the manifold protection case, the most general solution of (29) is a linear combination of both solutions of (32).

$$j_n = D_1\lambda'^n + D_2\lambda'^{-n} \tag{33}$$

The current in the first channel $j_1 = J'$ is an equal magnitude, but opposite direction to the current in the last channel $j_N = -J'$, or:

$$\begin{aligned} j_1 &= J' = D_1\lambda' + D_2\lambda'^{-1} \\ j_N &= -J' = D_1\lambda'^N + D_2\lambda'^{-N} \end{aligned} \tag{34}$$

with solutions:

$$\begin{aligned} D_1 &= \frac{-J'\,(1 + \lambda'^{-N+1})}{\lambda'^N - \lambda'^{-N+2}} \\ D_2 &= \frac{J'\lambda'(\lambda' + \lambda'^N)}{\lambda'^N - \lambda'^{-N+2}} \end{aligned} \tag{35}$$

From (34) and (35):

$$j_n = \frac{J'}{\lambda'^N - \lambda'}\left[\lambda'^{N-n+1} - \lambda'^n\right] \tag{36}$$

From (24), assuming (36):

$$k_n = k_0 + \sum_{p=1}^{n} j_p = k_0 - \frac{J'\lambda'\left[\lambda'^n + \lambda'^{N-n} - 1 - \lambda'^N\right]}{(\lambda'^N - \lambda')\,(\lambda' - 1)} \tag{37}$$

Substituting (23), (36), (37) into (26):

$$J' = \frac{Vo + IRe - k_o R_m}{R_m + R_c \frac{(\lambda' - 1)(\lambda'^{N-1} + \lambda')}{(\lambda'^N - \lambda')}} \tag{38}$$

Tunnel Currents

The current in the first tunnel t_1 is given by (25):

$$t_1 = t_o - j_1 \tag{39}$$

Subsequent tunnel currents:

$$t_2 = t_1 - j_2 = t_o - (j_1 + j_2) \tag{40}$$

$$t_3 = t_2 - j_3 = t_o - (j_1 + j_2 + j_3) \tag{41}$$

build on (17). The general equation for tunnel currents is:

$$t_n = t_o - \sum_{i=1}^{n} j_i \tag{42}$$

But, from equation 37, eq. 42 also equals eq. 43 or eq. 44. Thus,

$$t_n = t_o + k_o - k_n \tag{43}$$

$$t_n = t_o - J' \frac{\lambda'}{\lambda' - 1} \left[\frac{\lambda'^{N+1} - \lambda'^{N-n} - \lambda'^{n}}{\lambda'^N - \lambda'}\right] \tag{44}$$

the current in the tunnel at the center of the stack, n = N/2 is given by (45):

$$t_{N/2} = t_o + k_o + J' \frac{\lambda'}{\lambda' - 1} \left[\frac{-(\lambda'^{N/2} - 1)^2}{\lambda'^N - \lambda'}\right] - k_o \tag{45}$$

and by rearranging eq. 45, we form (46):

$$t_o + k_o = t_{N/2} + k_{N/2} \tag{46}$$

Where, without loss of generality, the number of cells, N, can be taken as an even number.

But when:

$$k_o = \frac{V_o + IR_e}{R_m} \tag{47}$$

Eq. (45) reduces to (48), using eq. (38) and (39)

$$t_{N/2} = t_o \tag{48}$$

and eq. (46) then becomes eq. (49):

$$k_{N/2} = k_o \tag{49}$$

When:

$t_{N/2} = 0$, $t_o = 0$ and vice versa.

This value of k_o in eq. (47) is that which is used in the non-tunnel manifold protection system. It is relatively high current compared to t_o, developed later (eq. (50) or (51)).

When $k_o = 0$ the t_o current is given by (50) from eq. (46):

$$t_o = t_{N/2} + k_{N/2} \tag{50}$$

When the resistance of the center tunnel is very large, or infinite, the value of $t_{N/2}$ is very small, or zero. Then (28) becomes, from eq. (37):

$$t_o = k_{N/2} = J' \frac{\lambda'}{\lambda' - 1} \left[\frac{(\lambda'^{N/2-1})^2}{\lambda'^N - \lambda'} \right] \tag{51}$$

This current is the minimum value to null the shuntage.

When the resistance of the center tunnel has a finite value, equation (50) applies and t_o is larger by the amount of $t_{N/2}$.

In this case, the resistances of all of the tunnels are less, and the gradient of the resistances is not as steep.

The following expressions for the non-tunnel case were derived above:

$$k_{N/2} = k_o + J\frac{\lambda}{\lambda-1} \left[\frac{(\lambda^{N/2}-1)^2}{\lambda^N - \lambda} \right] \tag{52}$$

and

$$J = \frac{V_o + IR_e - k_o R_m}{R_m + R_e + (R_c + R_L)\frac{(\lambda-1)(\lambda^{N-1}+\lambda)}{(\lambda^N - \lambda)}} \tag{53}$$

and

$$\lambda = \beta/2 \pm \sqrt{(\beta/2)^2 - 1} \tag{54}$$

where

$$\beta = 2 + \frac{R_m + R_e}{R_c + R_L} \tag{55}$$

where $R_c + R_L$ equals the "R_c", the classical case previously cited.

When R_e is much smaller than R_m, and R_L is small compared to R_C then C defined after eq. (28) approximately = β defined in (55) so that λ' of (32) = λ (54), and the $k_{N/2}$ for the tapered tunnel case (51) approaches that of the classical shunt current case ($k_o = 0$) eq. (52).

The power for the protection is a function of $k_{N/2}$. Thus, the power for protection with tapered tunnels is minimal when $t_{N/2} = 0$ and when R_C is large. The power for protection approaches that dissipated in classical shunt as the value of R_L is small. (If $t_{N/2}$ has a value, the power for protection is correspondingly increased.)

The value for a tunnel resistance, R_T, for any channel coupling, n, is given by:

$$R_{T_n} = \frac{V_o + IR_e}{t_n} = \frac{V_o + IR_e}{t_o - \sum_{n=1}^{N} j_n} \qquad (56)$$

When $k_o = 0$ and $t_{N/2} = 0$; $t_o = k_{N/2} = \frac{J'\lambda'}{\lambda'-1} \left[\frac{(\lambda'^{N/2}-1)^2}{\lambda'^N - \lambda'} \right]$

then (56) equals, from (44) and (37):

$$R_{T_n} = \frac{V_o + IR_e}{J'\frac{\lambda'}{\lambda'-1} \left[\frac{\lambda'^{N-n} + \lambda'^{n} - 2\lambda'^{N/2}}{\lambda'^N - \lambda'} \right]} \qquad (57)$$

and from (38):

$$R_{T_n} = \frac{1}{\left[\frac{1}{R_m + R_C \frac{(\lambda'-1)(\lambda'^{N-1}+\lambda')}{\lambda'^N - \lambda'}} \right] \left[\frac{\lambda'}{(\lambda'-1)} \right] \left[\frac{(\lambda'^{N-n} + \lambda'^{n} - 2\lambda'^{N/2})}{(\lambda'^N - \lambda')} \right]} \qquad (58)$$

When $t_{N/2}$ and $R_{T_{N/2}}$ have values and $k_o = 0$, eq. (50) applies:

$$t_o = t_{N/2} + k_{N/2}$$

Then, from eqs. (43) and (46):

$$t_n = t_{N/2} + k_{N/2} - k_n \qquad (59)$$

Using eq. (22) eq. (59) becomes:

$$t_n = \frac{V_o + IR_e}{R_{T_{N/2}}} + k_{N/2} - k_n \qquad (60)$$

When this is substituted into eq. (56), and the reduction is followed, eq. (61) is formed:

$$R_{T_n} = \frac{1}{\left[R_m + R_c \frac{(\lambda'-1)(\lambda'^{N-1}+\lambda')}{\lambda'^N - \lambda'}\right]\left[\frac{\lambda'}{(\lambda'-1)}\right]\left[\frac{(\lambda'^{N-n}+\lambda'^{n}-2\lambda'^{N/2})}{(\lambda'^N-\lambda')}\right]} + \frac{1}{R_{T_{N/2}}}$$

The value of R_{T_n} is determined by the geometry of the system with the corresponding resistances and not by the voltage or currents of the cells in the stack. In this case, the shunt currents from a series-connected system with shared electrolyte can be controlled, reduced, or eliminated by the insertion of appropriate t_o current into the tapered tunnel network of an appropriate designed geometry. The voltage requirement is $(V_o + IR_e)$ $(N-1)$. The current requirement is given by eq. (50) or eq. (51). The power requirements are the product of voltage and current values.

The power requirements are less than those for the manifold protection case (i.e., $k_o = (V_o+IR_e)/R_m$) and, in the limit, approach the power which would have been dissipated in shuntage in the unprotected case.

- Turn-Around Current Efficiency of Shunt Current Protected Battery Systems

The turn around current efficiency, CE, of shunt current protected battery systems can be calculated by the following formulas:

$$CE = \frac{T_d\, h_d}{T_d\, h_d - HZ} \quad \text{or} \quad CE = \frac{T_d\,(T_c-Z)h_c}{T_d(T_c-Z)h_c - HZ(T_d-Z)} \qquad (1)$$

and where

$$h_d = \frac{(T_c-Z)\, h_c}{(-T_d+Z)}$$

$$H = h_c + h_d + h_o$$

Where H is the total time the battery system is at a potential, h_c, h_d, and h_o are hours of charge, discharge and open circuit time, T_d is the terminal discharge current, T_c is the terminal charge current, and Z is the protective current inserted into the manifold or into the tunnel node at an open circuit voltage condition value. The coulombic efficiency is assumed to be 100%.

When the battery is immediately discharged upon charge or when there is no potential on the battery at stand condition, the current efficiency equation reduces to:

$$CE = \frac{T_d(T_c-Z)}{T_c(T_d-Z)} \qquad (2)$$

The values of Z current depend upon the type of protection system. The protection systems and their values of Z are listed below. Q is the number of manifold or tunnel current inserts.

Protection system	Z	term
manifold protected	$Q\ V_o/Rm$	k_o
tapered tunnel protected	$Q\ a'g'_{x/2}\ V_o$	t_o

Tapered tunnel expressions above are defined in Table A3.

During the charge portion of the battery cycle, protective currents are supplied from the charging circuit current. Correspondingly during discharge, protective currents are supplied from the current produced by the battery.

Under open circuit condition the currents for protection can be supplied from the external power source or from the battery.

The turn-around current efficiencies were calculated from the above analysis, and tabulated below in Table A4. The pumping energies were not calculated and are a function of manifold and cell design. The main pressure drops are in the manifold and in the right angle turns into the channels. The values assumed for the calculations were:

Cell open circuit voltage V_o, 1.8 Volts
Number of cells, 52
Center/Center cell distance, 0.093 inch
Electrolyte resistance, 15 ohm cm
Manifold diameter, 1/8 and 1/4 inch (.05 and .95 cm)
Manifold segment resistance, 4.973 and 18.55 ohms
Channel resistance, 500, 1500, and 6,000 ohms
Stack currents, 10 to 30 mA/cm^2
Cell area, 600 cm^2 and 1,000 cm^2
Number of manifolds, 4
Cell quadrant area, 150 cm^2 and 250 cm^2
No open circuit stand time (eq 2)

Table A3

Total Protective Current Formulas

Protection System	Z
Manifold Protected	$Q\ (Vo/Rm)$
Tapered Tunnel Protected	$\dfrac{Q \quad V_o}{R_m + R_c \dfrac{(\lambda' - 1)(\lambda'^{N-1} + \lambda')}{(\lambda'^N - \lambda')}} \quad \dfrac{\lambda'}{\lambda'-1} \cdot \left[-\dfrac{(\lambda'^{N/2} - 1)^2}{(\lambda'^N - \lambda')} \right]$

where

$$\lambda' = C/2 \pm \sqrt{\left(\frac{C}{2}\right)^2 - 1} \qquad C = 2 + \frac{R_m}{R_c}$$

TABLE A4

TURN-AROUND CURRENT EFFICIENCY

Apparent System Current Density Charge/Discharge	Manifold Diameter 0.95 cm				Manifold Diameter 0.50 cm	
	Manifold Protected	Tunnel Protected			Manifold Protected	Tunnel Protected
		R_c				R_c
		500 Ohm·cm	1500 Ohm·cm	6000 Ohm·cm		1500 Ohm·cm
30/30 mA/cm^2	85.5%	87.5%	91.4%	96.5%	95.8%	96.3 %
20/30	81.8	84.3	89.3	95.6	94.7	95.3
10/30	71.0	77.7	82.8	93.0	91.5	92.5
10/10	62.0	66.6	76.3	89.9	87.9	89.2
30/10	74.6	75.0	84.2	93.3	91.9	98.7
Protective currents, Amps Manifold/Tunnel	0.352	0.299	0.202	0.080	0.097	0.086

From Table A3 and Table A4, it can be seen that turn around current efficiencies increases with:

- higher current densities
- short charge/discharge times
- short or no open circuit time
- large values of R_c, long narrow channels
- larger electrode area
- small manifold diameter

These factors must be balanced however with other design and system factors when considering a viable battery system.

APPENDIX 4

ZINC-BROMINE BATTERY TESTING

at

SANDIA NATIONAL LABORATORIES

Sandia National Laboratories
Albuquerque, New Mexico 87185

May 15, 1981

Dr. Richard Bellows
Exxon Enterprises Incorporated
P. O. Box 45
Linden, NJ 07036

Dear Dr. Bellows:

I am writing to provide you with performance data for the 500-Wh 8-cell zinc-bromine battery we are testing. The battery has completed over 100 daily cycles and is operating very well. It is being tested with a four-factor two-level test regime (see Figure 1). So far, all testing has been at 20°C.

Figure 2 shows the range of energy efficiency values obtained to date. Numbers correspond to different cycle types as listed in Table 1. We intended to run each cycle type in a continuous set, but unanticipated problems caused some discontinuity in the data. On three occasions, impending pump failure led us to discharge the battery at the high rate. There were two cycles where strip chart recorder failure resulted in lost data. The majority of cycles were run as planned.

Table 1 lists a detailed data summary for the first 100 cycles. Energy efficiency varies from 69 to 60 percent. The high discharge rate cycles result in lower efficiency values. Lower maximum state of charge also causes a decrease in efficiency for cycles other than the baseline type.

Representative battery and cell voltage data is given in Table 2. Values at the various times have decreased by about 0.02 volts between cycle 16 and cycle 100. The values of cells six and seven have always been incorrect. We do not plan to repair the voltage probe until it becomes necessary to repair the stack.

We have been monitoring the pH of the electrolyte at intervals of two to four weeks. The results are shown in Table 3. The values seem rather inconsistent, but a gradual

upward trend is apparent. When the pH exceeds 3.5, the solutions will be adjusted with HBr, as per instructions.

The only problems encountered during the first hundred cycles involved the electrolyte pumps. About every month and a half we have had to grease the shaft bushing in the pump end of the motor. While we are experimenting with different greases, we have not located one that is long lasting. The battery also has a slight leak from the cell voltage tap area, but it is not significant.

We are planning to start the 50°C cycle tests in about two months. Also, the two-level test regime will be expanded to a three-level plan. Lower values will be selected, such as a 7.0A charge and discharge rate. We are currently performing decreased flow cycle tests using the baseline cycles. The data has not yet been reduced, but we are seeing a dip in the discharge voltage, near the end of discharge, as opposed to a straight line (refer to Figure 3). We are unsure if this is real or a data recorder problem. If you have any comments on any of the data or the test plan, please feel free to contact me.

We have received the 20-cell unit and will store it until our fume hood is installed. We will then operate the battery using computer control under the same general test schedule as the 8-cell stack. We will contact you when we are ready to install the battery, which will be around the middle of June.

Sincerely,

Paul C. Butler

Paul C. Butler
Division 2525

PCB:2525:jh

TABLE 1

DATA SUMMARY FOR CYCLES 1 TO 100
500 WH EXXON ZINC BROMINE BATTERY

ALL CYCLES AT 20°C

Cycle Type	Number of Cycles	Charge Rate (A) ±0.3	Discharge Rate (A) ±0.3	Maximum State of Charge (%) ±2	Average Coulombic Efficiency (%)	Average Voltaic Efficiency (%)	Average Energy Efficiency (%)	Comments
Baseline; #1	42	11.7	11.7	84	84±3	82±1	69±2	
#2	13	11.7	17.4	84	82±2	78±1	64±1	
#3	10	11.7	7.0	84	81±1	84±1	68±1	
#4	5	17.4	11.7	84	84±1	81±1	67±1	
#5	6	17.4	17.4	84	82±2	78±1	63±2	
#6	6	11.7	11.7	50	84±2	82±1	69±1	
#7	5	11.7	17.4	50	79±2	77±1	60±1	
#8	6	17.4	11.7	50	85±3	78±1	66±2	
#9	7	17.4	17.4	50	83±2	75±1	62±3	

TABLE 2

BATTERY AND CELL VOLTAGE VALUES
DURING REPRESENTATIVE CYCLES

500 WH EXXON ZINC BROMINE BATTERY

Cycle #		End of Charge	O.C. After Charge	Start of Discharge	End of Discharge
16	BV	15.62	14.52	13.40	8
	CV#1	1.96	1.82	1.67	-0.28
	CV#2	1.95	1.82	1.68	1.34
	CV#3	1.94	1.81	1.68	0.96
	CV#4	1.95	1.81	1.68	1.21
	CV#5	1.95	1.81	1.68	1.49
	CV#6	0.16	0.05	-0.04	-0.15
	CV#7	3.74	3.58	3.39	2.02
	CV#8	1.96	1.81	1.67	1.53
100		15.48	14.36	13.21	8
		1.94	1.80	1.65	0.14
		1.93	1.79	1.65	1.19
		1.93	1.80	1.65	0.60
		1.93	1.80	1.65	0.88
		1.93	1.79	1.65	1.45
		0.17	0.05	-0.04	-0.19
		3.70	3.54	3.34	1.96
		1.93	1.79	1.65	1.48

NOTE: Both cycles are the baseline type (#1).

TABLE 3

Ph DATA SUMMARY FOR CYCLES 1 TO 100
500 WH EXXON ZINC BROMINE BATTERY

Date	Cycles Completed	Ph of Anolyte	Ph of Catholyte	Comments
11/20/80	9	1.5	1.2	
12/8/80	17	1.1	0.9	
12/19/80	25	1.9	1.4	
1/26/81	34	1.5	1.1	
2/18/81	48	2.0	1.5	
2/27/81	57	2.5	2.4	
3/10/81	64	2.0	1.8	
4/15/81	93	2.3	2.5	
5/1/81	102	2.4	2.8	

Notes:
1. First battery cycle on 10/28/80.
2. Ph values measured on fully discharged battery.
3. Ph meter standardized with Ph 2 and 4 buffer.

FIGURE 1

EXXON ZINC BROMINE BATTERY TESTING

FOUR FACTOR TWO LEVEL TEST

FACTOR	LEVELS	
	HIGH	LOW
A*CHARGE RATE	17.4A	11.7A
B*DISCHARGE RATE	17.4A	11.7A
C*STATE OF CHARGE	84%	50%
D*TEMPERATURE	50 C	20 C

FIGURE 2

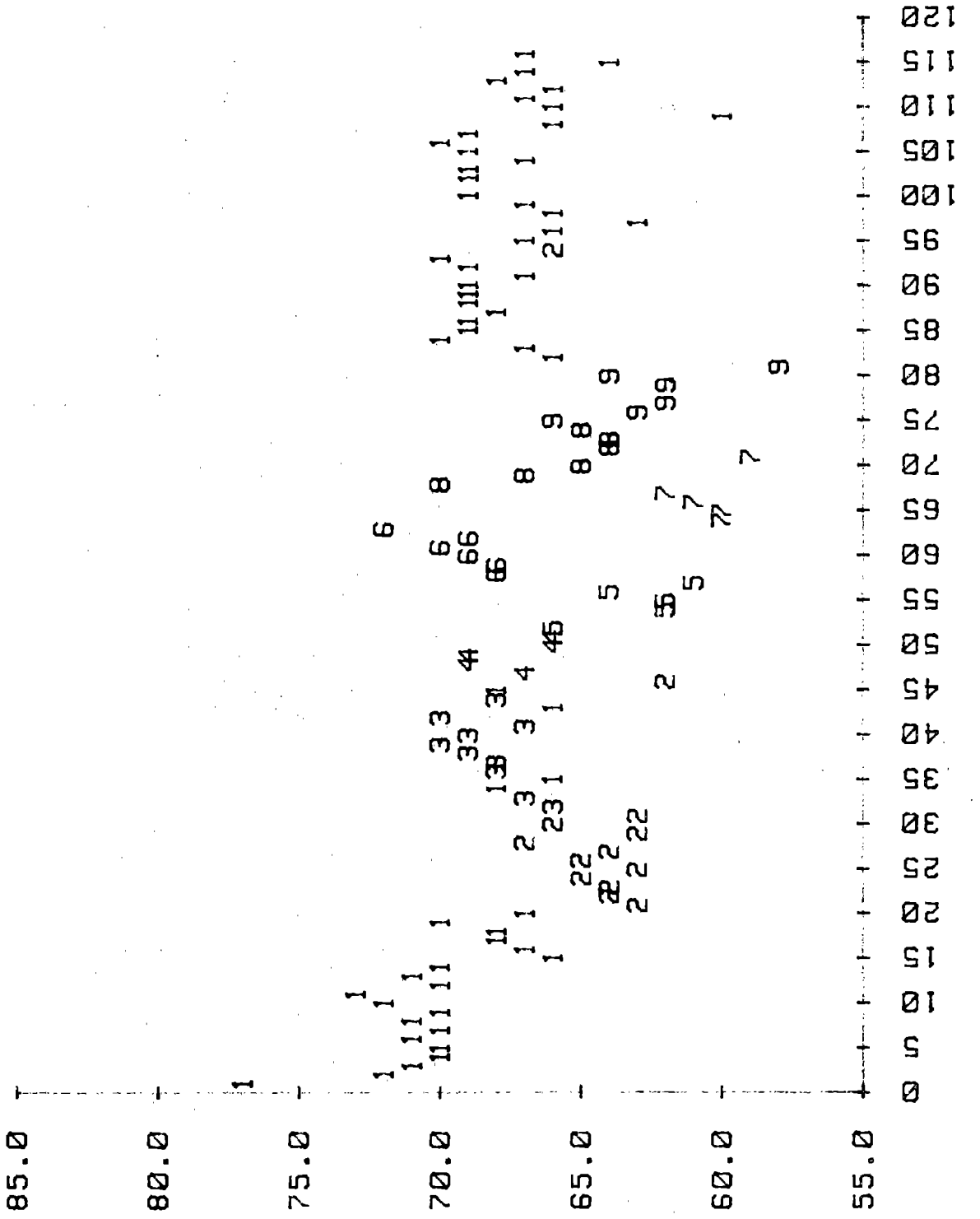
EXXON 500 Wh ZINC BROMINE BATTERY
ENERGY EFFICIENCY
85.0
80.0
75.0
70.0
65.0
60.0
55.0
0
5
10
15
20
25
30
35
40
45
50
55
60
65
70
75
80
85
90
95
100
105
110
115
120
CYCLE NUMBER

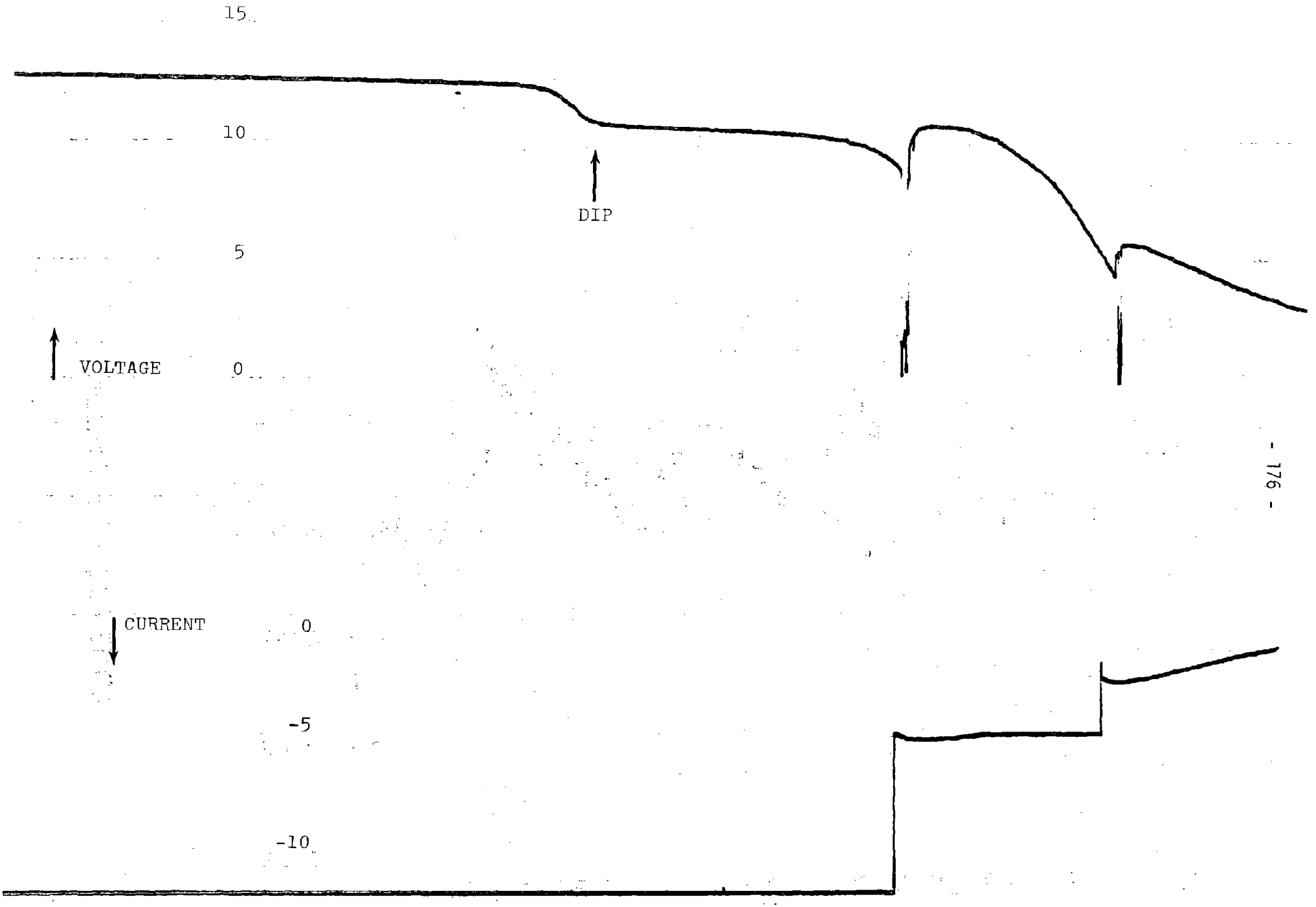

FIGURE 3